



Spatial correlations in parametric down-conversion

S.P. Walborn^a, C.H. Monken^b, S. Pádua^b, P.H. Souto Ribeiro^{a,*}

^a Instituto de Física, Universidade Federal do Rio de Janeiro, Caixa Postal 68528, Rio de Janeiro, RJ 21941-972, Brazil

^b Universidade Federal de Minas Gerais, Caixa Postal 702, Belo Horizonte, MG 30123-970, Brazil

ARTICLE INFO

Article history:

Accepted 1 June 2010

Available online 6 July 2010

editor: G.I. Stegeman

ABSTRACT

The transverse spatial effects observed in photon pairs produced by parametric down-conversion provide a robust and fertile testing ground for studies of quantum mechanics, non-classical states of light, correlated imaging and quantum information. Over the last 20 years there has been much progress in this area, ranging from technical advances and applications such as quantum imaging to investigations of fundamental aspects of quantum physics such as complementarity relations, Bell's inequality violation and entanglement. The field has grown immensely: a quick search shows that there are hundreds of papers published in this field, some with hundreds of citations. The objective of this article is to review the building blocks and major theoretical and experimental advances in the field, along with some possible technical applications and connections to other research areas.

© 2010 Elsevier B.V. All rights reserved.

Contents

1. Introduction.....	88
2. Fundamentals of parametric down-conversion.....	89
2.1. Classical and quantum parametric interaction.....	89
2.2. The coincidence count rate.....	92
3. Fundamentals of spatial correlations.....	93
3.1. Transverse coherence and partial coherence: classical optics.....	93
3.1.1. Double slit experiment: perfect coherence.....	93
3.1.2. Partial coherence and the van Cittert–Zernike theorem.....	93
3.1.3. The coherence area.....	95
3.2. The Fresnel and paraxial approximations.....	95
3.3. The angular spectrum and its propagation.....	96
3.4. Quantum state of photon pairs: spatial degrees of freedom.....	97
3.5. Coincidence detection probability and probability amplitude.....	99
3.6. The role of the spatial properties of the pump field.....	99
4. Double slit experiments with twin photons.....	100
4.1. Nonlocal dependence of spatial coherence.....	101
4.2. Ghost interference.....	102
4.2.1. The advanced wave picture.....	103
4.3. The de Broglie wavelength of a two-photon wave packet.....	103
4.3.1. Quantum lithography.....	104
4.4. Non-local double slit.....	105
4.5. The double-slit quantum eraser.....	106
5. Quantum imaging.....	107

* Corresponding author.

E-mail address: phsr@ifufrj.br (P.H. Souto Ribeiro).

5.1.	Quantum images.....	108
5.2.	Classical two-photon images.....	108
5.3.	Phase objects.....	110
5.4.	Spatial resolution of magnified images: quantum versus classical.....	110
6.	Spatial correlations: quantum versus classical.....	111
6.1.	Conditional interference and complementarity in one and two-particle interference patterns.....	112
6.2.	Spatial antibunching.....	113
7.	Spatial entanglement.....	115
7.1.	Continuous variable entanglement criteria.....	115
7.2.	Correlations in the near and far field.....	116
7.3.	Einstein–Podolsky–Rosen non-locality.....	117
7.4.	Propagation of spatial entanglement.....	118
7.5.	Fractional Fourier transform.....	119
7.6.	Correlations at intermediate planes.....	120
8.	Transverse modes.....	122
8.1.	Laguerre Gaussian modes: orbital angular momentum of light.....	122
8.2.	Entanglement and conservation of orbital angular momentum in SPDC.....	122
8.3.	Probing the phase structure of the two photon state: two-photon interference.....	124
8.4.	Quantifying spatial entanglement.....	125
8.4.1.	Schmidt decomposition of SPDC.....	125
8.5.	Hermite–Gaussian modes.....	127
8.6.	Down-conversion with Hermite–Gaussian modes.....	128
8.7.	Bell non-locality.....	128
9.	Applications to quantum information.....	130
9.1.	Generation of entangled qudits.....	130
9.2.	Quantum cryptography.....	131
9.3.	Quantum teleportation.....	133
10.	Conclusion.....	135
	Acknowledgements.....	135
	References.....	135

1. Introduction

Correlations between optical fields produced in spontaneous parametric down-conversion (SPDC) were first observed in 1970 by Burnham and Weinberg [1]. In this early experiment, they investigated the temporal and spatial correlation between pairs of photons. From the theoretical point of view, it was Zeldovich, Krindach and Klyshko who first studied the statistical properties of the light produced in this process, as early as 1969 [2,3]. The temporal correlations were studied and utilized in the pioneering series of work of Prof. Leonard Mandel and his group [4–8], giving rise to the use of the term *twin photons*, since the temporal correlation indicates that pairs of photons are born simultaneously. These correlations are of fundamental importance in all experiments with twin photons. They provide the time correlation which allows for the post-selection of photon pairs born from the same pump photon, which may present correlations in other degrees of freedom, such as the transverse position and momentum. Both the time and spatial correlations have been proven to be non-classical. The simple observation of a coincidence rate above the rate of accidental coincidence counts already leads to the violation of a classical inequality [9]. In the early Burnham and Weinberg experiment [1], spatial correlations were already observed. They demonstrated that the transverse profile of the coincidence distribution in the far field is narrower than the single photon intensity distribution. However, more comprehensive investigations were made only in the 1990s. For instance, Grayson and Barbosa [10] investigated spatial correlations for use in induced coherence without induced emission [11]. Joobeur et al. [12] studied general spatial and temporal coherence properties, and Souto Ribeiro et al. [13] started a long series of experiments using double-slit apertures and coincidence detection, initially dedicated to the study of spatial coherence properties of twin photons. Strekalov et al. [14] performed a novel double-slit experiment to observe *ghost* interference fringes and Pittman et al. [15] initiated a series of experiments on what was called *Quantum Imaging*, with the two-photon field from SPDC. Monken et al. [16] demonstrated that the spatial correlations could be controlled through the shaping of the angular spectrum of the pump beam. This control allowed the use of the spatial correlations in a series of applications, ranging from fundamental aspects of Quantum Mechanics such as the measurement of the photonic de Broglie wavelength of a two-photon wave packet [17] and the observation of the spatial anti-bunching of photons [18,19], to applications to quantum information such as, for instance, the production of spatial qudits [20]. Howell et al. [21] and D’Angelo et al. [22] formally demonstrated entanglement between the spatial properties of the twin photons.

In this review, we will discuss the spatial correlations between twin photons produced in parametric down-conversion, starting with the basic concepts and basic theory for the description of the down-conversion process and temporal simultaneity. We will introduce some basic concepts related to the classical spatial coherence of light fields and propagation of paraxial light beams. The theoretical framework for the description of quantum spatial correlations will be introduced and the remainder of the text will be dedicated to the description and discussion of several key experiments and applications:

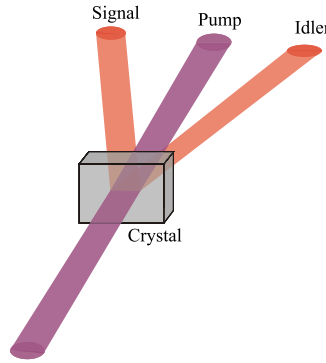


Fig. 1. Pumping a non-linear crystal with an intense laser beam produces low intensity signal and idler beams by the non-linear process of spontaneous parametric down-conversion.

double-slit experiments, quantum images, demonstration of non-classicality, spatial entanglement, transverse modes and applications to quantum information.

2. Fundamentals of parametric down-conversion

In SPDC, a nonlinear birefringent crystal is typically pumped by an intense pump laser beam, producing low intensity signal and idler fields, as illustrated in Fig. 1. The pump laser has frequency ω_p and is typically in the UV or violet region, while the down-converted signal and idler fields have frequencies ω_s and ω_i that are usually in the visible or near infra-red region of the spectrum. There have been many theoretical treatments of SPDC, beginning with the early work of Klyshko [23] and later by Hong and Mandel [5]. A detailed account of these calculations is out of the scope of this review, but can be found in the Ph.D. thesis of Wang [24] and the books by Klyshko [25], Mandel and Wolf [26] and Ou [27]. In this section, we follow the treatment presented in Refs. [5,24] to introduce the main features related to the temporal correlations between twin photons produced in SPDC. Even though our main concern is the spatial correlation, their time correlation is essential in all experiments.

2.1. Classical and quantum parametric interaction

The quantum theory of parametric down-conversion can be derived from the classical description of the nonlinear interaction, followed by the quantization of the electromagnetic field. Up to second order, the components of the electric polarization of a nonlinear and non centrosymmetric optical medium when an electric optical field \mathbf{E} propagates through it is [28,29]

$$P_i(\mathbf{r}, t) = \epsilon_0 \int_0^\infty dt' \chi_{ij}^{(1)}(t') E_j(\mathbf{r}, t - t') + \int_0^\infty dt' \int_0^\infty dt'' \chi_{ijk}^{(2)}(t', t'') E_j(\mathbf{r}, t - t') E_k(\mathbf{r}, t - t''), \quad (1)$$

where $E_j(\mathbf{r}, t)$ is the j component of the electric field vector and $\chi^{(1)}$ and $\chi^{(2)}$ are the first and second order susceptibility tensors, respectively. Summation over all combinations of the tensor components and electric field components is assumed. For light sources with low electric field strengths compared with the characteristic atomic electric field strength $E_{at} \approx 6 \times 10^{11}$ V/m [30], only the linear term in Eq. (1) is significant. Increasing the field intensity by using laser sources, for example, increases the nonlinear terms in the polarization. We will focus on the second order non-linear interaction.

In order to quantize the field, we begin with the electromagnetic field Hamiltonian in the dielectric medium of volume V [26]

$$\mathcal{H}(t) = \frac{1}{2} \int_V d\mathbf{r} [\mathbf{D}(\mathbf{r}, t) \cdot \mathbf{E}(\mathbf{r}, t) + \mathbf{B}(\mathbf{r}, t) \cdot \mathbf{H}(\mathbf{r}, t)], \quad (2)$$

where \mathbf{D} is the displacement vector, \mathbf{B} is the magnetic induction and \mathbf{H} is the magnetic field. If we use the definition $\mathbf{D}(\mathbf{r}, t) = \epsilon_0 \mathbf{E}(\mathbf{r}, t) + \mathbf{P}(\mathbf{r}, t)$ in Eq. (2), and use Eq. (1), we can rewrite the Hamiltonian as

$$\mathcal{H}(t) = \mathcal{H}_0(t) + \mathcal{H}_I(t), \quad (3)$$

where $\mathcal{H}_0(t)$ contains the interaction of the electric field and the first order linear component of the electric polarization. The “perturbation” $\mathcal{H}_I(t)$ is the nonlinear interaction Hamiltonian, given by

$$\begin{aligned} \mathcal{H}_I(t) &= \frac{1}{2} \int_V d\mathbf{r} \mathbf{E}(\mathbf{r}, t) \cdot \mathbf{P}_{nl}(\mathbf{r}, t) \\ &= \frac{1}{2} \int_V d\mathbf{r} \int_0^\infty dt' \int_0^\infty dt'' \chi_{ijk}^{(2)}(t', t'') E_i(\mathbf{r}, t) E_j(\mathbf{r}, t - t') E_k(\mathbf{r}, t - t''), \end{aligned} \quad (4)$$

where $\mathbf{P}_{\text{nl}}(\mathbf{r}, t)$ is the nonlinear component of the electric polarization, and summation on repeated indices is understood. In order to avoid unnecessary difficulties in the quantization of the field, it is considered that there are no electromagnetic boundaries between the medium and the air. In all situations discussed here, the effects related to refraction and birefringence can be included classically, after the field is quantized. A more rigorous approach is not yet available and is still subject of research.

From this point on we concern ourselves only with the nonlinear portion of the Hamiltonian. It is also convenient to suppose that just after the crystal there are two interference filters limiting the frequency spectrum of the down-converted fields, and that the pump beam has a narrow frequency spectrum. The two-photon quantum state will then include the functions describing the signal and idler interference filters. As a part of the quantization procedure, we expand the classical optical electric field in terms of plane waves:

$$\mathbf{E}(\mathbf{r}, t) = \mathbf{E}^+(\mathbf{r}, t) + \mathbf{E}^-(\mathbf{r}, t), \quad (5)$$

with

$$\mathbf{E}^+(\mathbf{r}, t) = \frac{1}{\sqrt{\mathcal{V}}} \sum_{\mathbf{k}, \sigma} \mathbf{e}_{\mathbf{k}, \sigma} \varepsilon_{\mathbf{k}, \sigma} \alpha_{\mathbf{k}, \sigma} G(\omega) \exp[i(\mathbf{k} \cdot \mathbf{r} - \omega t)] = [\mathbf{E}^-(\mathbf{r}, t)]^*, \quad (6)$$

where

$$\varepsilon_{\mathbf{k}, \sigma} = \sqrt{\hbar \omega(\mathbf{k}, \sigma) / 2 \epsilon_0 n^2(\mathbf{k}, \sigma)}, \quad (7)$$

ϵ_0 is the free space permittivity, $G(\omega)$ is the transmission function of the interference filter, \mathcal{V} is the quantization volume, \mathbf{k} is the wave vector, $\mathbf{e}_{\mathbf{k}, \sigma}$ is the two-dimensional polarization vector, ω is the frequency, and $\alpha_{\mathbf{k}, \sigma}$ is the mode amplitude. The index σ is summed over orthogonal components of a two-dimensional polarization vector and \mathbf{k} is summed over all possible wave vectors.

We adopt the usual method of quantization of the electric field, letting $\alpha_{\mathbf{k}, \sigma} \rightarrow \mathbf{a}_{\mathbf{k}, \sigma}$, where $\mathbf{a}_{\mathbf{k}, \sigma}$ is the photon annihilation operator. Then, the electric field amplitude becomes a field operator, given by

$$\begin{aligned} \mathbf{E}^+(\mathbf{r}, t) &\rightarrow \mathbf{E}^+(\mathbf{r}, t) = \frac{1}{\sqrt{\mathcal{V}}} \sum_{\mathbf{k}, \sigma} \bar{\mathbf{e}}_{\mathbf{k}, \sigma} \varepsilon_{\mathbf{k}, \sigma} \mathbf{a}_{\mathbf{k}, \sigma} G(\omega) \exp[i(\mathbf{k} \cdot \mathbf{r} - \omega t)] \\ &= [\mathbf{E}^-(\mathbf{r}, t)]^\dagger. \end{aligned} \quad (8)$$

Substituting expression (8) into the classical Hamiltonian (4) we have a quantum Hamiltonian operator

$$\begin{aligned} \mathbf{H}_I &= \frac{1}{2\mathcal{V}^{3/2}} \sum_{\mathbf{k}_\sigma, \sigma_s} \sum_{\mathbf{k}_i, \sigma_i} \sum_{\mathbf{k}_p, \sigma_p} \mathcal{G}_{\mathbf{k}_s, \sigma_s}^* \mathcal{G}_{\mathbf{k}_i, \sigma_i}^* \mathcal{G}_{\mathbf{k}_p, \sigma_p} \mathbf{a}_{\mathbf{k}_s, \sigma_s}^\dagger \mathbf{a}_{\mathbf{k}_i, \sigma_i}^\dagger \mathbf{a}_{\mathbf{k}_p, \sigma_p} \exp[i(\omega_s + \omega_i - \omega_p)t] \chi_{ijk}(\mathbf{e}_{\mathbf{k}_s, \sigma_s})_i^* (\mathbf{e}_{\mathbf{k}_i, \sigma_i})_j^* (\mathbf{e}_{\mathbf{k}_p, \sigma_p})_k \\ &\times \int_V \exp[-i(\mathbf{k}_s + \mathbf{k}_i - \mathbf{k}_p) \cdot \mathbf{r}] d\mathbf{r} + H.C., \end{aligned} \quad (9)$$

where we have distinguished the three fields as *pump* (p), *signal* (s) and *idler* (i),

$$\mathcal{G}_{\mathbf{k}_j, \sigma_j} = i \sqrt{\frac{\hbar \omega(\mathbf{k}_j, \sigma_j)}{2 \epsilon_0 n^2(\mathbf{k}_j, \sigma_j)}} G[\omega(\mathbf{k}_j, \sigma_j)]. \quad (10)$$

V is the interaction (crystal) volume, and $H.C.$ stands for Hermitian Conjugate. Here, $n(\mathbf{k}_j, \sigma_j)$ is the linear refractive index of the (anisotropic) crystal. We have also eliminated all terms which do not conserve energy and have defined

$$\chi_{ijk} \equiv \chi_{ijk}^{(2)}(\omega_p = \omega_s + \omega_i) + \chi_{ijk}^{(2)}(\omega_i = \omega_s + \omega_p) + \chi_{ijk}^{(2)}(\omega_s = \omega_i + \omega_p), \quad (11)$$

with

$$\chi_{ijk}^{(2)}(\omega = \omega' + \omega'') = \int_0^\infty dt' \int_0^\infty dt'' \chi_{ijk}^{(2)}(t', t'') \exp[-i(\omega' t' + \omega'' t'')]. \quad (12)$$

To find the quantum state at a given time t , we assume that the nonlinear interaction is turned on at time $t_0 = 0$ when the system is in the initial state $|\psi(0)\rangle$. The state at time t is given by the time evolution of some initial state at $t_0 = 0$:

$$|\psi(t)\rangle = \mathbf{U}(t) |\psi(0)\rangle \quad (13)$$

where

$$\mathbf{U}(t) = \exp\left(\frac{1}{i\hbar} \int_0^t d\tau \mathbf{H}_I(\tau)\right), \quad (14)$$

is the time evolution operator.

If the pump field is sufficiently weak, such that the interaction time is small compared to the average time between down-conversions, then we can expand Eq. (14) in power series and keep only the two-photon term:

$$\mathbf{U}(t) = 1 + \left(\frac{1}{i\hbar} \int_0^t d\tau \mathbf{H}_I(\tau) \right) + \dots \quad (15)$$

The integral can be expressed in terms of Eq. (9) as:

$$\begin{aligned} \int_0^t d\tau \mathbf{H}_I(\tau) &= \frac{1}{2\mathcal{V}^{3/2}} \sum_{\mathbf{k}_s, \sigma_s} \sum_{\mathbf{k}_i, \sigma_i} \sum_{\mathbf{k}_p, \sigma_p} g_{\mathbf{k}_s, \sigma_s}^* g_{\mathbf{k}_i, \sigma_i}^* g_{\mathbf{k}_p, \sigma_p} \mathbf{a}_{\mathbf{k}_s, \sigma_s}^\dagger \mathbf{a}_{\mathbf{k}_i, \sigma_i}^\dagger \mathbf{a}_{\mathbf{k}_p, \sigma_p} \\ &\times \exp[i(\omega_s + \omega_i - \omega_p)t/2] \chi_{ijk}(\mathbf{e}_{\mathbf{k}_s, \sigma_s})_i^* (\mathbf{e}_{\mathbf{k}_i, \sigma_i})_j^* (\mathbf{e}_{\mathbf{k}_p, \sigma_p})_k \\ &\times t \operatorname{sinc}[(\omega_s + \omega_i - \omega_p)t/2] \int_V d\mathbf{r} \exp[-i(\mathbf{k}_s + \mathbf{k}_i - \mathbf{k}_p) \cdot \mathbf{r}] + H.C. \end{aligned} \quad (16)$$

Integration in \mathbf{r} leads to a sinc function involving the wave vectors, which provides the conservation of momentum condition:

$$\begin{aligned} \int_0^t d\tau \mathbf{H}_I(\tau) &= \frac{Vt}{2\mathcal{V}^{3/2}} \sum_{\mathbf{k}_s, \sigma_s} \sum_{\mathbf{k}_i, \sigma_i} \sum_{\mathbf{k}_p, \sigma_p} g_{\mathbf{k}_s, \sigma_s}^* g_{\mathbf{k}_i, \sigma_i}^* g_{\mathbf{k}_p, \sigma_p} \mathbf{a}_{\mathbf{k}_s, \sigma_s}^\dagger \mathbf{a}_{\mathbf{k}_i, \sigma_i}^\dagger \mathbf{a}_{\mathbf{k}_p, \sigma_p} \\ &\times \chi_{ijk}(\mathbf{e}_{\mathbf{k}_s, \sigma_s})_i^* (\mathbf{e}_{\mathbf{k}_i, \sigma_i})_j^* (\mathbf{e}_{\mathbf{k}_p, \sigma_p})_k \operatorname{sinc}[(\omega_s + \omega_i - \omega_p)t/2] \\ &\times \exp[i(\omega_s + \omega_i - \omega_p)t/2] \prod_m \operatorname{sinc}[(\mathbf{k}_s + \mathbf{k}_i - \mathbf{k}_p)_m l_m/2] \\ &\times \exp[-i(\mathbf{k}_s + \mathbf{k}_i - \mathbf{k}_p)_z l_z/2] + H.C., \end{aligned} \quad (17)$$

where $V = l_x \times l_y \times l_z$ and l_m is the dimension of the nonlinear medium in direction m ($m = x, y, z$).

The quantum state at time t can be finally obtained using Eq. (13), considering the initial state as the vacuum state, and using the interaction Hamiltonian in the form of Eq. (17):

$$\begin{aligned} |\psi(t)\rangle &= |vac\rangle + \frac{Vt}{2i\hbar\mathcal{V}^{3/2}} \sum_{\mathbf{k}_s, \sigma_s} \sum_{\mathbf{k}_i, \sigma_i} \sum_{\mathbf{k}_p, \sigma_p} g_{\mathbf{k}_s, \sigma_s}^* g_{\mathbf{k}_i, \sigma_i}^* g_{\mathbf{k}_p, \sigma_p} v_p(\mathbf{k}_p, \sigma_p) \\ &\times \chi_{ijk}(\mathbf{e}_{\mathbf{k}_s, \sigma_s})_i^* (\mathbf{e}_{\mathbf{k}_i, \sigma_i})_j^* (\mathbf{e}_{\mathbf{k}_p, \sigma_p})_k \operatorname{sinc}[(\omega_s + \omega_i - \omega_p)t/2] \\ &\times \exp[i(\omega_s + \omega_i - \omega_p)t/2] \prod_m \operatorname{sinc}[(\mathbf{k}_s + \mathbf{k}_i - \mathbf{k}_p)_m l_m/2] \\ &\times \exp[-i(\mathbf{k}_s + \mathbf{k}_i - \mathbf{k}_p)_z l_z/2] |\mathbf{k}_s, \sigma_s\rangle |\mathbf{k}_i, \sigma_i\rangle, \end{aligned} \quad (18)$$

where $|\mathbf{k}_s, \sigma_s\rangle$ and $|\mathbf{k}_i, \sigma_i\rangle$ are single photon Fock states in modes (\mathbf{k}_s, σ_s) (signal) and (\mathbf{k}_i, σ_i) (idler) respectively, and $v_p(\mathbf{k}_p, \sigma_p)$ is a classical amplitude corresponding to the plane wave component (\mathbf{k}_p, σ_p) of the pump beam. Quantum effects in the pump field are neglected in this treatment, since the pump depletion is much smaller than its average intensity and its quantum state is effectively constant. The annihilation operator for the pump modes was replaced in Eq. (18) by a classical amplitude.

In order to simplify expression (18), it is convenient to make the following approximations:

- (a) The interaction time is long enough, so that the term $\operatorname{sinc}[(\omega_s + \omega_i - \omega_p)t/2]$ is significant only when $\omega_s + \omega_i = \omega_p$. This assumption can be justified by the use of a moderate power pump laser so that the time interval between two down-conversions is large compared to the detection resolving time.
- (b) The frequency spread of the detectable down-converted fields is small compared to the central frequencies, so that the dispersion of the refractive indices around the central frequencies $\bar{\omega}_j$ is small and a linear approximation can be used. This assumption is justified by the use of narrow-band interference filters in front of the detectors.
- (c) The terms $g_{\mathbf{k}_j, \sigma_j}$ and $\tilde{\chi}_{ijk}^{(2)}$ are slowly-varying functions of \mathbf{k}_j , so that they may be taken as constants in the intervals considered for \mathbf{k}_j .
- (d) The pump beam propagates along the z axis and the crystal is large enough in the x and y directions to contain the whole pump beam transverse profile. In this case, l_x and l_y can be extended to infinity and the last term in the third line of expression (18) is proportional to

$$\delta(\mathbf{q}_s + \mathbf{q}_i - \mathbf{q}_p) \operatorname{sinc}[(k_{sz} + k_{iz} - k_{pz})L/2],$$

where $\mathbf{q}_j = (k_{jx}, k_{jy})$ is the transverse (xy) component of \mathbf{k}_j and $L = l_z$ is the crystal thickness.

- (e) The quantization volume is large enough to justify the replacement of summations over \mathbf{k} by integrals.

(f) The pump beam contains only extraordinary polarization. It is implicit in this assumption that we are dealing with negative birefringent crystals.

Under the above assumptions, Eq. (18) is written as

$$|\psi\rangle = |vac\rangle + \sum_{\sigma_s, \sigma_i} \int d\omega_s \int d\omega_i \int d\mathbf{q}_s \int d\mathbf{q}_i \Phi_{\sigma_s \sigma_i}(\mathbf{q}_s, \mathbf{q}_i, \omega_s, \omega_i) |\mathbf{q}_s, \omega_s, \sigma_s\rangle |\mathbf{q}_i, \omega_i, \sigma_i\rangle, \quad (19)$$

where $|\mathbf{q}_j, \omega_j, \sigma_j\rangle$ represents a one-photon state in the mode defined by the transverse component \mathbf{q}_j of the wave vector, by the frequency ω_j and by the polarization σ_j . The amplitude Φ is now reduced to

$$\Phi_{\sigma_s \sigma_i} \approx C_{\sigma_s \sigma_i} G_s(\omega_s) G_i(\omega_i) v(\mathbf{q}_s + \mathbf{q}_i, \omega_s + \omega_i) \text{sinc}[(k_{sz} + k_{iz} - k_{pz})L/2], \quad (20)$$

where $C_{\sigma_s \sigma_i}$ is a coupling constant which depends on the nonlinear susceptibility tensor, and $G(\omega_j)$ is the spectral function defined by the narrow bandwidth filters placed in front of the detectors. If the anisotropy of the medium is neglected (which is not always convenient), the longitudinal wave vector mismatch $k_{sz} + k_{iz} - k_{pz}$ is written as $\sqrt{|\mathbf{k}_s|^2 - |\mathbf{q}_s|^2} + \sqrt{|\mathbf{k}_i|^2 - |\mathbf{q}_i|^2} - \sqrt{|\mathbf{k}_p|^2 - |\mathbf{q}_s + \mathbf{q}_i|^2}$.

2.2. The coincidence count rate

The state given by Eq. (18) can be simplified, considering approximations that are appropriate to given specific experimental situations. In this section, let us consider that signal and idler fields are detected through small apertures at fixed positions far enough from the source, so that only one spatial mode is selected by each detector. In this case, when narrow bandwidth filters are used, the quantum state takes a very simple form:

$$|\psi(t)\rangle = C_1 |vac\rangle + C_2 \int d\omega_s \int d\omega_i G_s(\omega_s) G_i(\omega_i) v_p(\omega_i + \omega_s) |\omega_s\rangle |\omega_i\rangle, \quad (21)$$

where C_1 and C_2 are normalization constants.

The electric field operator can also be simplified to

$$\mathbf{E}^+(t + \tau) = C \int d\omega \mathbf{a}(\omega) \exp[-i\omega(t + \tau)], \quad (22)$$

where C is a constant.

The state in Eq. (21) and field operator in Eq. (22) were obtained under several approximations. However, they adequately describe the main features of time correlations between twin photons. The time correlation is always assumed and used in all twin-photon experiments with coincidence detection, even when the spatial correlations are the focus of the investigation. Therefore, it is important and interesting to calculate the coincidence count rate in this simplified point of view.

The coincidence count rate is given by the fourth order (in the fields) correlation function:

$$\begin{aligned} R_c(t + \tau_i, t + \tau_s) &= \langle \mathbf{E}_s^-(t + \tau_s) \mathbf{E}_i^-(t + \tau_i) \mathbf{E}_i^+(t + \tau_i) \mathbf{E}_s^+(t + \tau_s) \rangle \\ &= |\mathbf{E}_i^+(t + \tau_i) \mathbf{E}_s^+(t + \tau_s) |\psi(t)\rangle|^2. \end{aligned} \quad (23)$$

Using Eqs. (21) and (22), we obtain:

$$\begin{aligned} R_c(t + \tau_i, t + \tau_s) &= \eta^2 \left| \int d\omega_1 \int d\omega_2 \mathbf{a}(\omega_1) \mathbf{a}(\omega_2) \exp\{-i[\omega_1(t + \tau_i) + \omega_2(t + \tau_s)]\} \right. \\ &\quad \times \left. \int d\omega_s \int d\omega_i G_i(\omega_i) G_s(\omega_s) v_p(\omega_i + \omega_s) |\omega_i\rangle |\omega_s\rangle \right|^2, \end{aligned} \quad (24)$$

where η is a constant that depends on the square root of the pump beam power, the efficiency of the detectors and of the parametric down conversion process. After the action of the operators on the quantum state and integration over ω_1 and ω_2 , we obtain:

$$R_c(t + \tau_i, t + \tau_s) = \eta^2 \left| \int d\omega_i \int d\omega_s G_i(\omega_i) G_s(\omega_s) v_p(\omega_i + \omega_s) \exp[-i(\omega_i + \omega_s)t] \exp[-i(\omega_i \tau_i + \omega_s \tau_s)] \right|^2. \quad (25)$$

In the limit where the pump spectrum can be approximated by a delta function $v_p(\omega) \rightarrow \delta(\omega_p - \omega)$, the time correlation is:

$$\begin{aligned} R_c(\tau_i, \tau_s) &= \eta^2 \left| \int d\omega G_i(\omega) G_s(\omega_p - \omega) \exp[i\omega(\tau_s - \tau_i)] \right|^2 \\ &= \eta^2 |F(\tau_s - \tau_i)|^2, \end{aligned} \quad (26)$$

where $F(t)$ is the convolution of the Fourier transforms of the filter functions $G_i(\omega)$ and $G_s(\omega_p - \omega)$. Usually, the width of $F(t)$ is on the order of femtoseconds. This means that detections are simultaneous within the window of a few femtoseconds.

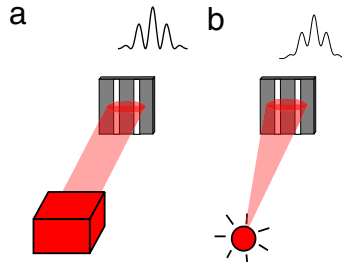


Fig. 2. Double-slit experiment. The double-slit is illuminated by a perfect coherent light source in (a) and by a partially coherent light source in (b).

3. Fundamentals of spatial correlations

The investigation of the transverse spatial properties of light has accompanied the study of the nature of light itself. The development of the theory of diffraction and all resulting applications represent an impressive example of how finely a physical theory can describe nature. Despite the incredible success of classical optics, it has been found in the last few decades that amendments should be made in order to accurately describe the quantum effects which arise when dealing with some special light sources. In this respect, the transverse correlations between the twin photons produced in the parametric down-conversion process have largely contributed to this end. The quantum optics theory of spatial effects which has been developed so far is strongly based on classical diffraction theory, and has been shown to describe a large array of quantum phenomena in optics. In the following, we will briefly discuss some important topics in classical diffraction theory which will help in the development of the quantum theory of spatial correlations.

3.1. Transverse coherence and partial coherence: classical optics

In this section we will review some fundamental aspects of transverse coherence and partial coherence in classical optics. These concepts were essential in the development of quantum coherence theory and are still essential for the design and understanding of many quantum optics experiments. We introduce the discussion by analyzing the Young's double-slit experiment and its relationship with the van Cittert–Zernike [31] theorem, and the concept of coherence area.

3.1.1. Double slit experiment: perfect coherence

Fig. 2 shows a light source illuminating a double-slit aperture, and the resulting intensity pattern which is observed at the detection screen. When the light emitted by the source is perfectly coherent, interference fringes are observed with high visibility or contrast, as in Fig. 2(a). Many of the laser light sources available today are almost perfectly coherent, but many other important light sources are incoherent or partially coherent. Incoherent light sources can also be used to perform interference experiments under certain conditions. All real light beams present partial coherence, depending on the geometrical properties and propagation of the beam. Thus, interference fringes can still be observed, but with reduced visibility, as illustrated in Fig. 2(b). The light intensity distribution after a double-slit is given by Born and Wolf [32] and Wolf [31]:

$$I(x, y) = I_0(x, y)[1 + |\gamma_{12}(d)| \cos(\mathbf{k} \cdot \boldsymbol{\rho} + \delta)], \quad (27)$$

where $I_0(x, y)$ gives the single slit diffraction pattern, \mathbf{k} is the wave vector, $\boldsymbol{\rho}$ gives the position in the transverse plane, γ_{12} is the normalized mutual coherence of the light field in the plane of the slits, d is the distance between slits and δ is a fixed phase factor. When the source is perfectly coherent, $|\gamma_{12}| = 1$ and the contrast of the interference fringes is maximum. The contrast can be quantified by the visibility V , defined as $V = (I_{\max} - I_{\min}) / (I_{\max} + I_{\min})$, where I_{\max} and I_{\min} are the intensities at the interference maximum and minimum. When the coherence is partial, $0 \leq |\gamma_{12}| \leq 1$, and can be calculated from geometrical and statistical properties of the source [31].

One important result in the calculation of γ_{12} is known as the van Cittert–Zernike theorem. We will discuss this theorem in more detail.

3.1.2. Partial coherence and the van Cittert–Zernike theorem

Let us consider the situation sketched in Fig. 3, where a light source \mathcal{S} is illuminating the observation screen \mathcal{O} . We assume that the source is constituted by infinitesimal independent light emitters, such as a thermal source or parametric down-conversion, for example. The non-normalized mutual coherence function between points 1 and 2 on the screen is defined as:

$$\Gamma_{12}(d, \tau) = \sum_m \langle E_{m1}(t + \tau) E_{m2}^*(t) \rangle + \sum_{m \neq n} \langle E_{m1}(t + \tau) E_{n2}^*(t) \rangle, \quad (28)$$

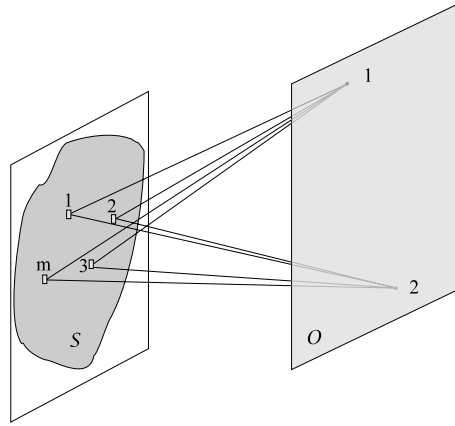


Fig. 3. Finite source S illuminating an observation screen O .

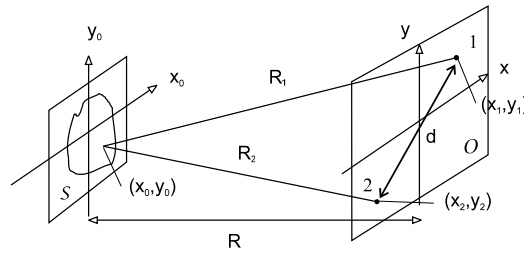


Fig. 4. Finite source illuminating an observation screen.

where the summations are performed over the emitting points of the source, d is the distance between points 1 and 2 at the screen, τ is the time difference due to different propagation distances from point m at the source to point 1 (or point 2) at the screen, E^* is the complex conjugate of E , and the brackets indicate time average.

If the field is quasi-monochromatic, the mutual coherence function can be written as

$$\Gamma_{12}(d, \tau) = \Gamma_{12}(d, 0)e^{ikc\tau}, \quad (29)$$

where $k = |\mathbf{k}|$ and c is the speed of light. This approximation is valid when the time difference τ is much smaller than the coherence time of the source. In other words, the phase relationship between $E_{m1}(t + \tau)$ and $E_{m2}(t)$ is preserved. However, for spatially incoherent sources such as thermal sources and SPDC, there is no phase relationship between $E_{m1}(t + \tau)$ and $E_{m2}(t)$ if $m \neq n$ and the second term in the left side of Eq. (28) averages to zero. Therefore, we end up with:

$$\Gamma_{12}(d, 0) = \sum_m \langle E_{m1} E_{m2}^* \rangle. \quad (30)$$

It is convenient to take the continuum limit and suppose that each point of the source emits a spherical wave. Thus, Eq. (30) takes the form:

$$\Gamma_{12}(d, 0) = \frac{1}{R^2} \int_{\mathcal{S}} d\mathbf{r}_0 I(\mathbf{r}_0) e^{ik(R_1 - R_2)}, \quad (31)$$

where $I(\mathbf{r}_0)$ is the intensity distribution of the source, $R_1 = |\mathbf{r}_0 - \mathbf{r}_1|$ and $R_2 = |\mathbf{r}_0 - \mathbf{r}_2|$ are the distances between point \mathbf{r}_0 in the source and points \mathbf{r}_1 and \mathbf{r}_2 , respectively, and it was assumed that $R_1 \sim R_2 = R \gg (R_1 - R_2)$.

It is interesting to write the difference $R_1 - R_2$ explicitly in terms of the coordinates of the generic source point (x_0, y_0) and the coordinates of the points 1 (x_1, y_1) and 2 (x_2, y_2) (see Fig. 4) and use again the relation $R_1 \sim R_2 = R \gg (R_1 - R_2)$. We then obtain the result known as the van Cittert–Zernike theorem:

$$\Gamma_{12}(d, 0) = \frac{e^{i\alpha}}{R^2} \iint_{\mathcal{S}} dx_0 dy_0 I(x_0, y_0) e^{ik(px_0 + qy_0)}, \quad (32)$$

where α is a constant phase and

$$p = \frac{(x_1 - x_2)}{R} \quad \text{and} \quad q = \frac{(y_1 - y_2)}{R}. \quad (33)$$

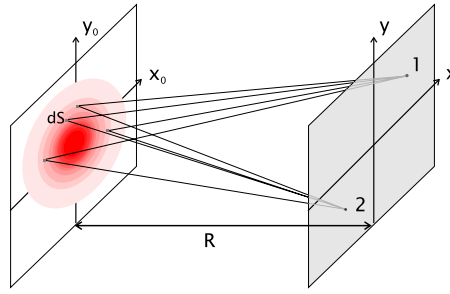


Fig. 5. Gaussian source illuminating an observation screen.

The dependence on the distance d appears through p and q . The van Cittert–Zernike theorem shows that the mutual coherence is given by the Fourier transform of the intensity distribution of the light source. This result is valid if the emitting points in the source are independent and if the mutual coherence is considered in a plane far enough from the source, so that Fraunhofer diffraction regime can be assumed. The normalized degree of coherence γ_{12} is:

$$\gamma_{12}(d, 0) = \frac{e^{i\alpha} \iint dx_0 dy_0 I(x_0, y_0) e^{ik(px_0 + qy_0)}}{\iint dx_0 dy_0 I(x_0, y_0)}. \quad (34)$$

The quantity $|\gamma_{12}(d)|$ gives the visibility of the interference fringes in a double slit experiment, Eq. (27), where we remember that d is the distance between slits.

3.1.3. The coherence area

Let us illustrate the application of the van Cittert–Zernike theorem in the calculation of the coherence area of a light source. Referring to Fig. 5, we start by calculating the degree of coherence for a light source with a Gaussian intensity distribution. The integrals in Eq. (34) are computed using the initial intensity distribution

$$I(x_0, y_0) = A \exp\left(-\frac{x_0^2 + y_0^2}{\sigma^2}\right), \quad (35)$$

and we obtain

$$\gamma_{12}(d, 0) = \exp\left(-\frac{k^2 \sigma^2 d^2}{4R^2}\right). \quad (36)$$

The coherence area is the area within which the value of $|\gamma_{12}|$ is appreciable and the field can be considered spatially coherent. From Eq. (36), we can see that, on the one hand, the degree of coherence decreases with the wave number k , source width σ and distance d between points 1 and 2. On the other hand, the degree of coherence increases with the propagation distance R . As the coherence function is Gaussian, it never reaches zero and we can take the value $\gamma_{12}(d, 0) = 1/e$ as a lower bound for the coherence. Then the circular coherence area $\mathcal{A}_c = \pi(\frac{d}{2})^2$ can be deduced from Eq. (36) by imposing $\gamma_{12}(d, 0) = 1/e$:

$$\mathcal{A}_c = \frac{\pi R^2}{k^2 \sigma^2}. \quad (37)$$

In terms of a double slit experiment, this result indicates that there will be interference fringes with considerable visibility as long as the slits are placed within the area given by Eq. (37).

The double-slit experiment provides a method for determining the coherence area of a light field at some distance from the source. A double-slit aperture with variable slit separation d is placed at the plane of interest, the visibility of the resulting interference patterns is measured in the far-field. By plotting the visibilities of the interference patterns as a function of d , a measurement of the transverse coherence length of the field in the one direction is obtained. Repeating the procedure in the perpendicular direction in the transverse plane, we obtain a measurement of the coherence area. This method was used to measure the transverse coherence length of one of the down-converted fields produced by SPDC [33], and it was observed that the coherence length is the same as that predicted for a thermal source. The same method was also applied to the two-photon beam produced by SPDC, and it was shown that the transverse coherence length of the two-photon field is much larger than the one-photon field [34]. A quantum multimode theory was necessary to explain the experimental results in this case.

3.2. The Fresnel and paraxial approximations

Another important and basic issue in spatial correlations concerns the Fresnel and paraxial approximations. Most of the quantum optics theory concerning SPDC was developed within these approximations and describes very well the vast

majority of the experimental situations reported so far. In the following sections, we will derive the quantum state for the transverse degrees of freedom of the twin photons produced by parametric down-conversion, according to the Fresnel and paraxial approximations.

Let us assume that a monochromatic light beam is propagating along the z direction in an isotropic medium. We can write the k_z component as

$$k_z = \sqrt{k^2 - q^2} \approx k \left(1 - \frac{q^2}{2k^2} \right). \quad (38)$$

The above approximation, known as the Fresnel approximation, is obtained by simple Taylor expansion and is valid when $q^2 \ll k^2$.

The Fresnel approximation is essentially a particular application of the more general paraxial approximation. In geometric optics, where light is represented by rays, paraxial rays are those that lie at small angles to the optical axis of the optical system under consideration. If we were to draw rays from the origin to points \mathbf{k} in k -space satisfying the approximation in expression (38), they would be paraxial rays. In this respect the paraxial approximation and the Fresnel approximation are essentially the same. Throughout this work we will refer to both as the paraxial approximation. A thorough account of the paraxial approximation can be found in most classical optics textbooks [35,36]. Here we will present only the bare essentials. The paraxial approximation can be extended to wave optics if one considers only waves whose wavefront normals are paraxial rays. In wave optics, an optical wave $E(\mathbf{r}, t)$ satisfies the wave equation:

$$\nabla^2 E(\mathbf{r}, t) - \frac{1}{c^2} \frac{\partial^2}{\partial t^2} E(\mathbf{r}, t) = 0. \quad (39)$$

If one considers that the optical wave is monochromatic with harmonic time dependence, so that $E(\mathbf{r}, t) = \mathcal{E}(\mathbf{r}) \exp(-i\omega t)$, where ω is the angular frequency, one arrives at the Helmholtz equation:

$$\nabla^2 \mathcal{E}(\mathbf{r}) + k^2 \mathcal{E}(\mathbf{r}) = 0. \quad (40)$$

If we now consider only paraxial waves propagating near the z axis, we can write $\mathcal{E}(\mathbf{r}) = \mathcal{U}(\mathbf{r}) \exp(ikz)$, where $\mathcal{U}(\mathbf{r})$ is a slowly varying function of \mathbf{r} such that $\mathcal{E}(\mathbf{r})$ maintains a plane wave structure for distances within that of a wavelength. Using this form of $\mathcal{E}(\mathbf{r})$ in the Helmholtz equation, one arrives at the paraxial Helmholtz equation

$$\left(\frac{\partial^2}{\partial x^2} + \frac{\partial^2}{\partial y^2} + 2ik \frac{\partial}{\partial z} \right) \mathcal{U}(\mathbf{r}) = 0. \quad (41)$$

In obtaining (41), we have used the fact that the term $\partial^2 \mathcal{U}(\mathbf{r}) / \partial z^2$ is very small within distances of a wavelength: $\partial^2 \mathcal{U}(\mathbf{r}) / \partial z^2 \ll k \partial \mathcal{U}(\mathbf{r}) / \partial z$. The paraxial Helmholtz equation admits several well known solutions, including the Hermite–Gaussian and Laguerre–Gaussian beams. Quantum fields prepared in these modes have been proposed for several applications and will be discussed in more detail later. It has been shown by several authors that the paraxial Helmholtz equation is analogous to the Schrödinger equation in quantum mechanics [37–39]. In Ref. [37] an alternative derivation of equation (41) is provided which requires that the optical wave is only nearly monochromatic.

3.3. The angular spectrum and its propagation

The quantum theory which accounts for the transverse correlations of photons makes use of several techniques of Fourier Optics, in particular the propagation of the angular spectrum. Fourier Optics [36] provides a useful method of calculating the propagation of an optical field through a given optical system. Here we consider a monochromatic scalar field far from its source, satisfying the Helmholtz equation (40), for which the field amplitude can be represented [36] as

$$\mathcal{U}(\boldsymbol{\rho}, z) = \frac{1}{(2\pi)^2} \int_{\mathbb{R}^2} d\mathbf{q} v(\mathbf{q}, z) \exp[i\mathbf{q} \cdot \boldsymbol{\rho}], \quad (42)$$

where we assume that the field is propagating along the z direction and have defined $\boldsymbol{\rho}$ and \mathbf{q} as the transverse components of \mathbf{r} and \mathbf{k} , respectively. The angular spectrum $v(\mathbf{q}, z)$ is the inverse Fourier transform of the electric field:

$$v(\mathbf{q}, z) = \int_{\mathbb{R}^2} d\boldsymbol{\rho} \mathcal{U}(\boldsymbol{\rho}, z) \exp[-i\mathbf{q} \cdot \boldsymbol{\rho}]. \quad (43)$$

One can also understand the angular spectrum by recognizing Eq. (42) as an expansion of $\mathcal{U}(\boldsymbol{\rho}, z)$ in terms of plane waves $\exp(i\mathbf{q} \cdot \boldsymbol{\rho})$, in which the angular spectrum $v(\mathbf{q}, z)$ acts as a weight function.

As the field propagates, its angular spectrum changes accordingly. Combining Eqs. (41) and (42), it is easy to show that if the angular spectrum of a field is known at $z = 0$, it propagates as

$$v(\mathbf{q}, z) = v(\mathbf{q}, 0) \exp(ik_z z). \quad (44)$$

In order to be useful, k_z must be expressed in terms of the transverse component \mathbf{q} . For isotropic media, this can be done using Eq. (38).

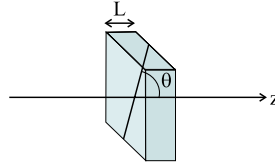


Fig. 6. Non-linear crystal and its optical axis. z axis represents the direction of propagation of light.

Dealing with anisotropic media, which is the case of the nonlinear crystals used for parametric down-conversion, the expressions for k_z in terms of \mathbf{q} can be quite complicated [32]. We will restrict our analysis to uniaxial media for two reasons: first, in the majority of the work on spatial correlation properties of two-photon states, the photon pairs are generated by spontaneous parametric down-conversion in uniaxial crystals. Second, the physics of down-conversion in biaxial crystals, though more involved, to our knowledge does not contain any essentially new effect. We will consider the geometry depicted in Fig. 6, where a slab of a uniaxial crystal of thickness L is cut to have its optic axis making an angle θ with its normal, which is oriented parallel to the z axis. In this medium, the wave vector surface has two sheets, defined by

$$\frac{q_x^2 + q_y^2 + k_z^2}{n_o^2} = \frac{\omega^2}{c^2}, \quad (45)$$

which allows us to immediately write

$$k_z = \sqrt{\left(n_o \frac{\omega}{c}\right)^2 - |\mathbf{q}|^2} \approx n_o \frac{\omega}{c} - \frac{c}{2n_o \omega} |\mathbf{q}|^2, \quad (46)$$

and

$$\left(\frac{\cos^2 \theta}{n_e^2} + \frac{\sin^2 \theta}{n_o^2}\right) q_x^2 + \frac{q_y^2}{n_e^2} + \left(\frac{\cos^2 \theta}{n_o^2} + \frac{\sin^2 \theta}{n_e^2}\right) k_z^2 + \left(\frac{1}{n_e^2} - \frac{1}{n_o^2}\right) \sin(2\theta) q_x k_z = \frac{\omega^2}{c^2}, \quad (47)$$

where n_o and n_e are the ordinary and extraordinary refractive indices, respectively. Eq. (45) applies to plane waves with ordinary polarization (orthogonal to the optical axis), whereas Eq. (47) applies to plane waves with extraordinary polarization. In the latter case, Eq. (47) can be solved for k_z , leading to

$$\begin{aligned} k_z &= \alpha q_x + \sqrt{\left(\eta \frac{\omega}{c}\right)^2 - \beta^2 q_x^2 - \gamma^2 q_y^2} \\ &\approx \alpha q_x + \eta \frac{\omega}{c} - \frac{c}{2\eta \omega} (\beta^2 q_x^2 - \gamma^2 q_y^2), \end{aligned} \quad (48)$$

where

$$\alpha = \frac{(n_o^2 - n_e^2) \sin \theta \cos \theta}{n_o^2 \sin^2 \theta + n_e^2 \cos^2 \theta}, \quad (49)$$

$$\beta = \frac{n_o n_e}{n_o^2 \sin^2 \theta + n_e^2 \cos^2 \theta}, \quad (50)$$

$$\gamma = \frac{n_o}{\sqrt{n_o^2 \sin^2 \theta + n_e^2 \cos^2 \theta}}, \quad (51)$$

$$\eta = \frac{n_o n_e}{\sqrt{n_o^2 \sin^2 \theta + n_e^2 \cos^2 \theta}}. \quad (52)$$

The term α is responsible for the so-called *walk-off*. The terms β and γ are close to 1 and cause a slight astigmatism in the beams propagating through the uniaxial medium. Their effect is marginal, and both β^2 and γ^2 can be approximated by 1. Therefore, for extraordinary polarization,

$$k_z \approx \eta \frac{\omega}{c} + \alpha q_x - \frac{c}{2\eta \omega} |\mathbf{q}|^2. \quad (53)$$

3.4. Quantum state of photon pairs: spatial degrees of freedom

The spatial properties of the two-photon state depend strongly on the birefringence of the non-linear crystal and type of phase matching [40–44]. Let us consider first the case of type I phase matching, where the pump field has extraordinary

polarization and the down-converted fields have ordinary polarization ($e \rightarrow oo$). In this case,

$$k_{pz} \approx \eta_p \frac{\omega_p}{c} - \alpha_p q_{px} - \frac{c}{2\eta_p \omega_p} |\mathbf{q}_s + \mathbf{q}_i|^2, \quad (54)$$

$$k_{sz} \approx n_s \frac{\omega_s}{c} - \frac{c}{2n_s \omega_s} |\mathbf{q}_s|^2, \quad (55)$$

$$k_{iz} \approx n_i \frac{\omega_i}{c} - \frac{c}{2n_i \omega_i} |\mathbf{q}_i|^2, \quad (56)$$

where n_j ($j = s, i$) stands for the ordinary refractive index.

Using Eqs. (54)–(56) in Eq. (20) and considering a monochromatic pump beam, we arrive at the two-photon detection amplitude for type I phase matching:

$$\begin{aligned} \Phi_{oo}(\mathbf{q}_s, \mathbf{q}_i) \approx & C_{oo} G_s(\omega_s) G_i(\omega_i) v(\mathbf{q}_s + \mathbf{q}_i) \delta(\omega_s + \omega_i - \omega_p) \text{sinc} \left[\mu_{oo} + l_t(q_{sx} + q_{ix}) + \frac{L}{4K} \left| \frac{\mathbf{q}_s}{r_s} - \frac{\mathbf{q}_i}{r_i} \right|^2 \right] \\ & \times \exp[-il_t(q_{sx} + q_{ix})], \end{aligned} \quad (57)$$

where $K = \eta_p \omega_p / c$ is the pump beam wave number inside the crystal, $r_s = \sqrt{\omega_s / \omega_i}$, $r_i = \sqrt{\omega_i / \omega_s}$, $\mu_{oo} = (\bar{n} - \eta_p)KL / 2\eta_p$, and $l_t = \alpha_p L / 2$ is the transverse walk-off length [45,43]. The ordinary refractive index \bar{n} is calculated at the frequency $\omega_p / 2$. In collinear phase matching, $\mu_{oo} = 0$. Eq. (57) is accurate up to first order in $(\omega_s - \omega_i) / 2\omega_p$.

For each particular set of frequencies ω_s, ω_i , the function $\Phi_{oo}(\mathbf{q}_s, \mathbf{q}_i)$ can be regarded as the normalized angular spectrum of the two-photon field. Note that the angular spectrum of the pump beam is present in Φ_{oo} , meaning that it is transferred to the fourth-order spatial correlation properties of the two-photon state [16]. The amplitude Φ_{oo} is not a separable function of \mathbf{q}_s , and \mathbf{q}_i , that is to say, $\Phi_{oo} \neq F_s(\mathbf{q}_s)F_i(\mathbf{q}_i)$. This non-separability is responsible for many of the nonlocal and non-classical effects observed with the state (60).

For simplicity, let us assume that the crystal is thin enough to allow us to ignore the effects of birefringence. If narrow-band interference filters selecting $\omega_s = \omega_i = \omega_p / 2$ are used, the two-photon state generated by SPDC in quasi-collinear phase matching ($\mu_{oo} \approx 0$) can be written in a very simple form as [16,46]

$$|\psi\rangle_{\text{SPDC}} = C_v |vac\rangle + C_2 |\psi\rangle_1, \quad (58)$$

where

$$|\psi\rangle_1 = \iint d\mathbf{q}_s d\mathbf{q}_i v(\mathbf{q}_s + \mathbf{q}_i) \gamma(\mathbf{q}_s - \mathbf{q}_i) |\mathbf{q}_s, \mathbf{e}_o\rangle |\mathbf{q}_i, \mathbf{e}_o\rangle, \quad (59)$$

$\gamma(\mathbf{q}) = \sqrt{2L/\pi^2 K} \text{sinc}(Lq^2/4K)$, and $|\mathbf{q}_j, \mathbf{e}_o\rangle$ represent Fock states in plane wave modes labeled by the transverse component \mathbf{q}_j of the wave vector \mathbf{k}_j , and ordinary polarization vector \mathbf{e}_o . If the nonlinear crystal is sufficiently thin, so that the width of the sinc function in Eq. (57) can be much greater than the width of the pump beam angular spectrum, the sinc function can then be approximated by unity. This is known as the *thin crystal approximation*. The quantum state (59) simplifies to

$$|\psi\rangle_{\text{tc}} = \iint_D d\mathbf{q}_s d\mathbf{q}_i v(\mathbf{q}_s + \mathbf{q}_i) |\mathbf{q}_s, \mathbf{e}_o\rangle |\mathbf{q}_i, \mathbf{e}_o\rangle. \quad (60)$$

D is a domain in the \mathbf{q} space within which the thin-crystal approximation is valid, meaning that the two-photon angular spectrum $\Phi_{oo}(\mathbf{q}_s, \mathbf{q}_i)$ mimics the pump beam angular spectrum $v(\mathbf{q})$ in the sum of transverse wave vectors $\mathbf{q}_s + \mathbf{q}_i$. Since all the information about a monochromatic beam is contained in its angular spectrum, the transverse and longitudinal spatial properties of the pump beam are transferred to the two-photon field, in this context, defining a *correlation beam*.

In the general case, however, when the crystal length is not negligible, the sinc function in Eq. (57) has to be considered in detail. Due to the presence of the linear term $l_t(q_{sx} + q_{ix})$, that function is, in general, much narrower in the x direction than it is in the y direction. This fact causes the two-photon coincidence detection amplitude to not emulate the pump beam angular spectrum completely [47,44]. For example, in the collinear ($\mu_{oe} = \mu_{eo} = 0$) degenerate monochromatic ($\omega_s = \omega_i = \omega_p / 2$) case, when the detectors are scanned in the same direction in the \mathbf{q} space ($\mathbf{q}_s = \mathbf{q}_i = \mathbf{q}$), the amplitude Φ_{oo} is proportional to

$$v(2\mathbf{q}) \text{sinc}(2l_t q_x) \exp(-2il_t q_x). \quad (61)$$

It is clear that the angular spectrum will be clipped by the sinc function and subjected to transverse walk-off.

In type II phase matching, one of the down-converted fields has ordinary polarization and the other one has extraordinary polarization ($e \rightarrow oe$). In this case, one has two amplitudes:

$$\begin{aligned} \Phi_{oe} \approx & C_{oe} G_s(\omega_s) G_i(\omega_i) v(\mathbf{q}_s + \mathbf{q}_i) \delta(\omega_s + \omega_i - \omega_p) \text{sinc} \left(\mu_{oe} + l_t q_{sx} + l'_t q_{ix} + \frac{L}{4K} \left| \frac{\mathbf{q}_s}{r_s} - \frac{\mathbf{q}_i}{r_i} \right|^2 \right) \\ & \times \exp[-i(\mu_{oe} + l_t q_{sx} + l'_t q_{ix})], \end{aligned} \quad (62)$$

and

$$\begin{aligned} \Phi_{eo} \approx & C_{eo} G_s(\omega_s) G_i(\omega_i) v(\mathbf{q}_s + \mathbf{q}_i) \delta(\omega_s + \omega_i - \omega_p) \text{sinc} \left(\mu_{eo} + l'_t q_{sx} + l_t q_{ix} + \frac{L}{4K} \left| \frac{\mathbf{q}_s}{r_s} - \frac{\mathbf{q}_i}{r_i} \right|^2 \right) \\ & \times \exp[-i(\mu_{eo} + l'_t q_{sx} + l_t q_{ix})], \end{aligned} \quad (63)$$

where

$$\mu_{oe} = \left[\frac{\bar{n} + \bar{\eta}}{2} - \eta_p + \frac{\omega_s - \omega_i}{2\omega_p} (\bar{n} - \bar{\eta}) \right] \frac{KL}{2\eta_p}, \quad (64)$$

$$\mu_{eo} = \left[\frac{\bar{n} + \bar{\eta}}{2} - \eta_p - \frac{\omega_s - \omega_i}{2\omega_p} (\bar{n} - \bar{\eta}) \right] \frac{KL}{2\eta_p}, \quad (65)$$

$l_t = \alpha_p L/2$, and $l'_t = (2\alpha_p - \bar{\alpha})L/4 \approx l_t/2$. The walk-off parameter $\bar{\alpha}$ and the refractive indices \bar{n} (ordinary) and $\bar{\eta}$ (extraordinary) are calculated at the frequency $\bar{\omega} = \omega_p/2$. Note the linear dependence of μ_{oe} and μ_{eo} on $\omega_s - \omega_i$. For the crossed cone configuration [48], the state generated by type II SPDC is, according to Eq. (63),

$$|\psi\rangle_{\text{SPDC}} \approx C_v |vac\rangle + C_2 |\psi\rangle_{\text{II}}, \quad (66)$$

where

$$|\psi\rangle_{\text{II}} \approx \int d\omega_s \int d\omega_i \int d\mathbf{q}_s \int d\mathbf{q}_i (\Phi_{oe} |\mathbf{q}_s, \omega_s, \mathbf{e}_o\rangle |\mathbf{q}_i, \omega_i, \mathbf{e}_e\rangle + \Phi_{eo} |\mathbf{q}_s, \omega_s, \mathbf{e}_e\rangle |\mathbf{q}_i, \omega_i, \mathbf{e}_o\rangle). \quad (67)$$

Again, if the crystal is thin enough and narrow-band filters are used, the state $|\psi\rangle_{\text{II}}$ in collinear frequency-degenerate phase matching reduces to

$$|\psi\rangle_{\text{II}} \approx \iint_D d\mathbf{q}_s d\mathbf{q}_i v(\mathbf{q}_s + \mathbf{q}_i) (|\mathbf{q}_s, \mathbf{e}_o\rangle |\mathbf{q}_i, \mathbf{e}_e\rangle + |\mathbf{q}_s, \mathbf{e}_e\rangle |\mathbf{q}_i, \mathbf{e}_o\rangle). \quad (68)$$

Eqs. (62) and (63) predict different transverse and longitudinal walk-off for ordinary and extraordinary down-converted photons. In type II phase matching, these effects can be considerable, and may decrease the quality of the entanglement between the photons.

3.5. Coincidence detection probability and probability amplitude

The coincidence count rate is proportional to the fourth-order correlation function

$$C(\boldsymbol{\rho}_s, \boldsymbol{\rho}_i) = \langle \psi | \mathbf{E}^{(-)}(\boldsymbol{\rho}_s) \mathbf{E}^{(-)}(\boldsymbol{\rho}_i) \mathbf{E}^{(+)}(\boldsymbol{\rho}_s) \mathbf{E}^{(+)}(\boldsymbol{\rho}_i) | \psi \rangle, \quad (69)$$

where \mathbf{E} is the electric field operator and $\boldsymbol{\rho}_s$ and $\boldsymbol{\rho}_i$ are the transverse coordinates on the signal and idler detection planes respectively. Since $|\psi\rangle$ is a two-photon state, the correlation function (74) can be put in the form [41]

$$C(\boldsymbol{\rho}_s, \boldsymbol{\rho}_i) = |\Psi(\boldsymbol{\rho}_s, \boldsymbol{\rho}_i)|^2, \quad (70)$$

where $C(\boldsymbol{\rho}_s, \boldsymbol{\rho}_i)$ can be interpreted as the two-photon detection probability and

$$\Psi(\boldsymbol{\rho}_s, \boldsymbol{\rho}_i) = \langle vac | \mathbf{E}^{(+)}(\boldsymbol{\rho}_s) \mathbf{E}^{(+)}(\boldsymbol{\rho}_i) | \psi \rangle, \quad (71)$$

as the two-photon detection amplitude. Eq. (71) can be viewed as the two-photon, or *bi-photon* wavefunction. The electric field operator is given by

$$\mathbf{E}^{(+)}(\boldsymbol{\rho}) = C \int d\mathbf{q} \mathbf{a}(\mathbf{q}) \exp \left[i(\mathbf{q} \cdot \boldsymbol{\rho} + \sqrt{k^2 - q^2} z) \right], \quad (72)$$

where C is a constant and z is the propagation distance.

3.6. The role of the spatial properties of the pump field

The quantum states derived in Section 3.4 show a dependence on the angular spectrum of the pump beam. This dependence indicates that the photon pairs can be prepared in a variety of quantum states through the manipulation of the pump beam. This preparation has measurable effects in the coincidence counting rate [16,49]. In order to illustrate this idea, we will describe one experiment in which the spatial shape of the coincidence distribution in the detection plane was prepared through manipulation of the pump beam [16].

The set-up is shown in Fig. 7. The pump laser passes through a mask and a lens, before pumping the non-linear crystal. The mask has an aperture with the shape of the letter “C”. The lens is used to form the image of the mask in a plane situated

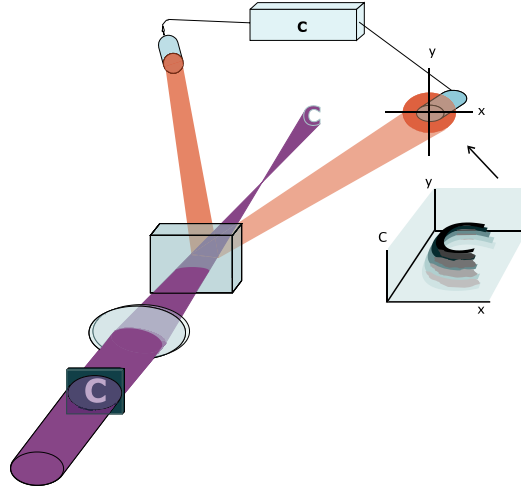


Fig. 7. Illustration of an experiment to show the transfer of the angular spectrum from the pump beam to the spatial correlations of down converted photons [16].

after the crystal. The down-converted beams are detected on the plane where the image of the mask “C”, in the transverse coincidence distribution. In this condition, it is possible to recover the shape of the image “C”, in the transverse coincidence distribution. In order to image the coincidence distribution, the idler (or signal) detector is kept fixed, while the signal (or the idler) detector is scanned in two dimensions on the detection plane. A typical result is displayed in the inset in Fig. 7. The angular spectrum of the pump laser is transferred to the correlations between signal and idler photons, while the local intensities of each photon field are not affected [16].

The coincidence count rate can be calculated using the state given in Eq. (60) together with several approximations simplifying the function $\Phi(\mathbf{q}_s, \mathbf{q}_i)$ given by Eq. (57). Assuming the thin crystal approximation, the SPDC state can be described by

$$|\psi\rangle = C_2 \int \int_D d\mathbf{q}_s d\mathbf{q}_i v(\mathbf{q}_s + \mathbf{q}_i) |\mathbf{q}_s, \sigma_s\rangle_s |\mathbf{q}_i, \sigma_i\rangle_i, \quad (73)$$

where C_2 is a constant. We neglect $|vac\rangle$ in Eq. (73), since it does not contribute to coincidence counts.

Using Eqs. (73), (69) and (72), the coincidence rate can be calculated:

$$\begin{aligned} C(\mathbf{p}_s, \mathbf{p}_i) &= |C_2|^2 \left| \int d\mathbf{p} \mathcal{W}(\mathbf{p}) \exp\left(-i \frac{K}{2Z_0} |\mathbf{R} - \mathbf{p}|^2\right) \right|^2 \\ &= |C_2|^2 |\mathcal{W}(\mathbf{R}; Z_0)|^2, \end{aligned} \quad (74)$$

where $\mathcal{W}(\mathbf{R}; Z_0)$ is the transverse spatial profile of the pump beam propagated to $Z = Z_0$, and

$$\begin{aligned} \frac{1}{Z_0} &= \frac{\omega_s}{\omega_p} \frac{1}{z_s} + \frac{\omega_i}{\omega_p} \frac{1}{z_i}, \\ \mathbf{R} &= \frac{\omega_s}{\omega_p} \frac{Z_0}{z_s} \mathbf{p}_s + \frac{\omega_i}{\omega_p} \frac{Z_0}{z_i} \mathbf{p}_i, \end{aligned} \quad (75)$$

where z_s and z_i are distances between the crystal and signal and idler detection planes, respectively.

Eq. (74) shows that the coincidence distribution depends on the Fresnel propagator of the transverse profile of the pump field. This structure coincides with the image prepared in the pump, depending on the relationship between the wavelengths of the three fields and the free propagation distances. This allows the engineering of spatial correlations by manipulating the pump laser beam. Another important aspect is that the coincidence distribution depends on the sum of the signal and idler detector coordinates, and not either detector position alone, which is a signature of the spatial entanglement between the down-converted photons.

4. Double slit experiments with twin photons

Spatial properties of twin photons were experimentally investigated already at the time of the first experimental observation of parametric down-conversion by Burnham and Weinberg [1]. They observed that the intensity correlations were stronger for certain combinations of detection angles. A more comprehensive study of these far field correlations were

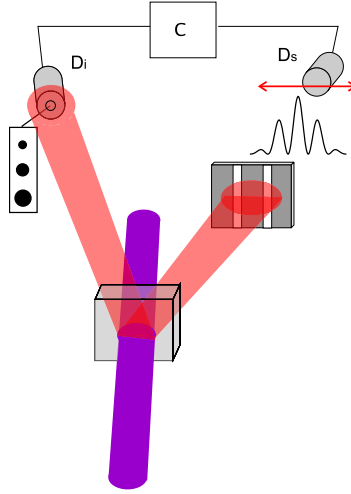


Fig. 8. Double slit experiment with twin photons. In Ref. [13], the signal detector D_s was scanned to observe interference fringes.

made by Grayson and Barbosa [10]. Experiments exploring interference at a double slit experiment using twin photons and coincidence counting came in 1994 [13] and 1995 [14] and was further investigated in later work [50,34,19,17,51–53,18,54,55]. In this section, we review some of the key experiments exploring aspects of interference of photon pairs using a double slit.

4.1. Nonlocal dependence of spatial coherence

There are several possible ways to send one or two photons through a Young's double slit. Historically, the first choice is to send one of the photons—say the signal photon—through the double slit aperture, and let the idler propagate freely to the detection plane [13], as illustrated in Fig. 8. The two-photon coincidence distribution can be obtained in the same way as in Section 3.6. In order to take into account the presence of the slits in the signal beam, we include the diffraction integral in the electric field operator [46]:

$$\mathbf{E}^{(+)}(\boldsymbol{\rho}) = \int d\mathbf{q} d\mathbf{q}' \mathbf{a}(\mathbf{q}') \mathcal{T}(\mathbf{q} - \mathbf{q}') \exp \left\{ i \left[\mathbf{q} \cdot \boldsymbol{\rho} - \frac{q^2}{2k} Z - \frac{q'^2}{2k} z_A \right] \right\}, \quad (76)$$

where $\mathcal{T}(\mathbf{q})$ is the Fourier transform of the double slit aperture $A(\boldsymbol{\rho})$, z_A is the longitudinal coordinate of the slits, and $Z = z - z_A$. Using this operator and the quantum state (73) in Eq. (71), we arrive at:

$$\Psi(\boldsymbol{\rho}_s, \boldsymbol{\rho}_i) \propto \iint d\boldsymbol{\rho}'_s d\boldsymbol{\rho}'_i A(\boldsymbol{\rho}'_s) \mathcal{W} \left(\frac{1}{2} \boldsymbol{\rho}'_s + \frac{1}{2} \boldsymbol{\rho}'_i, z_A \right) e^{-i \frac{k}{4Z} (|\boldsymbol{\rho}_s - \boldsymbol{\rho}'_s|^2 + |\boldsymbol{\rho}_i - \boldsymbol{\rho}'_i|^2)}, \quad (77)$$

where $\mathcal{W}(\boldsymbol{\rho}, z_A)$ is the transverse profile of the pump beam propagated to $z = z_A$ and we have assumed that $k_s = k_i = K/2$ and $z_s = z_i \equiv z$. Assuming that the distance Z is such that the Fraunhofer approximation is valid, the detection probability is

$$C(\boldsymbol{\rho}_s, \boldsymbol{\rho}_i) \propto \left| v \left(\frac{k}{Z} \boldsymbol{\rho}_i \right) \mathcal{T} \left(\frac{k}{Z} \boldsymbol{\rho}_s - \frac{k}{Z} \boldsymbol{\rho}_i \right) \right|^2. \quad (78)$$

Approximating the aperture function by $A(\boldsymbol{\rho}_s) = \delta(x_s + d) + \delta(x_s - d)$ gives $\mathcal{T}(\mathbf{q}) \propto \cos(q_x d)$. In this case the detection probability is

$$C(\boldsymbol{\rho}_s, \boldsymbol{\rho}_i) \propto \left| v \left(\frac{k}{Z} \boldsymbol{\rho}_i \right) \right|^2 \cos^2 \left[\frac{kd}{2Z} (x_s - x_i) \right]. \quad (79)$$

From Eq. (79) we see that the typical oscillations of a double slit interference pattern is found, as a function of the difference between the transverse coordinates of the signal and idler detectors. In Ref. [13], the coincidence patterns were obtained by scanning the signal detector D_s after the slits. A qualitative comparison between the intensity fringes and the coincidence fringes observed as a function of the width of the idler detector aperture is shown in Fig. 9. These results show that the visibility of the coincidence fringes depends on the diameter of the idler detector, while the visibility of the intensity (single-photon) fringes depends only on the source properties. The visibility is high for a narrow aperture and low for a large

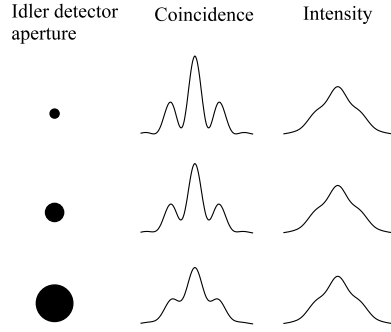


Fig. 9. Qualitative comparison between intensity (single-photon) and coincidence fringes obtained by scanning the signal detector D_s as a function of the aperture of the idler detector D_i .

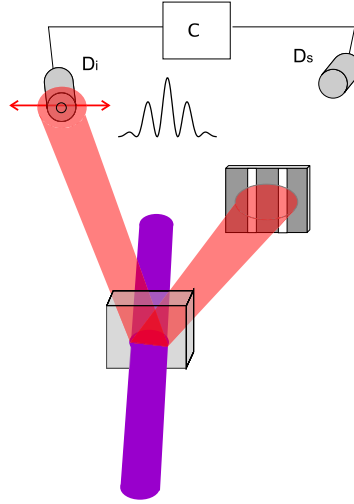


Fig. 10. Double slit experiment used to observe ghost interference fringes.

aperture, implying a nonlocal dependence of the spatial coherence. The detection probability in this case is obtained from Eq. (79) by integrating over the size of the idler detector

$$C_D(\boldsymbol{\rho}_s, \boldsymbol{\rho}_i) \propto \int d\boldsymbol{\rho}_i D(\boldsymbol{\rho}_i - \boldsymbol{\sigma}) \left| v \left(\frac{k}{Z} \boldsymbol{\rho}_i \right) \right|^2 \cos^2 \left(\frac{kd}{2Z} x_s - \frac{kd}{2Z} x_i \right), \quad (80)$$

where $D(\boldsymbol{\rho}_i)$ is the function describing the idler detector centered at position $\boldsymbol{\sigma}$ in the detection plane. For a very narrow detection aperture, $D(\boldsymbol{\rho}_i) \sim \delta(\boldsymbol{\rho}_i - \boldsymbol{\sigma})$, and $C_D(\boldsymbol{\rho}_s, \boldsymbol{\rho}_i) \propto \cos^2[kd/2Z(x_s - \sigma_x)]$, resulting in maximum visibility. In other words, the post-selection by the narrow aperture in the idler mode projects the signal beam in a state with a narrower angular bandwidth. For a very broad detector, so that the width of D is much larger than the width of the angular spectrum v , we can approximate $D \sim 1$. In this case Eq. (80) gives a convolution, which washes out the oscillations of the cosine function, giving low visibility. A simple way of relating the idler detector diameter and the visibility of the coincidence fringes, following the lines of the classical van Cittert–Zernike theorem, was developed in Ref. [56].

4.2. Ghost interference

Another possibility in terms of double slit experiments using twin photons and coincidence detection is the scanning of the idler detector instead of the signal detector [14], as shown in Fig. 10. The coincidence distribution displays interference fringes, while the intensity distribution of the idler field would never present interference fringes, since the double slit aperture is in the other beam. These fringes can be understood in terms of Eq. (79), which shows that the parameters of the coincidence interference pattern depend on the difference between the signal and idler detectors coordinates. Thus, by fixing the signal detector, and scanning the idler, the interference fringes appear as a function of the position of the idler detector, even though the idler photon never passes through the double slit aperture. This type of experiment was named “ghost” interference, in reference to the “spooky” action at a distance attributed by Einstein to the non-local nature of entangled particles.

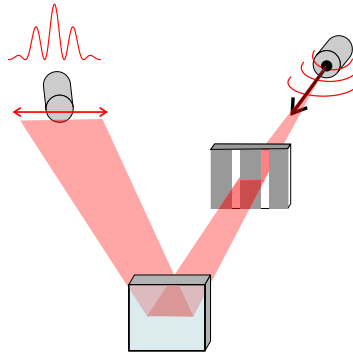


Fig. 11. Advanced wave picture.

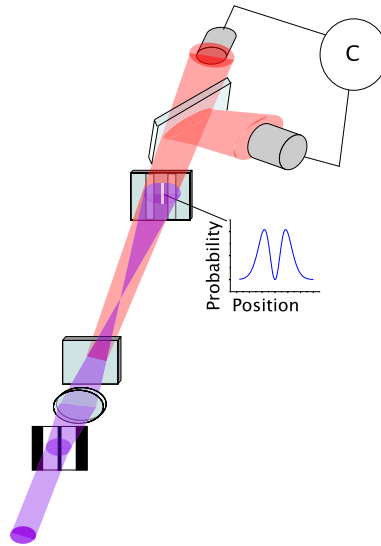


Fig. 12. Experimental setup for two-photon interference at a double slit. The resulting interference pattern has oscillations corresponding to the spatial frequency of a two-photon wave packet.

4.2.1. The advanced wave picture

A method that aids in the understanding and design of experiments exploring the spatial correlations between twin photons was introduced by Belinski and Klyshko [57]. This method, known as the “Advanced Wave Picture” (AWP), consists of associating the coincidence detection and post selection to a temporal inversion of the propagation of one of the beams. In the case of the experiment of Fig. 10, the AWP considers the system as if the fixed detector (signal) behind the slits was an incoherent light source and the scanning detector (idler) was registering the resulting intensity. The crystal plays the role of a mirror, as shown in Fig. 11. The coincidence pattern obtained when the idler detector is scanned will be equal to the hypothetical intensity pattern obtained according to the AWP scheme described above. The AWP works independently of the optical components placed in the signal and idler beams. It is important to notice that the crystal is treated as a mirror and the kind of mirror depends on the shape of the pump beam. This dependency was discussed in Section 3.6. For example, in Ref. [49] it was shown that the curvature of the “mirror” is directly related to the curvature of the pump beam.

4.3. The de Broglie wavelength of a two-photon wave packet

Interesting possibilities arise when one sends both photons through the double slit aperture. Using the spatial correlations between the twin photons, it is possible to perform a double slit experiment in which the two photons always pass through the same slit [17]. In this way, the interference for a wave packet containing two photons can be observed. The signature of the two-photon interference is the spatial frequency of the fringes, which is twice the frequency of the fringes that arise in single photon interference. The spatial frequency is directly related to the de Broglie wavelength $\lambda_{db} = \lambda/N$ of the N -photon wave packet [58]. An experiment which observed the de Broglie wavelength of a two-photon wave packet was reported in Ref. [17], and is sketched in Fig. 12. A twin photon pair is produced in collinear SPDC. The beam containing the down-converted photons is sent through a double slit aperture with slit separation of $2d$, after which the photons are split on

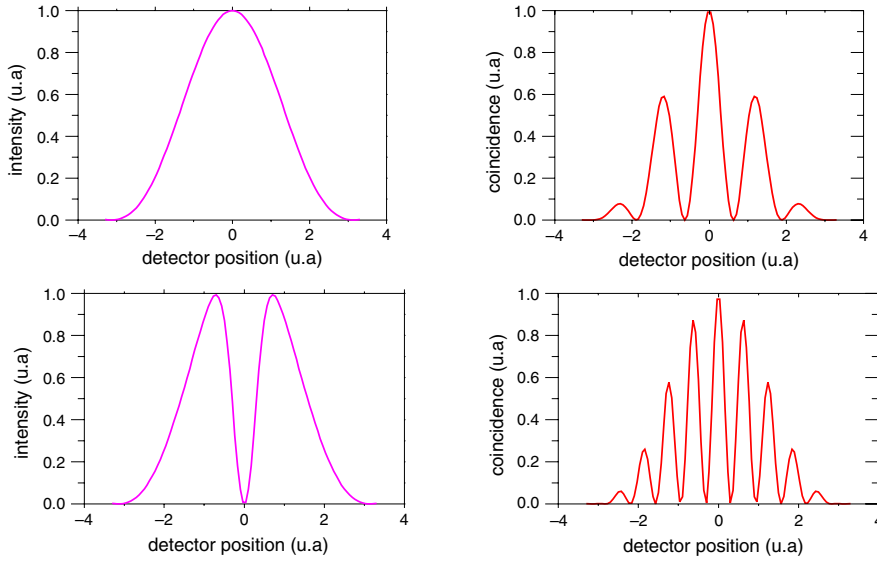


Fig. 13. Typical experimental results for two-photon interference at a double slit. The plots on the left show the profile of the pump beam at the double slit. The plots on the right show the two-photon interference pattern. In the lower pattern, the spatial frequency is doubled.

a 50/50 beam splitter and detected in coincidence. In order to control the spatial correlations between the pair of photons in the plane of the slits, the pump beam is sent through a wire and a lens, placed before the crystal. The angular spectrum of the pump is produced so that the image of the wire is projected onto the double slit plane. The pump beam is blocked after the crystal, and does not actually pass through the slits. However the image of the wire is transferred to the correlations between the twin photons, such that there is a relative spatial separation $2d$ between the photons. Therefore, if one photon passes through one of the slits, the probability of finding its twin in the other slit is practically zero. Then, almost all photon pairs that pass through the slits must have passed through the same slit. The detection of the coincidence distribution is performed by scanning both detectors together, in order to mimic a two photon detector. Again, we can use the two-photon state (73) and detection operator (76) for both the signal and idler fields to calculate the coincidence count distribution. We obtain [17]:

$$C(x) \propto |B_d(x)|^2 + 4|B_0(x)|^2 + |B_{-d}(x)|^2 + 4B_d(x)B_0(x) \cos\left(\frac{kd^2}{z_A} + \frac{kx2d^2}{z_1}\right) + 4B_0(x)B_{-d}(x) \cos\left(\frac{kd^2}{z_A} - \frac{kx2d^2}{z_1}\right) + 2B_d(x)B_{-d}(x) \cos\left(\frac{2kx2d^2}{z_1}\right), \quad (81)$$

where x is the position of the detectors, B_d , B_0 and B_{-d} are envelope functions which depend on the spatial amplitude distribution of the pump beam and the dimensions of the double slit aperture, z_A is the distance from the crystal to the double slit and z_1 is the distance from the slits to the detectors. In particular, B_j is proportional to the square root of the transverse profile of the pump beam at position $x = j$. We can see in Eq. (81) that two oscillating terms depend on kx and one term depends upon $2kx$, which is the two-photon interference term. Therefore, if $B_0(x) = 0$, then only the two-photon interference terms will survive. This condition is achieved through the preparation of the pump profile, using the wire and the lens to obtain a zero intensity profile at $x = 0$. Then the coincidence rate will be given by:

$$C(x) \propto |B_d(x)|^2 + |B_{-d}(x)|^2 + 2B_d(x)B_{-d}(x) \cos\left(\frac{2kx2d^2}{z_1}\right). \quad (82)$$

Fig. 13 shows a computer simulation of typical experimental results, similar to those obtained in Ref. [17]. The type of two-photon interference fringes depends strongly upon the transverse profile of the pump beam at the double slit aperture [52]. When the pump beam is a broad Gaussian distribution, the interference pattern depends only on the wavelength and not on the number of photons [59], and an interference pattern, shown in the upper right-side of Fig. 13, is obtained. However, if one manipulates the pump beam so that the photons always pass through the same slit, the spatial frequency of the interference pattern changes to twice the original frequency, as illustrated in Fig. 13(b). Additional experiments reporting the observation of the de Broglie wavelength of two or more photons have been reported [60–65]. The increase in spatial frequency in these experiments is equivalent to an increase in resolution, which may lead to interesting applications in optical lithography.

4.3.1. Quantum lithography

We can conclude from the experiment discussed in Section 4.3, that there are instances in which electromagnetic radiation with a given wavelength behaves as if it had a smaller wavelength, depending on the photon number. This idea has

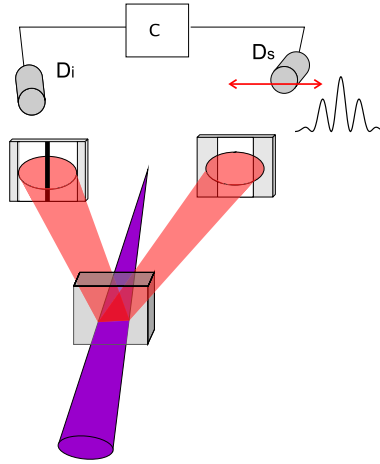


Fig. 14. Experimental set-up for the non-local double slit.

motivated the proposition of applications such as lithography processes with increased resolution. It was called *quantum lithography* [66–69] and is based on the possibility of creating two-photon wavepackets [17]. In brief, using entangled pairs of photons and coincidence techniques, it is possible to obtain two-photon wavepackets which interfere and diffract in the same fashion as light with twice its wavelength. In principle, this idea can be extended to N -photon wavepackets and in this case the increase in the resolution increases with N .

The term *quantum lithography* comes from the fact that the concept of photon is required to distinguish the behavior of one photon wavepackets and N photon wavepackets. However, there are propositions for the implementation of quantum lithography using classical light sources [70–74]. In this case it is the interaction between the light and some material which would only absorb N -photon wavepackets, and not J -photon wavepackets ($J \neq N$). Detection of only N -photon wavepackets projects the field onto the N -photon component.

Optical lithography is a process used to fabricate integrated circuits. It consists in the removal of a thin film from a substrate through the exposure to light. This results in drawings of very small circuits and electronic components. The future of integrated circuits in large scale depends on the possibility of reducing the size of these drawings. A limitation is given by the diffraction limit of the light used in the process, which depends upon the wavelength. Quantum lithography would allow one to obtain, for instance, the optical resolution of a UV beam, using near infra-red light. The main challenge towards quantum lithography seems to be finding proper materials which selectively absorb only N -photon wavepackets [75].

An experiment demonstrating this idea, similar to the one described in Section 4.3, was later reported in Ref. [69].

4.4. Non-local double slit

Another possibility in terms of variations of a double slit experiment using twin photons and coincidence detection is a non-local double slit [51], illustrated in Fig. 14. In this experiment double-slit interference is observed, even though neither photon passes through a double-slit aperture. The non-local double slit is built from a single slit placed in the signal beam and a thin wire placed in the idler beam. The combined effect of these two components results in double-slit type coincidence fringes. In order to calculate the coincidence count distribution, we can again use the two photon state given by Eq. (73) and the electric field operator given by Eq. (76), where the transfer function $\mathcal{T} = \mathcal{T}_1$ for the signal field corresponds to a single slit and the transfer function $\mathcal{T} = \mathcal{T}_2$ for the idler corresponds to a thin wire. In order to observe the coincidence fringes for the non local double slit, it is necessary to focus the pump beam on the z_A plane. This allows one to approximate the pump beam amplitude transverse distribution by a delta function. The resulting coincidence count distribution is given by [51]:

$$C(\rho_s, \rho_i) \propto \left| \int d\xi A_1(\xi) A_2(-\xi) \exp\left(ik \frac{\xi^2}{z_A}\right) \exp\left[ik \frac{\frac{1}{2}(\rho_1 - \rho_2) - \xi^2}{z_D - z_A}\right] \right|^2, \quad (83)$$

where A_1 and A_2 are the transmission functions of the single slit and the thin wire respectively, z_A is the longitudinal coordinate of the single slit and thin wire, considered to be at equal distances from the crystal ($z = 0$), and z_D is the position of the detection plane for both signal and idler detectors. The integral above is a Fresnel integral and the argument is given by the product of the functions A_1 and A_2 which results in the transmission function of a usual double slit aperture. Another characteristic which is present in this result, as well as many other SPDC experiments, is the dependence on the difference between the detector coordinates appearing in the Fresnel propagator in Eq. (83).

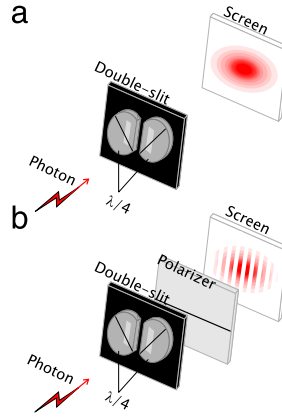


Fig. 15. The double slit quantum eraser for one photon. $\lambda/4$ represents a quarter wave plate.

4.5. The double-slit quantum eraser

A double slit experiment with twin photons can be used to implement a quantum eraser [76,77], which shows the complementarity between wave-like and particle-like behavior. Exploiting the polarization correlation between down-converted photons, the idler photon can be used to herald either interference fringes (wave-like) in the signal field or to determine which slit the signal photon passed through (particle-like). Furthermore, one can delay the decision about erasing this information or not.

Typically, if one cannot determine through which slit a photon passes, then interference fringes will be observed in the intensity distribution after the double slit aperture. However, if one can mark the photon's path, so that the two paths are in principle distinguishable, then no interference fringes appear. It was previously argued that the disappearance of interference fringes was due to the perturbation caused by the which-slit marker [78]. However, Scully, Englert and Walther showed that the interference fringes can reappear if one erases the which-slit information in the marker [77]. Hence the name *quantum erasure*. Let us begin by describing a simple double-slit quantum eraser with single photons. Let us suppose that a source emits single photons which propagate to a double slit. If interference fringes are visible on the detection screen after many photons have emitted, then one cannot determine through which slit each photon has passed. The state of the photons after the slits can be given by:

$$|\psi\rangle_{1\text{photon}} = \frac{1}{\sqrt{2}}[|\psi_1\rangle + |\psi_2\rangle], \quad (84)$$

where ψ_1 and ψ_2 represent the passage through slit 1 and 2 respectively. In order to mark the path of each photon, let us place quarter wave-plates in front of each slit, so that if the horizontally polarized photon crosses one of the slits, it leaves circularly polarized to the right and if it crosses the other it leaves circularly polarized to the left, as in Fig. 15(a). Then, a measurement of the photon polarization is enough to determine through which slit it has passed. This causes the interference pattern to disappear, even if the polarization is not measured. Even the possibility of obtaining which-path information is enough to destroy the interference, since the presence of the wave plates in each slit entangles states ψ_1 and ψ_2 with the polarization degree of freedom, so that the state becomes:

$$|\psi\rangle_{1\text{photon}} = \frac{1}{\sqrt{2}}[|R\rangle|\psi_1\rangle + |L\rangle|\psi_2\rangle], \quad (85)$$

where $|R\rangle$ and $|L\rangle$ are right and left circular polarization states respectively. The which-path information is available due to the entanglement between the state describing the passage through each slit and the output polarization state. It can be erased by projecting the two orthogonal polarization states $|R\rangle$ and $|L\rangle$ onto a—say—linear polarization state, $|H\rangle$ (horizontal) or $|V\rangle$ (vertical) for instance, as in Fig. 15(b). Therefore, after the polarizer, the which-path information is no longer available, and the interference fringes are recovered.

Using pairs of photons allows for a delayed choice quantum eraser, as reported in Refs. [53,54,79]. A sketch of an experiment is shown in Fig. 16. A pair of photons is prepared in a polarization-entangled state:

$$|\psi\rangle_{QE} = \frac{1}{\sqrt{2}}[|H\rangle_i|V\rangle_s + |V\rangle_i|H\rangle_s]. \quad (86)$$

The signal photon is sent through the double slit aperture and quarter-wave plates. The state of the photons after passage through the slits is given by:

$$|\psi\rangle_{QE} = \frac{1}{2}[|H\rangle_i(|L\rangle_s|\psi_1\rangle + |R\rangle_s|\psi_2\rangle) + i|V\rangle_i(|R\rangle_s|\psi_1\rangle + |L\rangle_s|\psi_2\rangle)]. \quad (87)$$

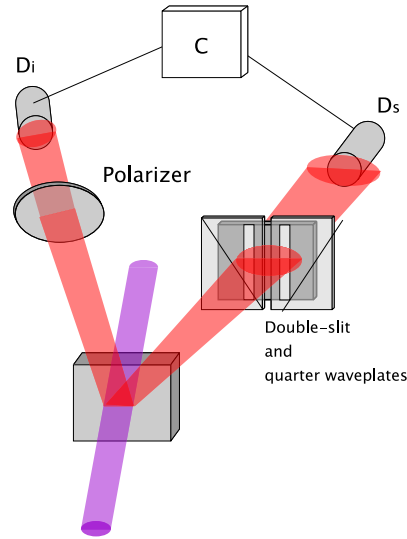


Fig. 16. The delayed choice double slit quantum eraser. Quarter wave-plates are used to mark the path of the signal photon. Which-path information can be recovered or erased by projecting the idler photon onto the appropriate polarization state.

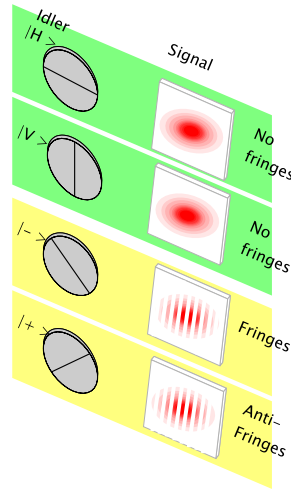


Fig. 17. The delayed choice double slit quantum eraser. Each polarization projection of the idler photon corresponds to a state preparation of the signal photon. Projections onto vertical and horizontal polarizations results in which-path information. Projections onto diagonal polarizations results in erasure of which-path information and interference.

The polarization entanglement allows the idler photon to be used as a which-path marker or eraser. If it is projected onto polarization H or V the signal photon will be projected onto state $|L\rangle_s|\psi_1\rangle + |R\rangle_s|\psi_2\rangle$ or $|R\rangle_s|\psi_1\rangle + |L\rangle_s|\psi_2\rangle$ respectively. Therefore, no interference is observed. However, if one projects the idler photon onto $|+\rangle$ ($+45$ degrees) or $|-\rangle$ (-45 degrees) linear polarizations, the which-path information is erased and the interference fringes return, as illustrated in Fig. 17. In order to see this, we write the state (87) in the $+/-$ basis:

$$|\psi\rangle_{QE} = \frac{1}{\sqrt{2}}[|+\rangle_i|+\rangle_s(|\psi_1\rangle - i|\psi_2\rangle) + |-\rangle_i|-\rangle_s(|\psi_1\rangle + i|\psi_2\rangle)]. \quad (88)$$

We see in Eq. (88) that projections of the idler photon onto $|+\rangle_i$ or $|-\rangle_i$ projects the signal photon onto a superposition of $|\psi_1\rangle$ and $|\psi_2\rangle$ states, which give interference fringes. This quantum eraser allows for “delayed choice”, meaning that the decision about the measurement of the idler photon can be delayed until the signal has already been detected.

5. Quantum imaging

In Sections 3.6 and 4.3 we discussed experiments in which the image or interference pattern of an object appears in the two-photon coincidence counts. These types of experiments have led to the idea of “quantum imaging”, which in some

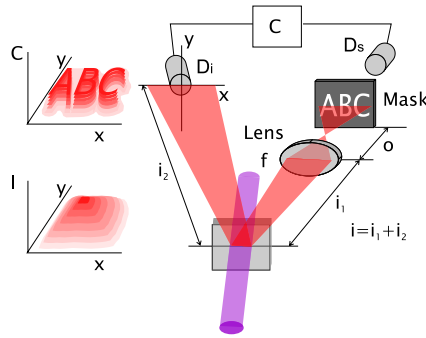


Fig. 18. Observation of a quantum image, similar to the experiment of Pittman et al. [15]. The image of the ABC mask appears in the coincidence counts when the detector D1 is scanned.

cases may present advantages over classical imaging techniques, such as increased spatial resolution [80–83], as discussed in Section 4.3. The term quantum images generally refers to images that appear in two-photon coincidence distributions. They are called *quantum*, because they were first produced with the quantum-correlated twin photons produced in parametric down-conversion. However, it is also possible to produce correlated images with classically correlated light sources. In this section we will discuss quantum and classically correlated images and some proposed applications.

5.1. Quantum images

The image of a double-slit aperture can be understood in terms of the diffraction theory of classical optics as the near-field distribution of the double slit, whereas the interference pattern is related to the far-field distribution. The amplitude distributions of the electric field in these two cases are related by a Fourier transform. This is also true for the correlated images and interference patterns which may appear in coincidence distributions. However, the propagation and detection of both signal and idler fields may influence the resulting spatial distribution.

In order to introduce the idea of a quantum image, let us consider the experiment reported by Pittman et al. [15] and illustrated in Fig. 18. Parametric down-conversion is produced as usual. An aperture mask is placed in the signal beam close to the detector and a lens also placed in the signal beam. Coincidence detection is performed such that the signal detector is a fixed large-aperture *bucket* detector, while the idler detector is scanned in the transverse plane. A 3-D plot of the coincidence counts as a function of the transverse coordinates x and y reproduces the image of the aperture ABC. See the inset in the upper part of Fig. 18. The lens in the signal beam is placed according to the advanced wave picture (see Section 4.2 for details). The imaging condition given by the thin lens formula $\frac{1}{f} = \frac{1}{i} + \frac{1}{o}$ is applied, where f is the focal length, o is the distance between the lens and the aperture mask (the image plane) and i is the distance between the lens and the crystal plus the distance between the crystal and the idler detector. According to the advanced wave picture, the crystal plays the role of a mirror in the imaging process.

There are some particular aspects which distinguish this image pattern from ordinary intensity images. One feature is that the image is observed in coincidence as a function of the position of the idler detector, even though the idler did not pass through the aperture mask. The image does not appear in the intensity distribution of the idler alone, but only when it is counted in coincidence with a detection of the signal photon. The intensity distribution depends only on the source shape as usual, as illustrated in the inset in the lower part of Fig. 18. Another aspect is that the dimensions and the resolution of the quantum image depend on the pump beam wavelength and spatial properties.

Initially, it was widely believed that the quantum correlation of the down-converted photons was necessary to observe quantum images [84]. Thus, it was quite surprising when similar types of correlated images were produced with classical sources. This is the subject of the next section.

5.2. Classical two-photon images

A great deal of discussion was triggered by the work of Bennink et al. [85,86], in which it was demonstrated that it is possible to obtain correlated images using classical light, in the same fashion as it is done with entangled photons. Bennink et al.'s experiment is sketched in Fig. 19. A laser pulse is sent to a mirror and then to a 50–50 beam splitter. The transmitted beam propagates through an aperture mask and is detected. Let us call this the signal beam. The idler beam is reflected at the beam splitter and sent directly to a CCD camera, which records the spatial intensity distribution. It is not necessary to use a pulsed laser, the pulse-like scheme can be obtained for instance with a chopper in a c.w. laser. However, it is important to have pulses, so that there will be a temporal correlation between signal and idler pulses.

The angle of the mirror before the beam splitter is randomly modulated in both axial and azimuthal directions. This artificially broadens the angular spectrum of the light sent to the beam splitter, and the temporal correlation results in an angular correlation between the signal and idler beams. The signal detector after the aperture mask is kept fixed, while

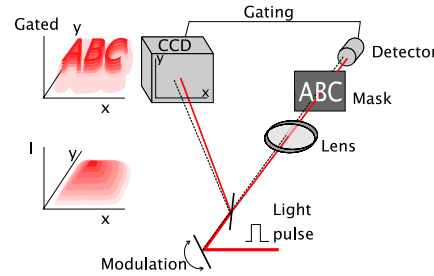


Fig. 19. Observation of a classically correlated image using a laser pulse as reported in Ref. [85].

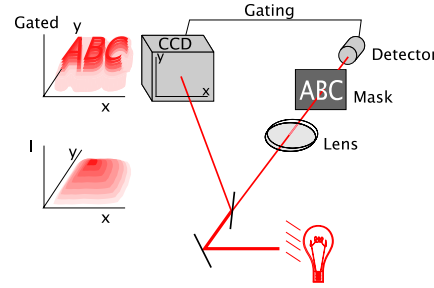


Fig. 20. Observation of a classically correlated image using a thermal light source.

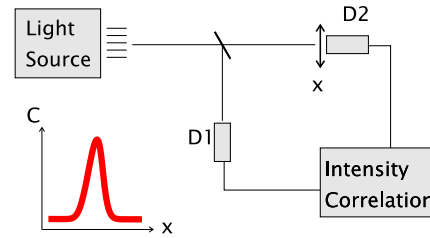


Fig. 21. Sketch of the Hanbury Brown and Twiss experiment. C is the intensity correlation. It is proportional to μ_{12} , the normalized spatial degree of coherence.

the idler is detected with the CCD camera which only records when a trigger pulse is sent by the signal. The triggered CCD image reproduces the *ABC* aperture, just as in the case of correlated photon pairs from SPDC. Almost all ingredients naturally present in the pair of photons produced in parametric down-conversion, are artificially introduced here: (i) temporal correlation and (ii) angular correlation. However, since the correlated pulses are produced classically, there is no entanglement. This experiment demonstrated that it is possible to obtain a correlated image using classical light, and opened up the discussion about the role of entanglement in quantum imaging experiments.

The production of correlated images with classical light was extended to thermal/chaotic light sources [70,87–90], supporting the idea that correlated images were not actually quantum. A typical experimental set-up for the observation of correlated images with thermal light is shown in Fig. 20 and is similar to Fig. 19. However, the pulsing to obtain temporal correlation and spatial modulation to obtain spatial correlation is not necessary anymore. Due to the natural bunching of photons in thermal light, it is possible to obtain temporal and spatial correlation directly from the thermal light. This kind of correlation was already observed in the famous experiment by Hanbury Brown and Twiss (HBT) [91]. In the HBT experiment, sketched in Fig. 21, the light is sent to a beam splitter and intensity correlations are measured. One detector is kept fixed, while the other is scanned along the detection plane. Results show that the width of the coincidence distribution is proportional to the spatial coherence of the input field. The larger the coincidence distribution, the smaller the spatial correlation and the larger the spatial coherence. For incoherent sources like thermal sources, the spatial coherence depends only on the source dimensions, as discussed in Section 3.1.2. In this way the HBT interferometer was used to measure the diameter of stars. Correlated imaging with a laser source required a modulation to induce spatial correlations since the spatial correlation is inversely proportional to the spatial coherence, which in the case of a laser source can be quite large.

While classical light can also be used to produce correlated images, there is a price to be paid: the signal to noise ratio is generally higher than for the output state of a down-converter [87,92]. Quantum imaging has been analyzed in the general case of light fields with Gaussian photon statistics [93,94], and this formalism has been applied to two-photon imaging [95].

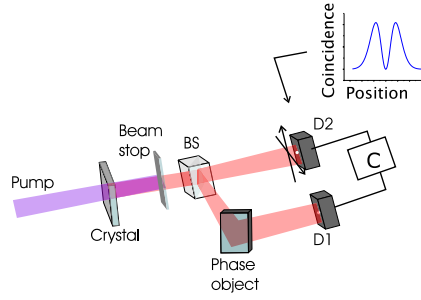


Fig. 22. Observation of a quantum image with a pure phase object.

5.3. Phase objects

The discussion about the differences between quantum and classically correlated images has led to an important test, proposed and realized experimentally by Abouraddy et al. [96]. The authors observed correlated images using phase objects. Fig. 22 shows a sketch of a typical experimental set-up. The transmission configuration using an aperture is replaced by a reflection configuration using a micro electromechanical system (MEMS) micro-mirror. The spatial amplitude distribution of the reflected beam is not changed, while the spatial phase distribution is modulated. The signal photon propagates through this plate and is detected afterwards by a fixed detector D1, outfitted with a small pinhole. The idler photon propagates directly to detector D2, which is scanned in the transverse plane. The spatial coincidence distribution will be determined by the diffraction pattern of the signal beam. A typical coincidence profile is illustrated in the inset of Fig. 22. This kind of two peak profile, is obtained when a double-slit object with phase π separated by a line of phase 0 is prepared in the MEMS. It was shown in Ref. [97], that coherent imaging can also be achieved with pseudo-thermal sources. The observation of quantum images of phase objects is a further demonstration of the differences between the correlated images with classical and quantum light.

5.4. Spatial resolution of magnified images: quantum versus classical

It is well known that the spatial resolution of an image increases when the wavelength of light used for illuminating the object is decreased. On the other hand, short wavelengths in the UV range or smaller usually damage an illuminated object. Needless to say, it would be advantageous to achieve the spatial resolution of short wavelengths while illuminating the object with a light beam with longer wavelength. Spatially entangled two-photon light beams generated by SPDC are good candidates for this special light source because it has two wavelengths associated with the two-photon beams: the central wavelengths of the individual photons λ and the de Broglie wavelength associated with the biphoton wavepacket equal to $\lambda/2$, as discussed in Section 4.3. It was demonstrated experimentally in Ref. [81] that magnified images of objects illuminated by two-photon wavepackets, as in a microscope [98], can be generated with spatial resolution better than the diffraction limit and are self-apodized [99].

For a comparison with a classical imaging experiment suppose an object is illuminated by a classical coherent light source. The image is produced with a lens with a focal length f , separated from the object by a distance z_L . The image plane is located at a distance z_D far from the lens. If it is assumed that the light arriving at the object is a plane wave, the electric field at the image plane is

$$E(\boldsymbol{\rho}) = \int O(\boldsymbol{\xi}) T_L \left(\frac{k\boldsymbol{\xi}}{z_L} + \frac{k\boldsymbol{\rho}}{z_D} \right) d\boldsymbol{\xi}, \quad (89)$$

where $O(\boldsymbol{\xi})$ is the transmission function of the object, $\boldsymbol{\rho}$ is the transverse position in the image plane, $k = 2\pi/\lambda$ is the wave vector of the incident plane wave and T_L is the Fourier transform of the magnitude of the lens transmission function. This last term limits the spatial resolution of the image due to the finite size of the lens aperture [99].

In the imaging experiment with photon pairs generated by SPDC, the object information appears in the two-photon probability amplitude at the image plane. It was shown theoretically in Ref. [80] that the probability amplitude of simultaneously detecting two down-converted photons in the image plane of an object illuminated by the signal photon is

$$\Psi(\boldsymbol{\rho}) = \int O(\boldsymbol{\xi}) T_F \left(\frac{2k\boldsymbol{\xi}}{z_L} + \frac{2k\boldsymbol{\rho}}{z_D} \right) d\boldsymbol{\xi}, \quad (90)$$

where it is assumed that $z_L = z_{Li} = z_{Ls}$, $z_D = z_{Di} = z_{Ds}$. Vector $\boldsymbol{\rho}$ describes the detection position at both signal and idler detection planes, so that $\boldsymbol{\rho}_i = -\boldsymbol{\rho}_s = \boldsymbol{\rho}$. This last assumption means that the image is measured by displacing the signal and idler detectors simultaneously in opposite directions. It has also been assumed that the pump laser beam at the object plane

has a transverse profile which is sufficiently narrow to be described by a Dirac delta function. T_F is the Fourier transform of the function F defined as

$$F(\mathbf{v}) = \int |A_{Li}(\mathbf{u} + \mathbf{v})| |A_{Ls}(\mathbf{u} - \mathbf{v})| d\mathbf{u}, \quad (91)$$

where $|A_{Ls}|$ and $|A_{Li}|$ are the magnitude of the aperture functions of the lenses placed in signal and idler paths, respectively. $F(\mathbf{v})$ is the correlation of the lens transmission function magnitudes [80]. In comparing Eqs. (89) and (90), one notices the presence of the factor $2k$ in Eq. (90) instead of k as in Eq. (89). Eq. (90) is equivalent to an image generated by single photons, however with wavelength equal to the De Broglie wavelength [58,17] of the biphoton $\lambda/2$, and thus shows improvement in the spatial resolution. On the other hand, the function F present in Eq. (90) describes an effective lens with aperture transmission function that has a magnitude that is equal to the correlation of the magnitudes of the aperture transmission functions of the actual lenses, as it can be seen in Eq. (91). The function F describes an effective apodized lens [99].

The image generated by the parametric down-converted photons is better resolved than a similar one generated by an infrared classical light source with the same wavelength, and is resolved better than the diffraction limit in this case. In spite of this, the quantum image resolution is not as good as the resolution of the image produced by the pump laser source ($\lambda_p = \lambda/2$), since the transmission function of the effective lens seen by the photon pairs is not equal to the transmission function of the original lenses. Apodization effects are also observed in the twin photon image without physically apodizing the lenses used, which could lead to interesting applications.

The spatial resolution of images obtained in quantum fourth-order imaging has also been compared with that obtained in a classical second-order incoherent imaging method [82]. The intensity at the image plane of an object illuminated by a classical incoherent light source is [36]:

$$I(\boldsymbol{\rho}) = \int |O(\boldsymbol{\xi})|^2 T_{\wp} \left(\frac{2k\boldsymbol{\xi}}{z_L} + \frac{2k\boldsymbol{\rho}}{z_D} \right) d\boldsymbol{\xi}, \quad (92)$$

where T_{\wp} is the Fourier transform of the function \wp , defined as

$$\wp(\mathbf{u}) = \int A_L(\mathbf{u} + \mathbf{v}) A_L(\mathbf{u} - \mathbf{v}) d\mathbf{v}, \quad (93)$$

$k = 2\pi/\lambda$, in which λ is the central wavelength of the incoherent light beam and A_L is the aperture transmission function of the lens. The function $\wp(\mathbf{u})$ is the auto-correlation function of the aperture function of the lens used for imaging, and describes the aperture function of an effective lens. Note that in the two-photon image the effective lens transmission function (91) is not an auto-correlation function but a cross correlation function of the signal and idler aperture lens transmission functions. Another difference with respect to the object function is that in the incoherent imaging only the square modulus of the object function appears in the optical intensity expression, i.e., this method is not sensible to the object phase. In quantum imaging the complete object function is present in the coincidence distribution at the image plane, i.e., the image carries the information about the object spatial phase. A situation where the object function has no phase variation was analyzed in Ref. [82], but the two imaging methods still produced completely different results. The transmission function of the lens pair in the two-photon imaging was modified such that the cross-correlation function between them was different from the auto-correlation of one of the lenses. When the object was illuminated by an incoherent classical light source, the image was not resolved spatially. On the other hand, an image with very high spatial resolution was measured when the object was illuminated by one down-converted photon, and both photons were detected in coincidence at the image plane.

6. Spatial correlations: quantum versus classical

In the 1990's, many novel and interesting features of spatial correlations were observed experimentally and well described by the quantum theory. Many of these results suggested that the spatial correlations were indeed quantum correlations, even though the non-existence of a classical analog was not discussed in most of these contributions. For example, the non-local conditionality of two-photon interference fringes [14,60] was well described by quantum mechanics. However, there was never any formal proof that the conditional interference fringes could not be exactly reproduced by some special classical light source. In Ref. [9], it was shown that the simple detection of coincidence counts above the accidental coincidence rate is a proof of non-classical behavior. However, this refers to the temporal correlations and cannot be directly extended to spatial variables.

Perhaps the first experimental demonstration of the quantum nature of light via a fourth-order correlation function was photon anti-bunching, first observed in the time domain by Kimble et al. in 1977 [100]. Demonstration of the non-classical nature of photon anti-bunching was based on the violation of a classical inequality. In the same spirit, the anti-bunching of photons was later demonstrated in the transverse spatial domain in Ref. [18], and was probably the first formal demonstration of the non-classical behavior of spatial correlations. In 2004, Howell et al. [21] and D'Angelo et al. [22] demonstrated that the pairs of down-converted photons are indeed entangled by experimentally violating classical separability criteria.

In this section we review several of these important results concerning the non-classical nature of transverse correlations. The observation, detection and quantification of spatial entanglement will be discussed in Sections 7 and 8.

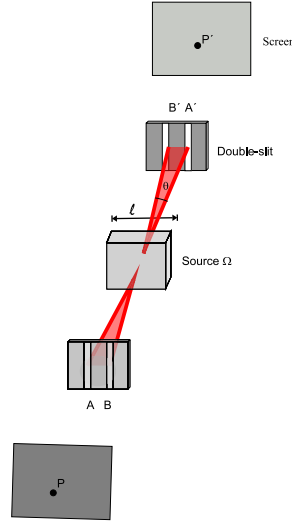


Fig. 23. Double-slit interference with two photons.

6.1. Conditional interference and complementarity in one and two-particle interference patterns

An interesting idealized two-particle double-slit interference experiment was discussed by Greenberger et al. [101] in 1993. In this gedanken experiment, two identical double-slits were placed in opposite sides of a linear source Ω with extension l that always emits two particles with momenta approximately equal and opposite, as sketched in Fig. 23. The angle between the slits and the source is θ and, due to the momentum correlation, the particles pass either through the slits A and A' or B and B' . The arrival of the particles is registered at two opposite screens after each double-slit. For the case where the daughter particles are photons and $l \gg \lambda/\theta$, the probability amplitude for one of the particles to arrive at P and the other to arrive at P' is [101]

$$\Psi_2(x_s, x_i) \propto \cos[k\theta'(x_i - x_s)] \quad (94)$$

where x_s and x_i are the transverse coordinates, $k = 2\pi/\lambda$, λ is the wavelength (de Broglie or optical) related to the emitted particles, and θ' is the angle that is subtended by the hole pairs and the detecting screens. On the other hand, if $l \ll \lambda/\theta$, the probability amplitude is

$$\Psi_2(x_s, x_i) \propto \cos(k\theta' x_i) \times \cos(k\theta' x_s). \quad (95)$$

Expression (94) shows that the coincidence interference pattern detected when $l \gg \lambda/\theta$ presents “conditional fringes”. If the interference pattern is recorded by two movable detectors D_i and D_s , the term “Conditionality” means that the position of the interference fringes will vary depending on the position of both detectors. Suppose the interference pattern is recorded by keeping one of the detectors (D_i , for example) fixed at some position x while D_s is scanned. For two different positions x , two displaced interference patterns will be recorded. Expression (95) shows that for $l \ll \lambda/\theta$ a product of independent single-particle interference patterns (“independent fringes”) is measured and conditional fringes are not detected. This condition is the requirement to detect the usual Young single-particle interference pattern.

This idealized experiment was tested experimentally in Ref. [52] using photons obtained from SPDC. The experiment is illustrated in Fig. 24. Two-photon interference experiments with spatial interference patterns were also observed in [7, 102, 14, 56, 103, 17] but as discussed above [101] the detection of a fourth-order interference pattern does not guarantee the presence of conditional fringes. Using the quantum multimode theory presented in Section 2 to calculate the fourth-order correlation function as a function of the detector positions, the number of coincident photons at positions x_i and x_s is [52]:

$$\begin{aligned} N_c(x_i, x_s) \propto & A(x_i, x_s) + 2 B_1(x_i, x_s) B_2(x_i, x_s) \cos\left(\frac{k d^2}{z_A} + \frac{k x_i 2 d}{z_1}\right) + 2 B_1(x_i, x_s) B_3(x_i, x_s) \cos\left(\frac{k d^2}{z_A} + \frac{k x_s 2 d}{z_1}\right) \\ & + 2 B_2(x_i, x_s) B_4(x_i, x_s) \cos\left(\frac{k d^2}{z_A} - \frac{k x_s 2 d}{z_1}\right) + 2 B_3(x_i, x_s) B_4(x_i, x_s) \cos\left(\frac{k d^2}{z_A} - \frac{k x_i 2 d}{z_1}\right) \\ & + 2 B_2(x_i, x_s) B_3(x_i, x_s) \cos\left[\frac{2 d k (x_i - x_s)}{z_1}\right] + 2 B_1(x_i, x_s) B_4(x_i, x_s) \cos\left[\frac{2 d k (x_i + x_s)}{z_1}\right] \end{aligned} \quad (96)$$

with

$$A(x_i, x_s) = |B_1(x_i, x_s)|^2 + |B_2(x_i, x_s)|^2 + |B_3(x_i, x_s)|^2 + |B_4(x_i, x_s)|^2. \quad (97)$$

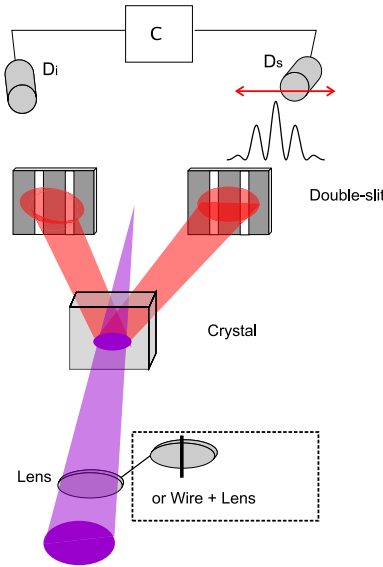


Fig. 24. Double-slit interference with two photons and parametric down-conversion. Focusing the pump beam with a lens induces an anti-correlation (dependence on the sum of coordinates) and using a lens plus a wire induces correlation (dependence on the difference of coordinates).

Here $2d$ is the separation of the double-slits, $2a$ is the width of each slit. The first four cross terms in (97) give independent fringes that depend only on x_s or x_i , while the last two terms give conditional fringes which depend upon $x_s \pm x_i$. The interesting fact that appears from this calculation is that the diffraction terms $B_j(x_i, x_s)$, $j = 1, 2, 3, 4$, are proportional to the transverse profile of the pump laser at different transverse positions in the plane of the double slit aperture: $B_j(x_i, x_s) \propto \mathcal{W}(0, z_A)$ with $j = 2, 3$, $B_1(x_i, x_s) \propto \mathcal{W}(d, z_A)$ and $B_4(x_i, x_s) \propto \mathcal{W}(-d, z_A)$. Generating the photon pairs using pump beams with different transverse profiles at the double-slit plane, the authors in Ref. [52] were able to measure two-particle independent fringes, as well as conditional fringes that depend on the difference or the sum of the detector position coordinates. Conditional fringes which depend on the sum of the position coordinates have been predicted theoretically in Refs. [104,105].

Greenberger et al. [101], analyzing the two extreme cases discussed above (independent versus conditional fringes) affirmed: "... there is a sort of complementarity between one- and two-particle fringes: the condition for seeing one precludes the possibility of seeing the other". When the source dimension or the distance from the double-slits to the source is such that the idealized experiment is analyzed in an intermediate geometry when compared with the extreme cases mentioned above, both single-particle fringes and conditional two-particle fringes are present [106,101,105,107]. Horne [105] derived a complementarity relation for the one- (v_1) and the two-particle (v_{12}) fringe visibility for a general state of a two-particle system [108]:

$$v_1^2 + v_{12}^2 = 1. \quad (98)$$

The single-particle fringe visibility is derived from the normalized single-particle probability density, which is obtained by integrating the joint probability density with respect to the position of one of the particles. The two-particle visibility is obtained from the two-particle "corrected" probability density [109,108]. This definition prevents the visibility v_{12} from being unity when particles 1 and 2 are prepared in a product state. Abouraddy and collaborators [110,111] studied the two-particle double-slit interferometer for the case where the particles are generated by means of SPDC. Photon pairs generated collinearly by the crystal are passed through a double-slit aperture and are imaged by a $2f$ lens system at the coincidence detector camera. For this geometry, the authors verified the above complementarity relation experimentally [110]. Calculation of v_1 and v_{12} from the measured data follows the strategy used by Horne [105]. The single-photon coincidence probability associated with the two-photon pair transmitted by the double-slit is calculated by integrating the fourth-order correlation functions with respect to one of the position variables.

6.2. Spatial antibunching

The experimental observation of the spatial anti-bunching of photons consists in the production of a homogeneous optical field for which it is more probable to detect coincident photons at spatially-separated positions in the transverse plane. The original idea of anti-bunching of photons [100] was connected to the time interval between the emission of two photons by a light source. Spatial anti-bunching means that the probability of finding two photons together at the same position in the transverse propagation plane is smaller than the probability of finding them at different positions. For a classical light

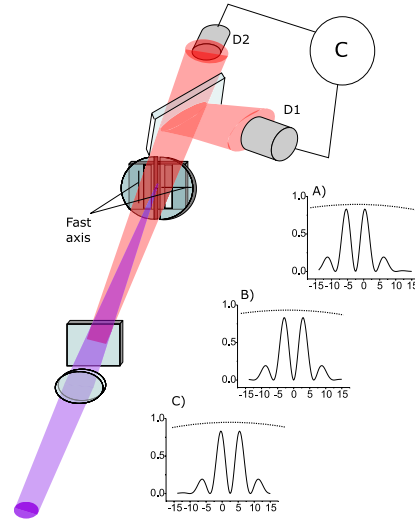


Fig. 25. Experiment for the observation of the spatial anti-bunching. The vertical axes in the plots are normalized coincidence rates for the solid lines and single count rates for the dashed lines. The horizontal axes are D2 detector positions in arbitrary units. The position of detector D1 is fixed in (a) -2.5 , (b) 0 and (c) $+2.5$ and D2 is scanned.

beam, the best that one can do is to have equal probability of detecting photons together or apart. A thermal source produces light that is bunched in time and in space, while an ideal laser produces light which is neither bunched nor anti-bunched. It is also important to note that both bunching and anti-bunching require that the fields be stationary (depend only on $\tau = t_1 - t_2$) and homogenous (depend only on $\delta = \rho_1 - \rho_2$). If this were not the case, it would be possible to simulate temporal anti-bunching using a low intensity pulsed laser, for instance.

From a mathematical point of view, the inequality

$$\Gamma^{(2,2)}(\delta, \tau) \leq \Gamma^{(2,2)}(0, 0), \quad (99)$$

must be satisfied by any classical field. $\Gamma^{(2,2)}$ is the fourth-order coherence function, which is proportional to the coincidence count probability. The violation of this inequality implies anti-bunching if the condition of stationarity and homogeneity is fulfilled. This means that the temporal and spatial arguments of all coherence functions ($t, t + \tau, \rho, \rho + \delta$) can be replaced by (τ, δ). The experiment performed in Ref. [18] is sketched in Fig. 25. The non-linear crystal is pumped by a Gaussian profile laser beam and collinear type II down-conversion is produced. Signal and idler photons are sent to a double-slit aperture equipped with quarter wave-plates (see below). After propagation through the slits, the photons are sent to a 50/50 beam splitter (BS) and single-photon detectors are placed in each output port. The detectors are carefully calibrated, so that the transverse coordinates in both detection planes are equivalent. This arrangement is essentially a two-photon detector. Detector D1 is kept fixed while D2 is scanned in the transverse plane. For an ordinary double-slit, the resulting coincidence pattern would display the usual interference fringes, equivalent to the intensity fringes in a double-slit experiment. To produce a spatially anti-bunched field, a phase shift of π is produced in the coincidence fringes, so that the interference maxima are now minima and vice versa. In this case, the probability of finding two photons together in the same point ($\delta = 0$) is smaller than the probability of finding them apart. This is the signature of spatial anti-bunching of photons, provided the condition of homogeneity is fulfilled.

The π phase shift is obtained using a double-slit aperture with a zero-order quarter-wave plate placed in front of each slit. The fast axis of one wave plate is oriented along the vertical direction and the fast axis of the other is oriented along the horizontal direction. The pump beam is focused in the plane of the slits, which causes an anti-correlation in the positions of the photons in this plane [16], so that if one photon crosses one slit, its twin will pass through the other slit. The type-II SPDC produces photons in the polarization state $|H\rangle \otimes |V\rangle$. The position anti-correlation at the plane of the double-slit guarantees that the photons pass through different slits, resulting in the state

$$|\Psi\rangle_{AB} = \frac{1}{\sqrt{2}}(|\psi_1, H\rangle|\psi_2, V\rangle + e^{i\pi/2}|\psi_2, H\rangle e^{i\pi/2}|\psi_1, V\rangle), \quad (100)$$

where ψ_1 and ψ_2 are the quantum states describing the spatial variables when the photons pass through slit 1 or slit 2, respectively. The $\pi/2$ phase factors are due to the delay introduced by the zero-order quarter-wave plates. The coincidence probability is [18,19]

$$C(x_s, x_i) \propto 1 - \cos\left[\frac{kd}{z}(x_1 - x_2)\right], \quad (101)$$

where k is the wave number of the down-converted fields, d is the separation between the slits, z is the propagation distance, and x_1 and x_2 are the positions of detectors D1 and D2. The coincidence probability is zero when $x_1 = x_2$, corresponding to a spatially anti-bunched field. Typical coincidence and intensity measurements observed in Ref. [18] are shown in the insets of Fig. 25. The coincidence distribution is near zero when both detectors observe the same point, and the single-photon intensity is nearly constant for all positions. The coincidence distributions violate inequality (99), as $\Gamma^{(2,2)}(\delta) > \Gamma^{(2,2)}(0)$, for many values of δ . The measurements are performed for several positions in the transverse planes of both detectors, demonstrating homogeneity. It was also demonstrated that the same effect can be observed without the use of a double-slit, with free propagating signal and idler beams [112]. Spatial anti-bunching has also been produced using Hong–Ou–Mandel interference of photons in an anti-symmetric polarization state [113]. This arrangement allows for the production of a beam of photons in a “singlet” polarization state.

7. Spatial entanglement

Quantum entanglement is a correlation that can exist between two or more quantum systems. In the case of pure states, entanglement implies that the quantum state $|\Psi\rangle_{12}$ describing the—say—two systems cannot be separated into a product of quantum states $|\psi\rangle_1 \otimes |\phi\rangle_2$. If the bipartite state can be written in this form it is said to be separable. In the more general case of mixed states, a separable bipartite state can be written as a convex sum of tensor products of local density matrices [114,115]:

$$\hat{\rho}_{\text{sep}} = \sum_i p_i \hat{\rho}_{1i} \otimes \hat{\rho}_{2i}, \quad (102)$$

where $\sum_i p_i = 1$ and $p_i \geq 0$. If a bipartite quantum state cannot be written in the form (102), it is entangled. For a more in depth discussion of quantum entanglement in general, we refer the reader to two recent review articles [114,115].

As discussed in Sections 4–6, although many experiments performed in the 1990's strongly suggested that photon pairs produced by SPDC were indeed entangled in the spatial degrees of freedom, it wasn't until 2004 that experimental tests confirmed this fact [21,22]. These experiments made use of entanglement criteria involving measurements of the sum and difference of the position and momentum variables [116,117], or EPR criteria involving conditional measurements [118,119].

7.1. Continuous variable entanglement criteria

There has been much work concerning the detection and characterization of entanglement in continuous variable degrees of freedom. An overview of the continuous variable formalism, and entanglement criteria for continuous variables, can be found in a number of review articles [120,121]. Though the physical system of interest is usually the field quadratures of intense fields, continuous variable entanglement conditions are also applicable to spatial entanglement of photon pairs.

For the spatial degrees of freedom of photon pairs, it is most useful to consider the global operators

$$\mathbf{X}_{\pm} = \mathbf{x}_1 \pm \mathbf{x}_2, \quad (103a)$$

$$\mathbf{P}_{\pm} = \mathbf{p}_1 \pm \mathbf{p}_2, \quad (103b)$$

where in the present case \mathbf{x} and \mathbf{p} are the position and momentum operators for photons 1 and 2, and we assume that $[\mathbf{x}_j, \mathbf{p}_k] = i\delta_{j,k}$ and $j, k = 1, 2$. In the case of spatially entangled photons, the position and momentum observables correspond to measurements in the near and in the far-field respectively, relative to the source plane, namely the SPDC crystal. The near field is associated with a position measurement at the source plane, while the far field is associated with a momentum measurement at the source plane.

In most cases, entanglement can be identified through violation of one of a number of inequalities, which thus serve as entanglement witnesses. For instance, the Mancini–Giovannetti–Vitali–Tombesi (MGVT) criteria [117] reads

$$\langle \Delta^2 \mathbf{X}_{\pm} \rangle \langle \Delta^2 \mathbf{P}_{\mp} \rangle \geq 1, \quad (104)$$

where Δ^2 stands for the variance, while the separability criteria of Duan, Giedke, Cirac and Zoller (DGCZ) [116] is

$$a^2 \langle \Delta^2 \mathbf{X}_{\pm} \rangle + \frac{1}{a^2} \langle \Delta^2 \mathbf{P}_{\mp} \rangle \geq 2, \quad (105)$$

where a is a local scaling parameter which guarantees that the quantities in the sum are dimensionless. One can optimize condition (105) over a , in which case one arrives at condition (104) [122]. All separable states of the form (102) will obey inequalities (104) and (105), and thus violation of either of them is a sufficient condition for identifying quantum entanglement. Inequalities (104), (105) are examples of a more general class of entanglement witnesses involving second-order moments [123], for which Hyllus and Eisert have provided an optimization procedure [122].

The Simon criterion [124] is a necessary and sufficient condition for $1 \times N$ mode Gaussian states [125]. To evaluate this criterion, it is necessary to reconstruct the covariance matrix [120,121]. Violation of the Simon, MGVT or DGCZ criteria are sufficient for identifying quantum states with negative partial transpose (NPT) [126–128]. In the general case, violation of

these criteria is not a necessary condition for entanglement even in the case of Gaussian states, due to the existence of bound entangled states which have a positive partial transpose.

For non-Gaussian states, these second-order criteria are sufficient, but not necessary, and there exist NPT entangled states which do not violate any second-order criteria. In this case one can use the NPT criteria of Shchukin and Vogel, which provides a hierarchy of inequalities involving combinations of second and higher-order moments [129]. In fact, they have shown that inequalities (104), (105) and the Simon criterion are special cases of this general NPT criteria. Violation of any inequality in the Shchukin–Vogel hierarchy indicates that the quantum state is NPT, and is thus a sufficient condition for entanglement. Higher-order inequalities obtained from the Shchukin–Vogel criterion have been violated recently for a spatially non-Gaussian two-photon state which does not violate any second-order criteria [130]. We note that there exist several other CV entanglement criteria involving higher order moments [131–141].

7.2. Correlations in the near and far field

The CV entanglement criteria discussed in Section 7.1 can be easily applied to the spatial correlations of SPDC photon pairs. In this case, the position variable x corresponds to the transverse position ρ and the momentum variable p is related to the transverse wave vector via $p = \hbar q$. The position and wave vector distributions can be observed through intensity measurements in the near and far field of the non-linear crystal, respectively. Using simple optical systems composed of lenses and free space, it is possible to measure the spatial distributions of the down-converted photons in the near and far field. In the near field, one generally observes a strong correlation between the positions of the signal and idler photons. An intuitive way to understand this correlation is through the fact that the two down-converted photons are “born” from the same pump photon simultaneously. Thus, the photons are produced at approximately the same transverse position inside the crystal. If the crystal were infinitesimally thin in the longitudinal direction, this would produce a point-like correlation between their positions in the crystal plane.

The field operator which describes detection in the near-field is given by

$$\mathbf{E}_{\text{nf}}(\rho) \propto \int d\mathbf{p} \mathbf{a}(\mathbf{q}) e^{-i\mathbf{q}\rho}. \quad (106)$$

Assuming that the quantum state of SPDC photon pairs is given by Eq. (59), the near-field correlations are governed by the profile of the pump beam $\mathcal{W}(\rho)$ and the Fourier transform of the phase matching function: $\Gamma(\rho) = \mathcal{F}\{\gamma(\mathbf{q})\}$. Typically, $\Gamma(\rho)$ is much narrower than $\mathcal{W}(\rho)$ at the crystal face. The detection amplitude is defined as $\Psi_{\text{nf}}(\rho_s, \rho_i) = \langle 0 | \mathbf{E}^+(\rho_i) \mathbf{E}^+(\rho_s) | \Psi \rangle$ and its square modulus is proportional to the coincidence rate.

If $\mathcal{W}(\rho)$ is approximately constant in the region where $\Gamma(\rho)$ varies appreciably, then the near-field detection amplitude is given by

$$\Psi_{\text{nf}}(\rho_s, \rho_i) \propto \Gamma(\rho_s - \rho_i). \quad (107)$$

$\Gamma(\rho)$ is generally a narrow function peaked at $\rho = 0$, which guarantees that the positions of the down-converted photons are correlated: $\rho_i = \rho_s$. We note that this is a much simplified picture of near-field correlations. It has very recently been shown that the near-field distribution of the biphoton may present a complex structure due to fourth-order interference of photon pairs that originate from different transverse planes of the crystal, and is strongly dependent upon the collinear phase mismatch [142,143].

In the far-field region, the down-converted photons exhibit anti-correlation. This is understood intuitively via momentum conservation in the SPDC process. If the pump beam is centered around $\mathbf{q} = 0$, momentum conservation guarantees that the down-converted photons are produced such that $\mathbf{q}_s \approx -\mathbf{q}_i$. Since the transverse position in the far-field is associated with the momentum distribution at the crystal, this translates into anti-correlation in the detection positions in the far-field. Equivalently, if $\mathcal{W}(\rho)$ is much larger than $\Gamma(\rho)$, then this implies that for the Fourier transforms of these functions the inverse is true: $v(\mathbf{q})$ is much narrower than $\gamma(\mathbf{q})$. The field operator corresponding to detection in the far-field as

$$\mathbf{E}_{\text{ff}}(\rho) \propto \mathbf{a}\left(\frac{\rho}{b}\right), \quad (108)$$

so that the detection amplitude can be approximated by

$$\Psi_{\text{ff}}(\rho_s, \rho_i) \propto v\left(\frac{\rho_s}{b_s} + \frac{\rho_i}{b_i}\right), \quad (109)$$

where b_s and b_i are scaling factors with dimension of length⁻², as the argument of the function v has units of a transverse wave vector (spatial frequency). Eq. (109) shows that position measurements in the far-field are associated with the momentum profile $v(\mathbf{q})$ in the near-field. Thus, through position measurements in the near and far-field, one can test the entanglement criteria (104) or (105). For example, in this case the MGV criterion (104) gives

$$\langle \Delta^2 \mathbf{X}_- \rangle \langle \Delta^2 \mathbf{P}_+ \rangle = \Delta^2 v \Delta^2 \Gamma \geq 1, \quad (110)$$

where $\Delta^2 v$ and $\Delta^2 \Gamma$ are the variances of the functions v and Γ , respectively. For a Gaussian pump beam with width w at the crystal face, $\Delta^2 v = 1/w^2$, and $\Delta^2 \Gamma \approx \lambda_p L / (2\pi)$ [144], where L is the crystal length and λ_p is the wavelength of the

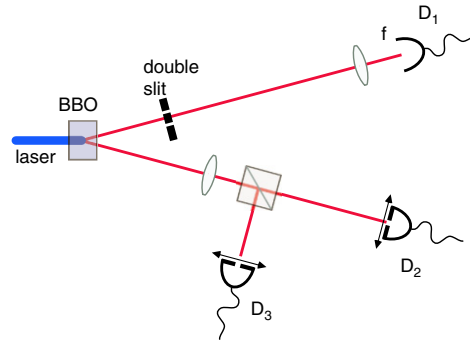


Fig. 26. Experimental setup for test of spatial entanglement performed by D'angelo et al. [22]. Measurements in the near field are performed by scanning detector D_2 in the image plane of an imaging lens system. Far-field measurements are realized by scanning detector D_3 in the Fourier plane of the lens. Detector D_1 is a bucket detector, placed in the focal plane of a lens.

pump beam. Since v and Γ are independent functions, they need not respect the limit on the right-hand side. In fact, for a $\lambda = 400$ nm Gaussian pump beam with width $w = 1$ mm, and $L = 1$ mm crystal, the left-hand side is on the order of 10^{-4} .

The strong spatial correlation depends explicitly on the widths of the pump beam and phase matching function. For long crystals and strongly focused pump beams, this correlation can be decreased so that the two-photon state is almost separable [145,146]. In this regime the shape and form of the pump beam and phase matching function become very important. In the approximation where both functions are described by Gaussians, the two-photon state is separable when $\Delta^2 v = \Delta^2 \Gamma$.

A condition similar to inequalities (104) and (105) was tested by D'Angelo et al. for down-converted photons using a ghost imaging setup [22], as illustrated in Fig. 26. Here a double slit was placed in the path of the signal photon, which is detected by a stationary “bucket” detector. The idler photon is detected by scanning a point-like detector in either the near-field or far-field, resulting in a ghost imaging or ghost interference scenario. The non-classicality conditions tested were

$$\begin{aligned} \Delta^2(x_1 - x_2) &< \min(\Delta^2 x_1, \Delta^2 x_2); \\ \Delta^2(p_1 + p_2) &< \min(\Delta^2 p_1, \Delta^2 p_2). \end{aligned} \quad (111)$$

Violation of both inequalities by the same quantum state implies entanglement. In the experiment, $\Delta^2(p_1 + p_2)$ was evaluated through the visibility of the ghost interference setup, while $\Delta^2(x_1 - x_2)$ is determined through the ghost imaging of the double slit. By further considering the divergence of the down-converted beams and the localization of photons by the double slit, both inequalities in (111) are violated.

7.3. Einstein–Podolsky–Rosen non-locality

In 1935, Einstein, Podolsky and Rosen (EPR) began the ongoing discussion and study of quantum entanglement in their seminal paper “Can Quantum-Mechanical Description of Physical Reality Be Considered Complete?”. EPR argued that quantum mechanics was inconsistent with seemingly reasonable notions of locality and “elements of reality”. Through analysis of a gedanken experiment involving two particles with perfectly correlated position and momentum, they argued that one should be able to attribute well-defined values to complementary physical quantities of one of the particles. This conflicted with the predictions of quantum mechanics, in particular with Bohr’s complementarity principle, quantified by the Heisenberg uncertainty relation. EPR then argued that quantum mechanics must be incomplete. The EPR paradox illustrates the incompatibility between what is now known as *local realism* and the standard quantum theory.

Though EPR considered perfect position and momentum correlations, it is possible to apply the EPR argument to a more realistic setting. Reid and collaborators have shown that EPR-like correlations can be identified by the violation of the inequality [118,119,147]

$$\Delta_{\min}^2(x_1|x_2)\Delta_{\min}^2(p_1|p_2) > \frac{1}{4}. \quad (112)$$

Here $\Delta_{\min}^2(r_1|r_2)$ is the minimum inferred variance, which represents the minimum uncertainty in inferring variable r_1 of system 1 conditioned upon measurement of variable r_2 of system 2. Explicitly,

$$\Delta_{\min}^2(r_1|r_2) = \int d\xi_2 \mathcal{P}(\xi_2) \Delta^2(r_1|\xi_2), \quad (113)$$

where $\Delta^2(r_1|\xi_2)$ is the variance of the conditional probability distribution $\mathcal{P}(r_1|\xi_2)$, which gives the probability of r_1 given that the measurement of system 2 gave result ξ_2 , and $\mathcal{P}(\xi_2)$ is the probability that result ξ_2 is obtained. Inequality (112) was first violated with quadrature measurements of two intense beams [148].

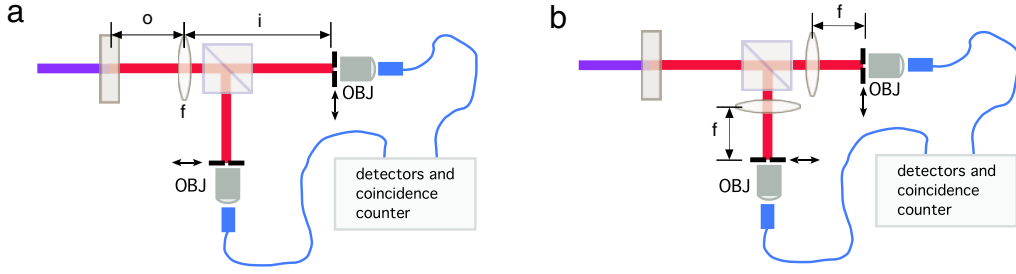


Fig. 27. Experimental setup for test of the EPR criteria performed by Howell et al. [21]. (a) Position measurement are performed by scanning a slit aperture in the image plane of an imaging lens system. (b) Momentum measurements are realized by scanning the slit in the Fourier plane of a lens.

Using SPDC, it is possible to produce a two-photon quantum state that is similar to the original EPR state. The SPDC state (see Section 3) in the limit $w \rightarrow \infty$ and $L \rightarrow 0$ becomes

$$|\psi\rangle_{\text{EPR}} = \int d\mathbf{q} |\mathbf{q}\rangle_1 |-\mathbf{q}\rangle_2 = \int d\mathbf{p} |\mathbf{p}\rangle_1 |\mathbf{p}\rangle_2, \quad (114)$$

where the equality on the right side is obtained by Fourier transform. Inequality (112) for spatial correlations was first tested experimentally by Howell et al. [21], using the experimental setup illustrated in Fig. 27. The near (x) and far-field (p) distributions were measured using an imaging lens system and a Fourier transform lens system, respectively. A value of $\Delta_{\min}^2(x_1|x_2)\Delta_{\min}^2(p_1|p_2) = 0.01 \ll 0.25$ was obtained, demonstrating the high correlation of the spatial degrees of freedom of the photon pairs. The separability condition (104) was also tested and violated.

A thorough discussion of the EPR paradox, including the experimental results to date can be found in a recent review article [147]. As inequality (112) deals with EPR non-locality, it is generally more restrictive than those which identify non-separability of continuous variable systems [116,117]. Recently, it has been shown that violation of the EPR inequality (112) is sufficient to discard “local hidden state” models, which have been related to Schrödinger’s “steering” phenomenon [149–151]. An EPR inequality based on an entropic uncertainty relation was introduced and tested experimentally in Ref. [152].

7.4. Propagation of spatial entanglement

The above experiments show quantum entanglement and EPR non-locality by identifying correlations in the near and far field of the SPDC crystal. In general, after free propagation, the transverse spatial correlations switch from a correlation in the near-field, given by Eq. (107) to an anti-correlation in the far-field, given by Eq. (109). Chan et al. have shown that this change from correlation to anti-correlation implies that at some intermediate plane there must be very little correlation present in the spatial intensity distributions [144]. Following Chan et al., let us consider the case where the cardinal sine function in the momentum configuration is approximated with a Gaussian: $\text{sinc}(bq^2) \propto \exp(-\alpha bq^2)$, with $\alpha = 0.455$ ($\alpha = 0.455$ optimizes the approximation), and the pump is a Gaussian beam. After propagation, the wave function in q -space is

$$\Phi(\mathbf{q}_s, \mathbf{q}_i, z) = C \exp\left[-\frac{a_+ + ib_+(z)}{4}(\mathbf{q}_s + \mathbf{q}_i)^2 - \frac{a_- + ib_-(z)}{4}(\mathbf{q}_s - \mathbf{q}_i)^2\right], \quad (115)$$

where C is a normalization constant and $a_+ = w_o^2/(1 + z_R^2/R^2)$, $a_- = \alpha L/K$, $b_+(z) = 2(z + L)/K + 2R/K(1 + z_R^2/R^2)$, and $b_-(z) = (2z + L)/K$. Here R and z_R are the radius of curvature and Rayleigh range of the Gaussian pump beam in the source plane, respectively. The ρ -space wave-function is the Fourier transform of (115), and is given by

$$\Psi(\mathbf{\rho}_s, \mathbf{\rho}_i, z) = D \exp\left[-\frac{a_+ - ib_+(z)}{4(a_+^2 + b_+^2(z))}(\mathbf{\rho}_s + \mathbf{\rho}_i)^2 - \frac{a_- - ib_-(z)}{4(a_-^2 + b_-^2(z))}(\mathbf{\rho}_s - \mathbf{\rho}_i)^2\right]. \quad (116)$$

One can see that both wave functions (115) and (116) are completely separable (un-entangled) when $a_+ = a_-$ and $b_+(z) = b_-(z)$, and thus $\Psi_{\text{sep}}(\mathbf{\rho}_s, \mathbf{\rho}_i, z) = \psi_s(\mathbf{\rho}_s, z)\psi_i(\mathbf{\rho}_i, z)$. This condition depends upon the initial parameters of the pump beam, as well as the length of the non-linear crystal, and cannot be met by propagation alone. However, at a certain distance $z = z_0$ from the non-linear crystal, such that $a_+[a_-^2 + b_-^2(z_0)] = a_-[a_+^2 + b_+^2(z_0)]$, the modulus squared of the wave function is separable:

$$|\Psi(\mathbf{\rho}_s, \mathbf{\rho}_i, z_0)|^2 = |\psi_s(\mathbf{\rho}_s, z_0)|^2 |\psi_i(\mathbf{\rho}_i, z_0)|^2. \quad (117)$$

Thus, in the transverse plane located a distance $z = z_0$ from the crystal, there is no correlation present in the intensity distribution. Since at z_0 we have $b_+(z_0)(a_-^2 + b_-^2(z_0)) \neq b_-(z_0)(a_+^2 + b_+^2(z_0))$, $\Psi(\mathbf{\rho}_s, \mathbf{\rho}_i, z_0)$ is not separable, and we conclude all initial spatial correlations have “migrated” to the phase of the two-photon state [144]. Thus, to properly identify the

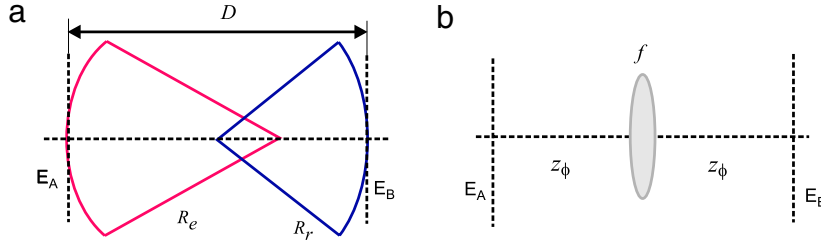


Fig. 28. (a) Free space propagation as an FRFT. (b) Optical lens system used to implement an FRFT.

entanglement present at $z = z_0$, some type of interferometric measurement capable of accessing phase information must be performed [144].

In the above arguments, the phase matching function $\gamma(\mathbf{q})$ is approximated by a Gaussian function, which is necessary for the separability of the modulus of the wave function (117). When considering the phase matching function in the form of a sinc function (in the momentum space), the correlations in principle never completely disappear. Nevertheless, one observes a strong decrease in spatial correlations at $z = z_0$.

Since the correlations present in the two-photon state migrate from the amplitude to the phase due to local unitary evolution in the form of free propagation, it should be possible to retrieve the correlations by undoing the unitary evolution. In this vein, it is convenient to parametrize the evolution in a more general framework.

7.5. Fractional Fourier transform

The analysis of the propagation of spatial correlations can be cast in a general setting using the concept of the fractional Fourier transform (FRFT) [153–156]. Since its first appearance in 1929 [157], the FRFT has found widespread use in quantum mechanics [158–160] as well as signal processing and optics [156]. The FRFT of order ϕ of a function $E(\xi)$ can be defined by the integral transform [154]

$$\mathcal{F}_\phi[E](\xi) = \iint F_\phi(\xi, \zeta) E(\zeta) d\zeta, \quad (118)$$

where the FRFT kernel is given by

$$F_\phi(\xi, \zeta) = \frac{i \exp(-i\phi)}{2\pi \sin \phi} \exp\left(-i \frac{\xi^2 \cot \phi}{2} - i \frac{\zeta^2 \cot \phi}{2} + i \frac{\xi \cdot \zeta}{\sin \phi}\right), \quad (119)$$

and ζ and ξ are two-dimensional variables. Note that $\phi = \pi/2$ corresponds to the usual Fourier transform. Furthermore, in the limit $\phi \rightarrow 0$, $F_0 \rightarrow \delta(\zeta - \xi)$, and when $\phi \rightarrow \pi$ the kernel $F_\pi \rightarrow \delta(\zeta + \xi)$. Just as the Fourier transform appears naturally in the context of Fraunhofer diffraction, it has been shown that the FRFT appears in the Fresnel diffraction regime [154]. To identify ordinary free space propagation with the fractional Fourier transform it is necessary to choose properly scaled coordinates [154]. Consider the usual Fresnel diffraction integral corresponding to the propagation of a field from the plane A to plane B, as shown in Fig. 28(a). Choosing dimensionless coordinates $\zeta = \sqrt{k \tan \phi / D} \rho$ and $\xi = \sqrt{k \sin \phi \cos \phi / D} \rho'$, where D the distance between planes, leads to

$$E_B(\xi) = \exp(i\phi) \cos \phi \exp(-i\xi^2 \tan \phi / 2) \mathcal{F}_\phi[E_A](\xi), \quad (120)$$

which expresses E_B as a FRFT of E_A multiplied by a phase term [154]. It is possible to eliminate the phase term if one observes the output field on a spherical surface of radius $R_\phi = -D / \sin^2 \phi$, as shown in Fig. 28(a). This spherical surface can also be mapped to a plane using a lens with focal length equal to $-R_\phi$.

It has also been shown that one can implement a FRFT using lenses [161,155]. For example, consider the symmetrical optical system shown in Fig. 28(b). Here l is the focal length of the lens and z is the propagation distance before and after the lens. Using $z = 2l \sin^2(\phi/2)$ and $f = l \sin \phi$, it has been shown that this optical system implements a FRFT operation given by

$$\mathcal{F}_\phi[E](\rho') = \iint F_\phi\left(\frac{k}{f} \rho', \frac{k}{f} \rho\right) E(\rho) d\rho, \quad (121)$$

which is equivalent to the transform given in Eq. (118) when one chooses scaled variables $\zeta = \sqrt{k/f} \rho$ and $\xi = \sqrt{k/f} \rho'$.

A generic optical system consisting of lenses, mirrors and sections of free space can be described in terms of FRFTs by scaling the transverse spatial coordinates appropriately. The convenience of the FRFT comes from the fact that it can be viewed as a simple rotation in phase space. This can be seen most easily using geometrical optics. Consider the

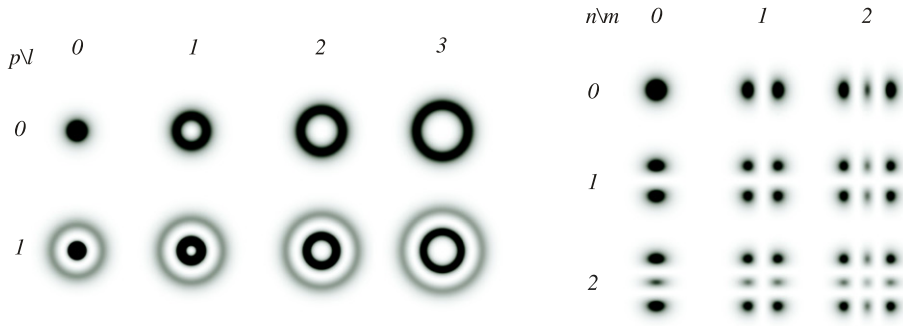


Fig. 29. Laguerre–Gaussian and Hermite–Gaussian modes.

symmetrical lens system shown in Fig. 28(b). Free propagation of an optical ray $\mathbf{r} = (r, \theta)$ can be represented by the ABCD matrix [162]

$$S_z = \begin{pmatrix} 1 & z \\ 0 & 1 \end{pmatrix}, \quad (122)$$

where z is the propagation distance. Passage through a thin lens is described by the matrix

$$L_l = \begin{pmatrix} 1 & 0 \\ -1/l & 1 \end{pmatrix}, \quad (123)$$

where l is the focal length of the lens. Choosing $z = 2l \sin^2(\phi/2)$ and defining $f = l \sin \phi$ as a scaled focal length, the complete optical FRFT system is given by the matrix

$$F_\phi = S_z L_l S_z = \begin{pmatrix} \cos \phi & f \sin \phi \\ -\frac{1}{f} \sin \phi & \cos \phi \end{pmatrix}. \quad (124)$$

Matrix (124) represents a ϕ -order FRFT, and is recognized as a rotation matrix scaled by f . This scaling is necessary since r has dimension of length and θ is adimensional, and thus the scaled focal length f acts on θ so that $f\theta$ has dimension of length. If the scaled focal lengths f of two FRFTs are equal, it is easy to see from the ray matrix in Eq. (124) that the FRFT is additive, that is $F_{\phi_1} F_{\phi_2} = F_{\phi_1 + \phi_2}$, such that the order of the combined optical FRFT is $\phi_1 + \phi_2$. By introducing the FRFT with properly scaled coordinates, and using the additivity property, one can describe propagation through any first-order optical system consisting of lenses, mirrors and free space. Propagation is now parametrized solely by the order of the overall FRFT, given by the angle ϕ .

In quantum-mechanical operator formalism, the FRFT operator is defined as [156]

$$\mathbf{F}_\phi \equiv e^{i\phi/2} \exp \left[-i \frac{\phi}{2} (\mathbf{x}^2 + \mathbf{p}^2) \right], \quad (125)$$

where \mathbf{x} and \mathbf{p} are the dimensionless position and momentum operators satisfying $[\mathbf{x}, \mathbf{p}] = i$. This operator is equivalent to the evolution operator of the quantum harmonic oscillator, which has the hamiltonian $\mathbf{H} = (\mathbf{x}^2 + \mathbf{p}^2)/2$. Application of the FRFT operator \mathbf{F}_ϕ to the \mathbf{x} and \mathbf{p} corresponds to rotation of angle ϕ in phase space [161,156]:

$$\mathbf{F}_\phi^\dagger \begin{pmatrix} \mathbf{x} \\ \mathbf{p} \end{pmatrix} \mathbf{F}_\phi = \begin{pmatrix} \cos \phi & \sin \phi \\ -\sin \phi & \cos \phi \end{pmatrix} \begin{pmatrix} \mathbf{x} \\ \mathbf{p} \end{pmatrix} \equiv \begin{pmatrix} \mathbf{x}_\phi \\ \mathbf{p}_\phi \end{pmatrix}, \quad (126)$$

where \mathbf{x}_ϕ and \mathbf{p}_ϕ are the rotated operators.

The FRFT is a rotation in the x, p phase space. In this respect, it can be used to measure the marginal probability distribution along any axis in phase space, and to perform tomography of the spatial Wigner function [163,164]. We note that spatial tomography of a field can also be performed using interference of rotated and displaced halves of the field [165,166].

7.6. Correlations at intermediate planes

To describe the spatial correlations of photon pairs at some propagation distances z_s and z_i , through arbitrary first-order optical systems, it suffices to consider FRFT's of arbitrary order angle α and β . A two-photon state $|\Psi\rangle$ after arbitrary

propagation is given by $|\Psi_{\alpha,\beta}\rangle = \mathbf{F}_{\alpha}^{(1)} \otimes \mathbf{F}_{\beta}^{(2)} |\Psi\rangle$. The two-photon wave function then becomes $\Psi_{\alpha,\beta}(x_1, x_2) = \langle x_1, x_2 | \Psi_{\alpha,\beta} \rangle$, where

$$\begin{aligned} \Psi_{\alpha,\beta}(x_1, x_2) &= \iint dx'_1 dx'_2 \langle x_1 | \mathbf{F}_{\alpha} | x'_1 \rangle \langle x_2 | \mathbf{F}_{\beta} | x'_2 \rangle \Psi(x'_1, x'_2) \\ &= \iint dx'_1 dx'_2 F_{\alpha}(x_1, x'_1) F_{\beta}(x_2, x'_2) \Psi(x'_1, x'_2), \end{aligned} \quad (127)$$

and the kernels are defined in Eq. (119). For simplicity, we consider only one spatial dimension. As an example, let us consider the propagation of the EPR state in one dimension

$$|\Psi^{\text{EPR}}\rangle = \iint dx_1 dx_2 \delta(x_1 - x_2) |x_1\rangle_1 |x_2\rangle_2, \quad (128)$$

which presents a perfect correlation, since detection of photon 2 at position x projects photon 1 onto a position eigenstate $|x\rangle$. This situation is approximated by the state produced by SPDC when the pump beam can be treated as a plane wave. This state evolves to [167]

$$|\Psi_{\alpha,\beta}^{\text{EPR}}\rangle = A_{\alpha+\beta} \iint dx_1 dx_2 \exp \left[i \frac{\cot(\alpha + \beta)}{2} (\rho_1^2 + \rho_2^2) \right] \exp \left[-i \frac{x_1 \cdot x_2}{\sin(\alpha + \beta)} \right] |x_1\rangle_1 |x_2\rangle_2. \quad (129)$$

We can now analyze the type of correlations present. Whenever $\alpha + \beta = 0 \pmod{2\pi}$, the original state (128) is recovered. That is, the EPR state (128) is an eigenstate of operators of the type $\mathbf{F}_{\alpha} \mathbf{F}_{2\pi-\alpha}$, $\mathbf{F}_{\alpha} \mathbf{F}_{4\pi-\alpha}$, etc. When $\alpha + \beta = \pi \pmod{2\pi}$, the correlated EPR state (128) evolves to an anticorrelated EPR state

$$|\Phi^{\text{EPR}}\rangle = \iint dx_1 dx_2 \delta(x_1 + x_2) |x_1\rangle_1 |x_2\rangle_2. \quad (130)$$

In this case the detection of photon 2 at x projects photon 1 onto the state $|-x\rangle$. When $\alpha + \beta = \pi/2 \pmod{2\pi}$, this state becomes

$$|\Omega\rangle = \int dx |x\rangle_1 |p(x)\rangle_2, \quad (131)$$

which presents no intensity correlation. Here $|p(x)\rangle \propto \int \exp(ip(x) \cdot x) |x\rangle$ is the momentum eigenstate conjugate to $|x\rangle$. An equivalent result is found for $\alpha + \beta = 3\pi/2 \pmod{2\pi}$. We note that the conditions for correlation, anti-correlation, and no-correlation depend on the sum of the FRFT angles of the down-converted fields, and not the individual angles α and β . Thus, for any propagation characterized by an FRFT \mathcal{F}_{α} on photon 1, one can find a suitable transformation \mathcal{F}_{β} on photon 2 such that a correlation, anti-correlation or no intensity correlation is recovered. These conditions were tested experimentally in Ref. [167].

This simple picture drawn for the ideal EPR-state is followed approximately by the two-photon state in Eq. (116). Let us consider two simple cases. First, let us assume that the FRFT angles are the same for both down-converted photons: $\alpha = \beta$. Then, no intensity correlation is observed whenever

$$\cot^2 \alpha = \frac{a_-(a_+^2 + b_+^2) - a_+(a_-^2 + b_-^2)}{a_+ - a_-}, \quad (132)$$

where parameters a_{\pm} and b_{\pm} are defined in (115) and b_{\pm} refers to $b_{\pm}(z)$ at the crystal plane. Consider another simple case in which $b_+ = b_- = 0$ at the crystal face, with no restriction on α and β . Analytical calculation shows that, in order to have no intensity correlation,

$$\cot \alpha \cot \beta = a_- a_+. \quad (133)$$

Eq. (133) is satisfied by FRFT orders such that $\alpha + \beta = \pi/2 \pmod{2\pi}$ or $\alpha + \beta = 3\pi/2 \pmod{2\pi}$ only when $a_- = 1/a_+$. Nevertheless, the intensity correlations present in the state Eq. (116) propagate in a fashion similar to an idealized case of the EPR state.

The above arguments apply to intensity correlations, the absence of which does not necessarily imply that a quantum state is separable. Let us now discuss the identification of entanglement via intensity correlations of transverse spatial variables. The DGCZ inequality (105) for transverse variables rotated using the FRFT operator (126) is [168]:

$$\begin{aligned} \langle (\Delta \mathbf{X}'_-)^2 \rangle + \langle (\Delta \mathbf{P}'_+)^2 \rangle &= \frac{1 + \cos(\alpha + \beta)}{2} [\langle (\Delta \mathbf{X}_-)^2 \rangle + \langle (\Delta \mathbf{P}_+)^2 \rangle] + \frac{1 - \cos(\alpha + \beta)}{2} [\langle (\Delta \mathbf{X}_+)^2 \rangle + \langle (\Delta \mathbf{P}_-)^2 \rangle] \\ &\quad - \frac{\sin(\alpha + \beta)}{2} [\langle \{\mathbf{X}_+, \mathbf{P}_+\} \rangle - 2\langle \mathbf{X}_+ \rangle \langle \mathbf{P}_+ \rangle] + \frac{\sin(\alpha + \beta)}{2} [\langle \{\mathbf{X}_-, \mathbf{P}_-\} \rangle - 2\langle \mathbf{X}_- \rangle \langle \mathbf{P}_- \rangle], \end{aligned} \quad (134)$$

where $\mathbf{X}'_{\pm} \equiv \mathbf{x}_{\alpha} - \mathbf{x}_{\beta}$ and $\mathbf{P}'_{\pm} \equiv \mathbf{p}_{\alpha} + \mathbf{p}_{\beta}$, are defined in terms of the rotated variables, and $\mathbf{X}_{\pm} = \mathbf{x}_1 - \mathbf{x}_2$ and $\mathbf{P}_{\pm} = \mathbf{p}_1 + \mathbf{p}_2$ in terms of the variables at the source. The sum of variances for the rotated variables coincides with the sum of variances

for the variables at the source when $\alpha + \beta \pmod{2\pi} = 0$. If the two-photon state is entangled, with intensity correlation in the \mathbf{x} and \mathbf{p} variables at some initial plane, then, for any propagation of the signal photon, characterized by α , it is possible to find a propagation of the idler field, characterized by β , so that an intensity correlation is recovered and entanglement can be identified. It is important to note that Eq. (134) does not depend on the state and is applicable to any bipartite continuous variable systems. Eq. (134) was experimentally tested for intermediate propagation planes of SPDC photons in Ref. [168].

8. Transverse modes

A simple way to describe spatial correlations in the paraxial regime is through the use of transverse spatial modes described by discrete indices, such as the Laguerre Gaussian (LG) modes or the Hermite Gaussian (HG) modes. Like the well known Gaussian beam, the Hermite–Gaussian and Laguerre–Gaussian beams are also solutions to the paraxial Helmholtz Eq. (41) [35]. In Section 8.1, we will introduce the Laguerre Gaussian modes, which have well defined orbital angular momentum (OAM). In Section 8.2 we review the conservation of OAM in SPDC and the generation of entangled OAM states. In Sections 8.5 and 8.6 we present the Hermite–Gaussian modes and their application to SPDC.

8.1. Laguerre Gaussian modes: orbital angular momentum of light

Since the 1990's it has been known that any electromagnetic paraxial beam with an azimuthal phase dependence of the form $e^{i\ell\phi}$ carries an orbital angular momentum ℓh per photon [169]. The Laguerre–Gaussian beams are probably the most well-known and studied examples of beams carrying orbital angular momentum. They are given by [170]

$$U_p^\ell(\rho, \phi, z) = D_p^\ell \frac{1}{w(z)} \left(\frac{\sqrt{2}\rho}{w(z)} \right)^\ell L_p^\ell \left(\frac{2\rho^2}{w(z)^2} \right) \exp \left(-\frac{\rho^2}{w(z)^2} \right) \times \exp \left\{ -i \left[\frac{k\rho^2}{2R} - (n+m+1)\gamma(z) \right] - (p-\ell)\phi \right\}, \quad (135)$$

where (ρ, ϕ, z) are the usual cylindrical coordinates, D_p^ℓ is a constant which depends on the azimuthal index ℓ and radial index p . L_p^ℓ are the Laguerre polynomials. Here z is the longitudinal propagation direction, $R(z)$ is the radius of curvature, $w(z)$ is the beam waist, and $\gamma(z)$ is the phase retardation or *Gouy phase*. The parameter z_R is the *Rayleigh range*. The order of the LG beam is defined as $\mathcal{N} = |\ell| + 2p$. The usual Gaussian beam is the zeroth-order U_0^0 beam. See plots of LG modes in Fig. 29(left).

In addition to interesting implications in classical and quantum optics, the orbital angular momentum of a light field raises possibilities for technical applications. It has been shown that the orbital angular momentum of light can be used to rotate micro-particles in optical traps [171]. In terms of quantum optical applications, the orbital angular momentum of single photons in LG modes provides a possible d -dimensional qudit encoding scheme [172–177], which allows for the creation of multi-dimensional entanglement in discrete bases. Devices that discriminate the orbital angular momentum of Laguerre–Gaussian beams have been proposed [178] and experimentally tested [179,180].

8.2. Entanglement and conservation of orbital angular momentum in SPDC

The first experimental investigation of OAM conservation in SPDC suggested that OAM is not conserved [181], in contrast to previous experimental investigations of other non-linear optical processes such as second-harmonic generation (SHG). Using an LG mode as the fundamental beam in SHG showed a conservation relation, such that the OAM of the second-harmonic beam is double that of the fundamental beam: $\ell_{\text{SH}} = 2\ell_{\text{fund}}$ [182,183]. In these experiments, the intensity and phase structure of the output beam was observed using a CCD camera. The same measurement method was used in the inverse experiment, investigation of OAM conservation in SPDC by Arlt et al. [181]. However, by imaging the near and far field of the collinear down-converted fields using a CCD camera, correlations in second-order are observed. Theoretical investigations by Arnaut and Barbosa showed that, under suitable experimental conditions, OAM conservation appears only in fourth-order [172]. The two-photon state has well-defined OAM equal to that of the pump beam, and $\ell_{\text{signal}} + \ell_{\text{idler}} = \ell_{\text{pump}}$. Moreover, they showed that the two-photon state is entangled in OAM, and thus the individual signal and idler beams do not have well defined OAM. For this reason, the experiment by Arlt et al. did not observe OAM conservation. Shortly thereafter, a clever experiment by Mair et al. confirmed the conservation and entanglement of OAM in SPDC [184].

The experiment by Mair et al. [184] is illustrated in Fig. 30. The OAM correlation was measured using forked holographic masks and single-mode optical fibers to project onto individual OAM values of m . The forked hologram mask functions in much the same way as a diffraction grating. A Gaussian mode passing through a mask with m dislocations and diffracting into the n th-order becomes an LG mode with $l = mn$. The detection scheme of Mair et al. exploits this process in the reverse. A mode with OAM m that diffracts into the first-order of a forked mask with m dislocations will now be in a Gaussian mode. Single mode fibers are used to select only those photons in the Gaussian mode, which are then registered by single photon detectors. The pump laser beam with $l = -1, 0, 1$ was shown to produce entangled photons with $m_{\text{signal}} = l - m_{\text{idler}}$.

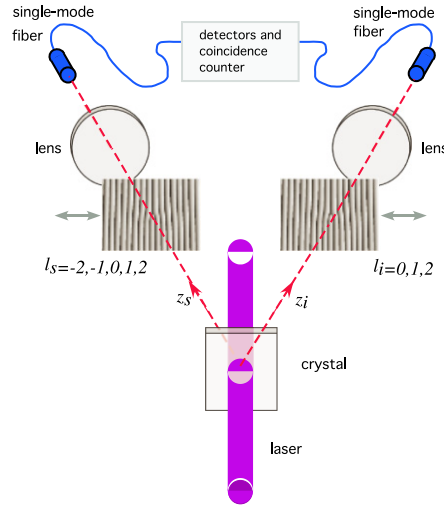


Fig. 30. First measurement of OAM entanglement in SPDC by Mair et al. [184]. Forked holographic masks of OAM l_s and l_i are used in conjunction with lenses and single mode-optical fibers to project onto modes with well-defined OAM. To project onto superpositions of OAM, the masks are shifted in the transverse direction.

However, this confirms only a classical correlation between the OAM of the down-converted photons. To prove that the photons are indeed entangled in OAM, Mair et al. projected the photons onto superpositions of OAM states. This was done by shifting the position of the holographic mask. A shifted mask with m dislocations and the single-mode fiber detection scheme described above projects the single-photons onto superposition states of the form $\alpha |0\rangle + \beta |m\rangle$, where α and β depend on the position of the mask.

The two-photon state for frequency degenerate down-converted fields ($\lambda_s = \lambda_i = 2\lambda_p$) in a quasi-collinear geometry can be decomposed in terms of LG modes in a relatively simple form [172,185–187]. The wave function in this case can be written as

$$\Psi(\rho_s, \rho_i) = U_p^l \left(\frac{\rho_s + \rho_i}{\sqrt{2}} \right) \mathcal{F} \left(\frac{\rho_s - \rho_i}{\sqrt{2}} \right), \quad (136)$$

where U_p^l describes the pump beam profile and \mathcal{F} is the phase-matching function.

Decomposing this wave function into signal and idler LG modes results in an alternative form:

$$\Psi(\rho_s, \rho_i) = \sum_{l_s, p_s} \sum_{l_i, p_i} N_{p_s p_i}^{l_s l_i} U_{p_s}^{l_s}(\rho_s) U_{p_i}^{l_i}(\rho_i), \quad (137)$$

where the coefficient $N_{p_s p_i}^{l_s l_i}$ is given by [186]

$$N_{p_s p_i}^{l_s l_i} = \iint d\rho_s d\rho_i U_p^l \left(\frac{\rho_s + \rho_i}{\sqrt{2}} \right) \mathcal{F} \left(\frac{\rho_s - \rho_i}{2} \right) U_{p_s}^{*l_s}(\rho_s) U_{p_i}^{*l_i}(\rho_i). \quad (138)$$

Assuming that the crystal length L is much smaller than the Rayleigh range z_R of the pump beam, and the function $\mathcal{F} \sim 1$, the coefficient $N_{p_s p_i}^{l_s l_i}$ becomes

$$N_{p_s p_i}^{l_s l_i} \propto \delta_{l_s + l_i, l} \int q dq v_p^l(\sqrt{2}q) v_{p_s}^{*l_s}(q) v_{p_i}^{*l_i}(q), \quad (139)$$

where $v_p^l(q)$ is the Fourier transform of the radial component of $U_p^l(\rho)$. The presence of the Kronecker delta function guarantees that OAM is conserved: $l_i + l_s = l$, and the down-converted signal and idler photons are emitted with correlated OAM. For simplicity, let $|m\rangle$ denote a single photon state carrying an orbital angular momentum $m\hbar$ and l be the azimuthal index of the LG pump beam. Coherence of the SPDC process guarantees that the two-photon state can be written as a Schmidt decomposition of the form [145]

$$|\psi\rangle = \sum_{m=-\infty}^{+\infty} P_m |l-m\rangle |m\rangle. \quad (140)$$

Here the states $|m\rangle$ represent spatial modes with well-defined OAM m .

The derivation of the two-photon state (140) is valid for quasi-collinear paraxial fields in the thin-crystal approximation. Other effects, such as the birefringence and anisotropy of the non-linear medium, as well as a non-collinear geometry, were

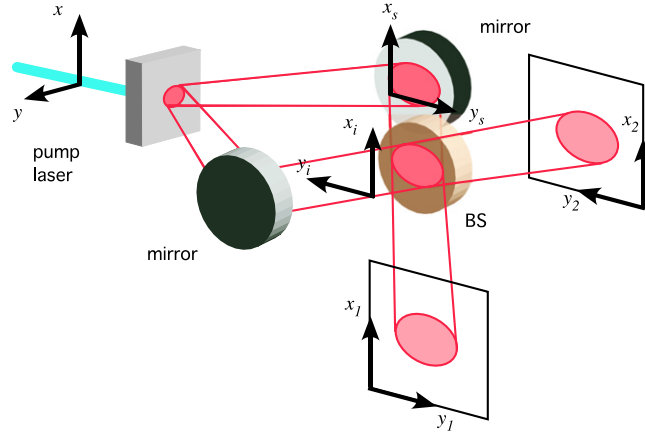


Fig. 31. Illustration of Hong–Ou–Mandel interference with multiple spatial modes.

ignored. Some authors have studied SPDC and OAM conservation in more general contexts [45,43,188]. A comprehensive discussion has been provided recently by Osorio et al. [188]. They have shown that when one considers all the photon pairs produced by the crystal, distributed along the entire down-conversion cone, OAM is conserved. In a more realistic setting, in which signal and idler photons are detected in small regions of the down-conversion cone, the two-photon wave function may be spatially asymmetric and not reproduce the angular spectrum of the pump beam. The deformation generally corresponds to an ellipticity that depends upon the non-collinear angle φ , the crystal length, and the width of the pump beam w , and can be quantified by the quantity $L_d = w/\sin \varphi$. When the crystal length $L \ll L_d$, the two-photon wave function reproduces the transverse field of the pump beam, and OAM is conserved. If this condition is not fulfilled, the two-photon wave function is not given by $\Psi(\rho_s, \rho_i) = U_p^l \left(\frac{\rho_s + \rho_i}{\sqrt{2}} \right)$, and OAM will not be conserved. Ellipticity of the two-photon spatial wave function caused by non-collinear geometry and focusing of the pump beam has been observed experimentally [47]. Torres et al. [189] have considered the extreme situation in which the down-converted fields are either counter-propagating and perpendicular to the pump field, or co-propagating with respect to each other but counter-propagating to the pump field. In these cases the usual OAM selection rule (as in the collinear geometry above) does not apply.

Another consideration is the spatial walk-off caused by the birefringence of the non-linear SPDC crystal, which occurs for either the pump and/or one of the down-converted fields. In the case of type-I down-conversion, in which only the pump field is polarized in the extraordinary direction, the critical parameter is the “walk-off length” $L_w = w/\tan \rho_0$ [43,188]. Here ρ_0 is the spatial walk-off angle, which depends upon the extraordinary refractive index and the propagation direction in the crystal. When the length of the non-linear crystal $L \ll L_w$, the effect of walk-off on the shape of the two-photon wave function is negligible, and OAM is conserved [44].

8.3. Probing the phase structure of the two photon state: two-photon interference

Two-photon interference at a beam splitter was first demonstrated by Hong, Ou and Mandel (HOM) [190]. It has subsequently become the key process for two-photon quantum logic, and is used in quantum information protocols such as Bell-state measurements [191,192] and to construct two-photon logic gates [193–197]. On the one hand, these applications are designed for perfect interference with a single spatial mode. On the other hand, multimode interference is a useful method to probe the transverse phase structure of the two-photon state [198,199], and has been used to show the conservation of orbital angular momentum in SPDC [186], as well as to quantify spatial entanglement [200]. It has also been shown to be useful in Bell-state analysis of polarization entangled photons [201], and to produce two-photon fields exhibiting spatial antibunching [113].

Let us illustrate the probing of the phase structure. Consider the HOM interferometer shown in Fig. 31, in which two photons are generated by SPDC and then reflected onto opposite sides of a beam splitter (BS). If the path length difference is greater than the coherence length of the down-converted photons, then there is no interference and the photons leave either side of the beam splitter randomly. Here we will assume that lengths of paths s and i are equal. Using the reference frames illustrated in Fig. 31, the annihilation operators in exit modes 1 and 2 *after* the beam splitter can be expressed in terms of the operators in input modes s and i :

$$\mathbf{a}_1(\mathbf{q}, \sigma) = t\mathbf{a}_s(q_x, q_y, \sigma) + i r\mathbf{a}_i(q_x, -q_y, \sigma), \quad (141a)$$

$$\mathbf{a}_2(\mathbf{q}, \sigma) = t\mathbf{a}_i(q_x, q_y, \sigma) + i r\mathbf{a}_s(q_x, -q_y, \sigma), \quad (141b)$$

where σ is the polarization, q_x and q_y are the transverse components of the momentum and t and r are respectively the transmission and reflection coefficients of the beam splitter ($|t|^2 + |r|^2 = 1$). A field reflected from the beam splitter

undergoes a spatial inversion in the horizontal (y) direction, while a transmitted field does not suffer any inversion, as illustrated in Fig. 31. The negative sign that appears in the q_y components of the reflected field is due to this spatial inversion. The two-photon wave function is split into four components, according to the four possibilities of transmission and reflection of the two photons [198,199]:

$$\Psi_{tr}(\mathbf{r}_+, \mathbf{r}_-) = \Psi_{rt}(\mathbf{r}_+, \mathbf{r}_-) = itr \exp \left\{ \frac{2iK}{Z} (x_-^2 + y_-^2) \right\} [\mathcal{W}(x_+, -y_-, Z) + \mathcal{W}(x_+, y_-, Z)], \quad (142)$$

$$\Psi_{tt}(\mathbf{r}_+, \mathbf{r}_-) = t^2 \exp \left\{ \frac{2iK}{Z} (x_-^2 + y_-^2) \right\} \mathcal{W}(x_+, y_+, Z), \quad (143)$$

$$\Psi_{rr}(\mathbf{r}_+, \mathbf{r}_-) = -r^2 \exp \left\{ \frac{2iK}{Z} (x_-^2 + y_-^2) \right\} \mathcal{W}(x_+, -y_+, Z), \quad (144)$$

where $\mathbf{r}_\pm = (x_\pm, y_\pm) = (x_s/2 \pm x_i/2, y_s/2 \pm y_i/2)$. Let us assume that $t = r = 1/\sqrt{2}$. If the pump beam profile \mathcal{W} is symmetric with respect to the y coordinate ($\mathcal{W}[y] = \mathcal{W}[-y]$), then the two photons always leave in the same output port of the BS, since the amplitude for coincidence counts in different output ports is $\Psi_{tt} + \Psi_{rr} = 0$. This results in the usual HOM interference dip. If \mathcal{W} is antisymmetric with respect to y ($\mathcal{W}[y] = -\mathcal{W}[-y]$), then $\Psi_{tr} = \Psi_{rt} = 0$, and the photons always leave the BS in different output ports, giving an interference peak.

The analysis above considered that all other degrees of freedom are in symmetric states. Combining the spatial degrees of freedom with the polarization degree of freedom, for instance, provides a way to control two-photon interference of different polarization states. This allows for partial Bell-state analysis in the coincidence basis [201], as well as for the creation of a two-photon “singlet” beam, in which the photon pairs in the same beam are in an anti-symmetric polarization state, and consequently are spatially antibunched [113].

Other experiments have used two-photon interference to probe the phase structure of the two-photon state, and have shown that the down-converted photon pairs are entangled in OAM [186,199]. For a pump beam in a LG mode, the two-photon coincidence detection probability at the output of the HOM interferometer is

$$P(\mathbf{r}_1, \mathbf{r}_2) \propto |u_p^\ell(R)|^2 \sin^2 l\theta, \quad (145)$$

where $u_p^\ell(R)$ is the radial component of the LG mode, ℓ is the OAM of the pump beam which is transferred to the two-photon state, $R = |\boldsymbol{\rho}_1 + \boldsymbol{\rho}_2|$, and $\sin \theta = (\rho_1 \sin \phi_1 + \rho_2 \sin \phi_2)/R$. When $\mathbf{r}_2 = 0$, the coincidence profile is $P(\mathbf{r}_1, 0) \propto |u_p^\ell(\rho_1/\sqrt{2})|^2 \sin^2 \ell\phi_1$. Thus, fixing one detector and scanning the other, oscillations with period ℓ will appear in the azimuthal coordinate ϕ_1 . In Ref. [186], the phase structure was observed for LG pump beams with $\ell = 1, 2$.

8.4. Quantifying spatial entanglement

In Section 7, the detection of spatial entanglement using entanglement witnesses was discussed. In many cases, these witnesses involve only a few measurements of the transverse spatial variables. Quantifying spatial entanglement, on the other hand, presents a considerable challenge, due to the large dimensionality of the involved Hilbert spaces. Nonetheless, theoretical and experimental methods exist which allow for the quantification of bipartite spatial entanglement of photon pairs.

8.4.1. Schmidt decomposition of SPDC

The Schmidt decomposition [202] of the two-photon state produced by SPDC has been derived by Law and Eberly [145]. Absorbing any phase factors into the states $|m\rangle$ allows one to write the two-photon amplitude (140) in the form [145]

$$\Psi(\boldsymbol{\rho}_s, \boldsymbol{\rho}_i) = \sum_{m=-\infty}^{+\infty} \sum_{n=0}^{\infty} \sqrt{\lambda_{n,m}} u_{n,l-m}(\boldsymbol{\rho}_s) u_{n,m}(\boldsymbol{\rho}_i), \quad (146)$$

where the real numbers $\lambda_{n,m}$ are the eigenvalues of the reduced density operators. The functions $u_{n,m}$ are normalized transverse mode functions with well-defined OAM [145]. The entanglement depends upon the number of non-zero Schmidt coefficients $\lambda_{n,m}$. Each $\lambda_{n,m}$ depends on the OAM ℓ , wavenumber and width of the pump laser beam, and the length of the non-linear crystal, and can be calculated by determining the overlap integral of the product of mode functions with the two-photon amplitude given in Eq. (136):

$$\sqrt{\lambda_{n,m}} = \int \boldsymbol{\rho}_s \boldsymbol{\rho}_i u_{n,l-m}^*(\boldsymbol{\rho}_s) u_{n,m}^*(\boldsymbol{\rho}_i) U_p^l \left(\frac{\boldsymbol{\rho}_s + \boldsymbol{\rho}_i}{\sqrt{2}} \right) \mathcal{F} \left(\frac{\boldsymbol{\rho}_s - \boldsymbol{\rho}_i}{\sqrt{2}} \right). \quad (147)$$

Again, effects due to crystal anisotropy and non-collinear geometry have been ignored. Law and Eberly [145] have used the decomposition (146) to calculate the entanglement of the two-photon state generated by a Gaussian pump beam using the so-called Schmidt number, $S = 1/\sum_{n,m} \lambda_{n,m}^2$ [145]. They have shown that the entanglement depends upon the parameter

$L/2z_R$, where z_R is the Rayleigh range of the pump beam and L is the crystal length. If one approximates the phase matching function by a Gaussian function with the same variance, $\gamma(\mathbf{q}) \approx \exp(-L\mathbf{q}^2/8K)$ [144], the Schmidt number in this case can be put in the analytical form $S = (\sqrt{L/4z_R} + \sqrt{4z_R/L})^2/4$. The entanglement in this Gaussian approximation serves as a lower bound, since Gaussian states are always less entangled than non-Gaussian states with the same covariance matrix [203].

For typical values of the experimental parameters, the predicted Schmidt number can be very large. For example, for $L = 1$ mm and $z_R = 1$ m, the predicted Schmidt number is on the order of 10^3 . However, as has been pointed out by van Exter et al. [204], and Osorio et al. [188], even in the case of collinear propagation and negligible crystal anisotropy, this does not necessarily correspond to the usable entanglement present in a realistic experimental scenario. The effect of spatial filtering due to the finite spatial bandwidth of an optical setup is to decrease the Schmidt number, and hence the entanglement. This can be a rather large effect, of several orders of magnitude.

In Ref. [205], Di Lorenzo Pires et al. demonstrated that for the case of a two-photon pure state such as (59), the overall Schmidt number (including contributions from radial and azimuthal parameters) is given by the inverse of the overall degree of coherence of either down-converted field. Assuming that – say – the signal field is quasihomogeneous, the Schmidt number takes the form

$$S \approx \frac{1}{(2\pi)^2} \frac{[\int I_{nf}(\rho_s) d\rho_s]^2 [\int I_{ff}(\mathbf{q}_s) d\mathbf{q}_s]^2}{\int I_{nf}^2(\rho_s) d\rho_s \int I_{ff}^2(\mathbf{q}_s) d\mathbf{q}_s}, \quad (148)$$

where I_{nf} and I_{ff} are the near-field and far-field intensity distributions of the signal photon field, respectively. Thus, through second-order intensity measurements, the spatial entanglement of the two-photon state can be determined. It was shown that the entanglement depends critically on the collinear phase mismatch [205]. Schmidt numbers above 400 were obtained experimentally.

An experimental technique to measure the Schmidt number associated with the OAM decomposition (146) was developed by Peeters et al. [200], who investigated multimode HOM interference in the presence of image rotation of the signal beam before the beam splitter. They showed that the amount of spatial entanglement can be inferred from the visibility of the HOM dip:

$$V(\vartheta) = \sum_{m=-\infty}^{\infty} P_m \cos(2m\vartheta), \quad (149)$$

where ϑ is the angle of image rotation of the signal field. Here P_m are the coefficients of the Schmidt decomposition (140). To quantify spatial entanglement, an azimuthal Schmidt number can be defined as $S_{az} = (\sum_{m=-\infty}^{\infty} P_m^2)^{-1}$. The Schmidt coefficients can be determined by measuring $V(\vartheta)$ for a number of values of ϑ and inverting the Fourier series (149). In Ref. [200], this was done for a number of different types of spatial filtering systems. Schmidt numbers as high as 7.3 ± 0.3 were determined experimentally. More recently, Di Lorenzo Pires et al. performed a similar experiment in a collinear geometry using a bucket detector system [206]. This impressive experiment allowed for the measurement of the complete OAM distribution of the correlated down-converted photons, and Schmidt numbers above 35 were measured. This was in excellent agreement with theoretical predictions based on the experimental parameters. It was also shown that the phase mismatch could be used to increase the entanglement. In this case, the mismatch could be controlled through the temperature of the periodically poled crystal.

Another method to quantify entanglement using multimode HOM interference has been proposed in [146]. In this scheme, it is possible to measure the concurrence directly using two copies of the quantum state [207,208].

An interesting series of experiments have been performed employing phase plates and single-mode fibers to detect and analyze spatial entanglement [209–211]. Two main types of phase plates have been investigated: spiral phase plates and Heaviside step plates. When a Gaussian mode passes through a half-integer spiral phase plate, it is transformed into a superposition of LG modes, given by [212]

$$\sum_{p,\ell} |C_{p,\ell}| e^{if_{p,\ell}(\alpha)} U_p^\ell(\rho, \phi), \quad (150)$$

where $f_{p,\ell}(\alpha)$ is a function which depends upon the orientation angle α of the phase plate. By considering the inverse scenario, it is apparent that the spiral phase plate transforms the superposition (150) into a Gaussian mode, which can be selected with a single mode optical fiber. By changing the orientation angle α of the plate, one can project onto a number of superposition states of the form (150). In Ref. [212] it was shown that the number of non-zero terms in the superposition (150) can be quite large ($\sim 10^2 - 10^3$), and depends upon the half-integer value of the plate.

Half-integer spiral phase plates were used to observe fractional OAM entanglement in down-converted photons [209]. The experimental setups are similar to that of Fig. 30, with the forked holographic masks replaced by the phase plates. The coincidence detection probability, given by [209]

$$P(\alpha_s, \alpha_i) \propto (\pi - |\alpha_s - \alpha_i|)^2, \quad (151)$$

depends only upon the relative angle $|\alpha_s - \alpha_i|$ between the analyzers in the signal and idler fields, which is typical of a quantum correlation.

Another type of phase plate which has been studied is a Heaviside phase plate, in which there is relative phase difference of π between the phase imparted by each section of the plate [212,210]. The transmission function is given by $T(\phi, \alpha) = 1 - 2[\Theta(\phi - \alpha) - \Theta(\phi - \alpha - \beta)]$, where Θ is the Heaviside step function, α is the orientation angle of the plate and β is the angular width of the π -step section. The simplest case corresponds to two half-circle sections ($\beta = \pi$). These step phase plates can also be used to probe multidimensional entanglement. Pors et al. have shown that the amount of usable entanglement that is available is given by the dimensionality of the measurement apparatus [210,211]. The authors have dubbed this the “Shannon dimensionality”, in analogy with the Shannon number of a classical communication channel [213]. The Shannon dimensionality is an effective Schmidt number, corresponding to the amount of entanglement which can be accessed by the measurement system. In the case of the phase plate analyzers, the dimensionality has a simple experimental interpretation. It is given by 2π divided by the area under the normalized coincidence curve, plotted as a function of the relative angle of the phase plates. Experimental and theoretical results show that the half-circle plate corresponds to dimensionality of three, while a quarter section plate gives dimensionality of six. The authors also considered step plates with multiple sections, and have shown that it should be possible to probe spaces with dimension on the order of about 50 [211].

There is thus an inconsistency between the amount of entanglement which is theoretically available and the amount of entanglement actually accessible in a given experimental scenario, due in particular to the geometry of the down-conversion setup and the spatial bandwidth of the optical systems used in manipulation and detection of the fields involved.

Another experiment investigating this kind of entanglement quantification, used entangled states prepared placing apertures in the path of the beams generated by SPDC. In this case the aperture photon path defines the qubit state. In Ref. [214], two double-slits placed at the path of the idler and signal photons were used to generate two-qubit entangled states. States with different degrees of entanglement were prepared by modifying the pump beam profile that generates the twin photons. Measurements of either two-photon conditional interference or marginal probabilities were used for characterizing entanglement in two-qubit spatial pure states.

The concurrence \mathcal{C} is an entanglement quantifier for bipartite systems [215]. For a general pure entangled state of two qubits,

$$|\psi\rangle = c_{11}|11\rangle + c_{10}|10\rangle + c_{01}|01\rangle + c_{00}|00\rangle, \quad (152)$$

the concurrence is given by

$$\mathcal{C}(\psi) = 2|c_{11}c_{00} - c_{10}c_{01}|. \quad (153)$$

State (152) may be written as a Schmidt decomposition [216]

$$|\psi\rangle = c'_{11}|11\rangle' + c'_{00}|00\rangle', \quad (154)$$

where $|ii\rangle'$ ($i = 0, 1$) is the *Schmidt basis*, and the coefficients c'_{ii} are real and positive. In terms of these coefficients, the concurrence is given by the simpler expression

$$\mathcal{C}(\psi) = 2c'_{11}c'_{00}. \quad (155)$$

In Ref. [214], states $|0\rangle, |1\rangle$ represent the single photons which pass through either slit of the double slit aperture. The strategy used for characterizing entanglement consists in performing measurements in the Schmidt basis, either by directly measuring the Schmidt coefficients or through a direct connection between concurrence, given by Eq. (155), and the visibility of interference patterns obtained when one of the detectors is used as trigger. The Schmidt basis is selected by letting the photons propagate through an appropriate lens system and keeping one of the detectors fixed at some specific positions, while the other is scanned at the Fourier plane of the lens. The Schmidt coefficients are then obtained from these conditional interference patterns. In the second method the fixed detector used as trigger is completely opened detecting all photons that crossed one of the double-slits while the second point detector is scanned at the lens Fourier plane. This corresponds to a measurement of the marginal probability, which is defined as the probability, $\bar{P}_1(x_i)$, of observing a photon idler at x_i and the signal at any location ($-\infty < x_s < +\infty$) [84] and is related to the concurrence as

$$P_1(x_i) \propto \left[1 + \sqrt{1 - [\mathcal{C}(\psi)]^2} \cos(\alpha x_i)\right]. \quad (156)$$

In Ref. [55] different two-qubit states are generated by using collinear type II SPDC and a double-slit. Different states are produced by tailoring the imaging system in between the two-photon source and the double slit. More than 30 different two-photon states are characterized by measuring their complete two-photon interference patterns in the far field of the double slit.

8.5. Hermite–Gaussian modes

The mode decomposition of the two-photon state produced in SPDC can also be performed using the Hermite–Gaussian modes, which are given by the complex field amplitude [170]

$$U_{nm}^{HG}(x, y, z) = c_{nm} \frac{1}{w(z)} H_n \left(\frac{\sqrt{2}x}{w(z)} \right) H_m \left(\frac{\sqrt{2}y}{w(z)} \right) \exp \left(-\frac{x^2 + y^2}{w(z)^2} \right)$$

$$\times \exp \left\{ -i \left[\frac{k(x^2 + y^2)}{2R(z)} - (n + m + 1)\gamma(z) \right] \right\}. \quad (157)$$

Here C_{nm} are the coefficients, $H_n(x)$ is the n th-order Hermite polynomial, which is an even or odd function of x if n is even or odd, respectively. The order \mathcal{N} of the beam is the sum of the indices: $\mathcal{N} = m + n$. The usual Gaussian beam is the zeroth-order U_{00}^{HG} beam. See plots of HG modes in Fig. 29(right).

8.6. Down-conversion with Hermite–Gaussian modes

Consider SPDC in which the pump beam is described by a HG mode U_{nm}^{HG} . The two-photon state can be expanded as [217,146]

$$|\psi_{nm}\rangle = \sum_{j,k,u,t=0}^{\infty} C_{jkut}^{nm} |v_{jk}\rangle |v_{ut}\rangle, \quad (158)$$

where $|v_{ab}\rangle$ are Hilbert space vectors such that $v_{ab}(\mathbf{q}) = \langle \mathbf{q} | v_{ab} \rangle$ corresponds to the HG mode written in k -vector space, given by the Fourier transform of Eq. (157). The coefficients C_{jkut}^{nm} are related to the pump beam and phase matching function through

$$C_{jkut}^{nm} = \iint d\mathbf{q}_u d\mathbf{q}_i v_{jk}^*(\mathbf{q}_s) v_{ut}^*(\mathbf{q}_i) \Phi_{nm}(\mathbf{q}_s, \mathbf{q}_i), \quad (159)$$

where $\Phi_{nm}(\mathbf{q}_s, \mathbf{q}_i)$ is given by the product of the angular spectrum for a HG pump beam and the phase matching function (see Section 3). An analytical expression for the coefficients C_{jkut}^{nm} was calculated in Ref. [217], showing that spatial parity is conserved in the x and y directions. That is, the indices $j + u$ ($k + t$) must have the same parity as the pump beam index n (m). Since the parity of each down-converted photon is undetermined, yet the sum of parities is well-defined, the two-photon state is entangled in parity. Thus, assuming that the pump beam has well-defined parity in the y direction, and ignoring the x direction, the two-photon state can be written as

$$|\psi\rangle_{\text{even}} = \frac{1}{\sqrt{2}} (|\psi_{EE}\rangle + |\psi_{OO}\rangle), \quad (160)$$

or

$$|\psi\rangle_{\text{odd}} = \frac{1}{\sqrt{2}} (|\psi_{EO}\rangle + |\psi_{OE}\rangle), \quad (161)$$

where E and O stand for the y indices of photons 1 or 2 being even (odd) and odd (even) numbers, respectively. If the pump beam is a HG mode, the states $|\psi_{XY}\rangle$ ($X, Y = E, O$) are given by linear combinations of modes with the same y parity. For example,

$$|\psi_{EO}\rangle = \sum_{k \text{ even}, t \text{ odd}} \sum_{j,u} C_{jkut}^{nm} |v_{jk}\rangle |v_{ut}\rangle, \quad (162)$$

and similarly for the other states in (160) and (161). Yarnall et al. [218,219] have used this type of parity entanglement to violate Bell's inequalities with parity measurements, which we describe in detail below in Section 8.7.

Using the expansion (158), the concurrence of the two-photon state can be calculated as a function of the pump beam profile and the length of the non-linear crystal. Numerical results reported in [146] show that in general the entanglement increases with the order $n + m$ of the pump beam.

8.7. Bell non-locality

The Einstein–Podolsky–Rosen paradox showed an inconsistency between local-realism and the completeness of quantum mechanics. In 1965, John S. Bell considered the predictions of local realism against those of quantum mechanics [220]. His argument, made in the context of David Bohm's version of the EPR paradox involving two entangled spin-1/2 systems [221], showed a conflict between the predictions of quantum mechanics and local realistic theories. This provided an experimentally accessible testing ground for these theories. The Clauser–Horne–Shimony–Holt inequality [222], also derived independently by Bell [223], shows that any local realistic theory should obey

$$S = |E(a, b) + E(a', b) + E(a, b') - E(a', b')| \leq 2, \quad (163)$$

where $-1 \leq E(a, b) \leq 1$ is the correlation function of dichotomic measurements a and b on systems A and B . For a pair of maximally-entangled spin- $\frac{1}{2}$ particles, quantum mechanics predicts $S_{\text{max}} = 2\sqrt{2}$. This set the stage for tests of quantum mechanics versus local realism beginning with the work of Freedman and Clauser [224] and Aspect and collaborators

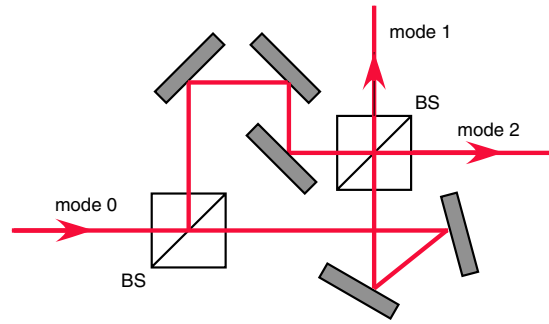


Fig. 32. Asymmetric interferometer used as a parity projector. When $\delta_1 = \delta_2$ and the beam splitters are 50:50, transverse modes with even parity leave the interferometer in port 1, and odd transverse modes in port 2.

[225,226]. With the advent of down-conversion sources, recent experiments have reached a considerable degree of sophistication, with the objective of performing a conclusive loop-hole free test [48,227,228], and also to discard more complex alternatives to standard quantum theory [229,230].

An early adaptation of the Bell inequality to continuous variables was provided by John Bell, who considered linear combinations of position and momentum observables of the form $\mathbf{x} + \alpha \mathbf{p}$, where α is a continuous parameter [223]. By binning the results, for instance into non-negative and negative values, one can translate these continuous measurements into two outcomes and apply the Bell–CHSH inequality (163). Bell reached a striking conclusion: quantum states with positive Wigner functions should allow for local realistic descriptions, since in this case the Wigner function itself serves as a classical probability distribution of the x and p variables [223]. A surprising example is the EPR state (128), with Wigner function given by [223]

$$W_{\text{EPR}}(x_1, p_1, x_2, p_2) = 2\pi \delta(x_1 - x_2) \delta(p_1 + p_2), \quad (164)$$

which is non-negative everywhere. This state displays an infinite amount of entanglement, and as such it is remarkable that it does not violate the Bell–CHSH inequality (163). The EPR state is not physical, however it represents the limit $a_-/a_+ \rightarrow 0$ (and $b_+ = b_- = 0$) of the Gaussian state (116).

Despite these arguments against the use of continuous variables in this context, it was later shown by Banaszek and Wódkiewicz [231,232] that the EPR state does violate the Bell–CHSH inequality when one considers measurements of the displaced parity operator. The parity operator does not have a well-behaved Wigner–Weyl representation, and thus expectation values of this operator do not correspond to averages over classical probability distributions. This point has been explored in more detail by Revzen et al. [233]. Thus, the state of a given system alone is not enough to determine whether it is suitable or not for a Bell-type experiment, but rather one must also take into account the observables measured.

Extending the idea of the parity operator, it is possible to define a set of pseudo-spin operators, forming an analogy with the Pauli operators for a spin-1/2 system. Chen et al. have shown that the operators [234]

$$\mathbf{X} = \sum_{n=0}^{\infty} |2n+1\rangle \langle 2n| + |2n\rangle \langle 2n+1| \quad (165a)$$

$$\mathbf{Y} = i \sum_{n=0}^{\infty} |2n+1\rangle \langle 2n| - |2n\rangle \langle 2n+1| \quad (165b)$$

$$\mathbf{Z} = \sum_{n=0}^{\infty} |2n\rangle \langle 2n| - |2n+1\rangle \langle 2n+1|, \quad (165c)$$

defined in terms of photon number Fock states $|n\rangle$, obey a $SU(2)$ algebra. One can recognize \mathbf{Z} as the parity operator. These operators were originally formulated for single-modes of the electromagnetic field, and their realization presents considerable experimental challenges [234].

An insightful contribution was made by Abouraddy et al., who recognized that the operators (165) could be constructed for the spatial degrees of freedom of photons [218]. This is possible due to the isomorphism between the photon number Fock states $|n\rangle$, and the spatial degrees of freedom of a field described by a one-dimensional Hermite Gaussian mode with index n [218]. To employ the full power of the analogy between the spatial version of the pseudo-operators (165) and the Pauli operators, one must be able to implement arbitrary rotations, composed of linear combinations of \mathbf{X} , \mathbf{Y} and \mathbf{Z} . In Ref. [218], the authors showed that arbitrary rotations of the “spatial parity”, can be manipulated through a series of linear optical components. This allows for the use of the spatial parity of single photons as a quantum bit in quantum information tasks [235]. For example, \mathbf{Z} can be implemented by a mirror reflection or a lens system. One can discriminate between even and odd spatial modes of a single photon by interfering the field with its mirror image [236]. This can be achieved using the asymmetric Mach-Zehnder interferometer shown in Fig. 32. Photons traveling through arm 1 of the

interferometer are subject to 2 mirror reflections, while photons in arm 2 are subject to 3 mirror reflections. Each reflection transforms the transverse wave vector as $(q_x, q_y) \rightarrow (q_x, -q_y)$. Assuming a single-photon detection at an exit port, the photon annihilation operators at the exit ports are related to the input port by

$$\mathbf{a}_1(\mathbf{q}) = t^2 e^{i\delta_1} \mathbf{a}_0(q_x, q_y) - r^2 e^{i\delta_2} \mathbf{a}_0(q_x, -q_y) \quad (166)$$

$$\mathbf{a}_2(\mathbf{q}) = itre^{i\delta_1} \mathbf{a}_0(q_x, -q_y) + itre^{i\delta_2} \mathbf{a}_0(q_x, q_y) \quad (167)$$

where t and r are the transmissivity and reflectivity of the beam splitters. δ_1 and δ_2 are phases due to propagation through arms 1 and 2. Assuming $|\delta_1 - \delta_2| \bmod 2\pi = 0$, and $t = r$, an even input mode will leave the interferometer in output 2 while an odd mode will exit in output 1. The asymmetric interferometer is thus capable of projecting onto even or odd modes, and is the spatial parity analog to the polarizing beam splitter [218].

To perform rotations in parity space, it is necessary to imprint a variable phase on half of the light beam. In Ref. [218] it was shown that this can be done using two phase plates. Each plate is placed in half of the input field, so that plate 1 covers the region $x < 0$ and imprints a phase $\exp(-i\theta/2)$, and plate 2 covers the region $x \geq 0$ and imprints a phase $\exp(i\theta/2)$. The parity rotation depends upon the overall phase difference between the two halves of the field.

Using a set of variable phase plates and asymmetric interferometers for each of the down-converted fields, Yarnall et al. violated Bell's Inequality in spatial parity space for pump beams with different spatial parity [219].

9. Applications to quantum information

The facility with which one can produce highly-entangled states from SPDC and manipulate the spatial characteristics of the pump and down-converted fields allows for the investigation of a wide range of quantum information applications and phenomena. A principal advantage of the spatial degrees of freedom of photons, as compared to the polarization degree of freedom, for example, is the high-dimensionality of the system. This allows for the generation of entangled continuous variable states or entangled d -dimensional *qudits*. Higher dimensional ($D > 2$) quantum systems have been shown to allow for higher security and transmission rates in quantum cryptography [237–239], increased security in two-party protocols such as bit commitment [240] and coin tossing [241,242], and more robust tests of Bell's inequalities [243]. In Sections 7 and 8 we showed that the two-photon quantum state produced by SPDC can be highly entangled. Furthermore, there exist schemes for engineering the two-photon entanglement by properly shaping the two-photon angular spectrum [16,244,245]. There is also a wide array of gadgetry devised to manipulate these spatial degrees of freedom, including lens systems [21,168,167,246], holographic masks [184,247], phase plates [209,210,219] and more recently the development of spatial light modulators have opened up even more possibilities for the synthesis and control of the spatial degrees of freedom of photons [248–251].

Orbital angular momentum is a natural choice for encoding single- and entangled qudits, and a number of proof of principle experiments have been performed which employ these degrees of freedom. These include the demonstration of bit commitment [252] and coin tossing protocols [176] with entangled qutrits ($D = 3$), manipulation of heralded qutrits [175], violation of Bell's inequality and entanglement concentration of entangled qutrits [173,174], violation of Bell's inequality in various two-dimensional subspaces of the infinite-dimensional OAM space [250] and quantum cryptography [253,254].

Higher-dimensional quantum information protocols can also be implemented using the linear transverse position and momentum. In this respect, entangled qudits have been produced using D -slit apertures [20,255], and by binning the near and far-field detection positions [256] and quantum cryptography with a 37-dimensional alphabet has been demonstrated [257].

Another notable use of spatial entanglement is the creation of multiply entangled states, which are entangled in multiple degrees of freedom [258,259]. In fact, pairs of photons which are *hyperentangled* (entangled in *all* degrees of freedom) have been produced and tomographically analyzed [260]. It has been shown theoretically [261–263] and experimentally [201,264,265], that entanglement in an auxiliary degree of freedom can improve Bell-state analysis of photon pairs. Barreiro, Wei and Kwiat have used auxiliary OAM entanglement to surpass the channel capacity imposed by linear optics in the quantum superdense coding protocol [265]. First-order transverse modes and polarization can be used to define single-photon logical qubits which are invariant under azimuthal coordinate rotations [266,267], and to implement small-scale quantum algorithms [268].

9.1. Generation of entangled qudits

There are a number of ways to generate entangled qudits using the spatial degrees of freedom of twin photons. A natural choice is using a set of transverse modes with discrete quantum numbers, such as the Hermite–Gaussian or Laguerre–Gaussian modes. A number of experiments in this direction have been performed [173–176,252].

Another possibility is through D -slit apertures placed in each down-converted field [255,20], as illustrated in Fig. 33. By focusing the pump beam in the plane of the apertures, one can guarantee that the photons always pass through

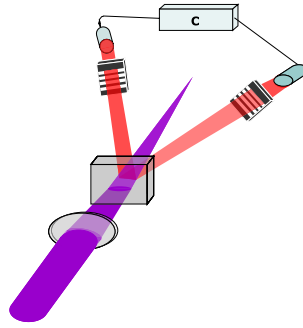


Fig. 33. Multiple-slit scheme used to produce entangled qudits.

symmetrically opposite slits of their respective apertures. In this fashion, the two-photon state immediately after the apertures can be written as [20,255]:

$$|\psi\rangle = \frac{1}{\sqrt{D}} \sum_{j=(1-D)/2}^{(D-1)/2} \exp(ikd^2j^2/2z) |j\rangle_1 | -j\rangle_2, \quad (168)$$

where d is the distance between the slits, z is the distance from crystal to slits, k is the wave number and $|j\rangle$ are states describing the spatial profile of a single photon which has passed through slit j , which are given by

$$|j\rangle = \int d\rho R(\rho - jd) |\rho\rangle. \quad (169)$$

Here $R(\rho)$ are the aperture functions describing each individual slit. The position correlation of these photons as well as the entanglement can be confirmed by measuring in the near-field and far-field of the apertures, respectively. In Ref. [251], it was demonstrated that different spatial qudit states can be generated by sending one of the down-converted beams through diffractive apertures with controllable transmission coefficients, produced with a spatial light modulator.

Another technique for generating spatial qudits is by simply defining a discrete array of spatial regions. This has been realized in the single-photon regime [257] for dimension $D = 37$ and entangled-photon regime for up to $D = 6$ [256]. Using lens systems, it is possible to create and measure superposition states [269].

Possible applications of two entangled qudits in quantum communication rely on the ability of transmitting these photonic high dimension entangled states between different communicating parties. The propagation of entangled states of qubits have been subject of recent studies. Optical-fibers links were used to send energy-time entangled qubits for receivers separated by more than 10 km [270] and a test of the Bell inequality [220] showed that the two-photon state was still in an entangled state. Free-space distribution of polarization entangled qubits through the atmosphere was demonstrated for a distance of 144 km [271]. The experimental free-space propagation of two entangled four-dimensional qudits or “ququarts” produced by four-slit apertures was reported in Ref. [272]. Free space propagation of the entangled photons was performed on a laboratory scale. The spatial correlation of the propagated state was observed at the image plane of two lenses and high-fidelity with its original form was measured. Far from the image plane a conditional interference pattern of the propagated state was measured. The presence of the conditional interference pattern shows that the state of the propagated ququarts is entangled [20]. Several studies of free space propagation of single and biphoton fields with OAM have been performed, and are mentioned in more detail in Section 9.2.

An important step in future use of entangled spatial qudits is the development of quantum tomography suitable for this degree of freedom or a method for the determination of the density matrix of the compound system. In Refs. [273,274] a technique for determination of the density operator was developed for the case of two spatial qubits, generated with two double-slits placed in the path of the photon pair. Measurements were performed at the image plane and in the focal plane of a lens for different positions of the detector in the transverse plane. This method can be used for the tomography of two spatial qubits in a mixed state [275]. In a second method, the interference patterns obtained at the intermediate plane between the image and the focal plane are used for reconstruction of the quantum state of two spatial qubits [276] and qutrits [277].

9.2. Quantum cryptography

An interesting application for spatial qudits is quantum key distribution, in which the increased dimensionality presents benefits not only in terms of the information transmission rate but also the security of the protocol. It is straightforward to generalize the well-known BB84 [278] or BBM [279] protocols to qudits [237–239]. In this case, it is possible in principle to send on average $\log_2 D$ bits per sifted qudit, while an eavesdropper employing an intercept-resend strategy would induce a qudit error rate of $E_D = \frac{1}{2} \frac{D-1}{D}$, which saturates at $1/2$ for large D . The increased security is due to the increased disturbance,

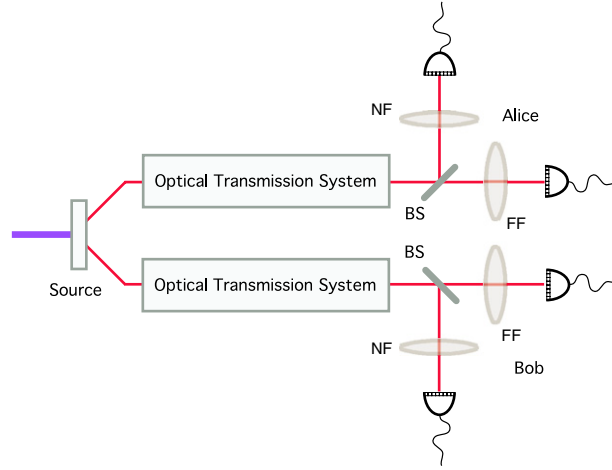


Fig. 34. Quantum key distribution using transverse position and momentum of entangled photons. Photons are sent to Alice and Bob's input planes via optical transmission systems. The random basis selection can be performed using beam splitters (BS).

since half the time the eavesdropper measures in the wrong basis, and consequently sends the wrong state with a probability of $(D - 1)/D$.

One can achieve the advantages mentioned above using discrete sets of transverse modes or employing the continuous position and momentum correlations present in the down-converted photons. For discrete modes, the quantum cryptography protocol and theoretical security analysis should be nearly identical to the general cases of qudits covered in Refs. [237,238]. Theoretical proposals and experimental investigations in this direction have focused primarily on the orbital angular momentum degree of freedom [280,253,254].

The conjugate position and momentum correlations provide an interesting scenario from a practical point of view and in addition to the advantages mentioned above, have been shown to present particular security features. Fig. 34 shows an illustration of the main idea. Alice and Bob receive spatially entangled photon pairs. Independently, they choose randomly between two conjugate bases: the near field variable ρ and far-field variable q . The random selection can be performed passively using a 50:50 beam splitter. Using optical lens systems (represented by lenses NF and FF), they map the near and far-field distributions onto their respective detection planes. Using an array of single-photon detectors, they register the detection position, and thus infer the variable ρ or q . Several experimental investigations of this scheme have been performed in the case of entangled photons [281] and single photons [257].

A first motivation for the study of spatial QKD is the increased information transmission rate per photon pair. In the case that Alice and Bob measure in the ρ basis, the secret key rate ΔI_ρ is given by the difference between Alice–Bob and Alice–Eve mutual information: [282,283]

$$\Delta I_\rho = I(\rho_A|\rho_B) - I(\rho_A, E), \quad (170)$$

where the mutual information is given by

$$I(\mathbf{x}_1, \mathbf{x}_2) = H(\mathbf{x}_1) - H(\mathbf{x}_1|\mathbf{x}_2), \quad (171)$$

and

$$H(\mathbf{x}) = - \int d\mathbf{x} P(\mathbf{x}) \ln P(\mathbf{x}), \quad (172)$$

$$H(\mathbf{x}_1|\mathbf{x}_2) = - \iint d\mathbf{x}_1 d\mathbf{x}_2 P(\mathbf{x}_1, \mathbf{x}_2) \ln P(\mathbf{x}_1|\mathbf{x}_2), \quad (173)$$

are the entropy and conditional entropy respectively, for a continuous distribution [213,284]. $P(\mathbf{x})$ is the probability distribution for \mathbf{x} , $P(\mathbf{x}_1, \mathbf{x}_2)$ is the joint probability distribution for $\mathbf{x}_1, \mathbf{x}_2$ and $P(\mathbf{x}_1|\mathbf{x}_2)$ is the conditional probability distribution for \mathbf{x}_1 conditioned on measurement of \mathbf{x}_2 . A similar expression can be written for the secret key rate ΔI_q corresponding to q measurements. Here E stands for the Eve's measurement, and we are considering the case of forward reconciliation [282]. Using the above equations, the key rate can be put in the form

$$\Delta I_\rho = H(\rho_A|\rho_B) - H(\rho_A|E), \quad (174)$$

and similarly for ΔI_q . For individual attacks, one can consider that Alice, Bob and Eve share a pure state [282]. Thus, upon measurement, Bob and Eve prepare Alice's photon in some state, which must satisfy the entropic uncertainty relation [285]:

$$H(\rho_A|E) + H(q_A|q_B) \geq \ln \pi e. \quad (175)$$

To establish a secret key requires $\Delta I \geq 0$. This leads to [282]

$$\Delta I \geq \ln \pi e - H(\mathbf{q}_A|\mathbf{q}_B) - H(\mathbf{p}_A|\mathbf{p}_B) \geq 0. \quad (176)$$

For any distribution with variance σ^2 , the entropy satisfies $H \leq \ln \sqrt{2\pi e \sigma^2}$ [213,284]. Thus, the key rate can be bounded by [283]

$$\Delta I \geq -\ln 2 \Delta(\mathbf{q}_A|\mathbf{q}_B) \Delta(\mathbf{p}_A|\mathbf{p}_B), \quad (177)$$

where $\Delta(\mathbf{x}|\mathbf{y})$ is the variance of the distribution of \mathbf{x} given a measurement of \mathbf{y} .

This condition is fulfilled when $\Delta(\mathbf{q}_A|\mathbf{q}_B)\Delta(\mathbf{p}_A|\mathbf{p}_B) \leq 1/2$, which is equivalent to the EPR variance criterion (112). For photons produced by SPDC, the EPR criteria depends on the characteristics of the pump beam and the length of the non-linear crystal L .

Implementation of QKD requires preservation of quantum information over long transmission distances, and as such is a technical challenge. QKD with spatial variables should be most aptly suited to a free-space transmission, as opposed to optical fibers, due to the multi-mode character of the down-converted fields. There are at least two main factors which limit the distance at which spatial QKD could be a viable endeavor. The first are fluctuations in the index of refraction along the free-space transmission path. This causes local phase fluctuations which distort the single-photon fields, increasing the error rate. Atmospheric turbulence causes fluctuations in the index of refraction which transform an initial field $\psi(\mathbf{r}) \rightarrow \exp[i\delta(\mathbf{r})]\psi(\mathbf{r})$, where the position-dependent phase $\delta(\mathbf{r})$ describes the phase fluctuations in the wave function. The transmission of spatial quantum information under these conditions has been considered in Refs. [286,287] in the case of Laguerre–Gaussian modes and in Ref. [269] for single-photon spatial QKD. Assuming that the phase fluctuations are isotropic and a random Gaussian process, the induced error rate is dependent upon the initial field and the length scale of the phase fluctuations known as the Fried parameter [288,286]. Typical values of the Fried parameter are 10–60 cm [289]. For realistic experimental parameters, it was shown in Ref. [269] that spatial QKD should be feasible up to a few kilometers. It is important to note that the recent progress in the field of classical optical communication has shown that it should be possible to correct the effects of turbulence in real time with adaptive optics and a reference beam [289–291]. A recent experiment by Pors et al. has shown that OAM entanglement should resist typical atmospheric turbulence for up to a few kilometers [292].

The second limiting factor is the presence of losses due to absorption, which reduces the transmission rate as well as the signal to noise ratio, which Eve can exploit to her advantage. The noise present in spatial QKD comes from spurious ambient photons and detector dark counts. Following Zhang et al. [283], three types of events can contribute to the coincidence count rate, occurring with probabilities $P(\text{spdc}, \text{spdc})$, $P(\text{noise}, \text{spdc})$ or $P(\text{spdc}, \text{noise})$, and $P(\text{noise}, \text{noise})$. Focusing only on dark counts, they show that for reasonable experimental parameters, one can tolerate losses of a few dB and still satisfy Eq. (177). This level of loss corresponds to free-space transmission distances on the order of a few km. However, it is important to note that the left-side of inequality (177) is an upper-bound which is saturated only when Alice and Bob's coincidence distributions are Gaussian. However, assuming a constant dark count rate for each detector, the coincidence counts in the presence of loss will be composed of a Gaussian distribution of correlated photons, combined with a *constant* background count, resulting in a non-Gaussian distribution. The interesting eavesdropping strategy for Eve is to perform measurements so that she can mask her disturbance with the counts due to noise, so that, in this case, her disturbance should appear as a constant background noise. This can be achieved with a simple intercept resend strategy, so that when she measures in the same basis as Alice and Bob, she goes undetected. Zhang et al. [283] have shown that considering the non-Gaussian nature of the total coincidence distribution allows one to increase the allowable losses by at least a factor of ten, giving a secure transmission distance of several tens of kilometers. Thus, in a realistic scenario, the noise due to dark counts can increase the allowable losses, while maintaining security of the protocol.

9.3. Quantum teleportation

Quantum teleportation is a method to transfer quantum information between distant locations, without direct transmission of the physical system containing the information. The original quantum teleportation proposal [293] considered discrete D -level ($D = 2$) systems. Further proposals generalized it to continuous variables [294–296]. Quantum teleportation plays an important role in quantum information processing since it is the basis for quantum repeaters [297], non-local interactions between light and matter [298], as well as linear optics quantum computing [299].

A quantum teleportation protocol which uses transverse spatial properties of intense light fields has also been proposed [300,301], and a teleportation procedure which can transmit the angular spectrum of a single-photon has been proposed in Ref. [302].

We will describe the teleportation procedure of Ref. [302] in more detail. Fig. 35 illustrates the main idea. Alice is in possession of a single photon described by the quantum state

$$|\phi\rangle_1 = \int d\mathbf{q} u(\mathbf{q}) |\mathbf{q}\rangle_1, \quad (178)$$

where $u(\mathbf{q})$ is the normalized angular spectrum of the field in the $z = 0$ plane. She would like to send the angular spectrum $u(\mathbf{q})$ of the single-photon field to Bob. To do this, Alice and Bob share a pair of spatially entangled photons described by the

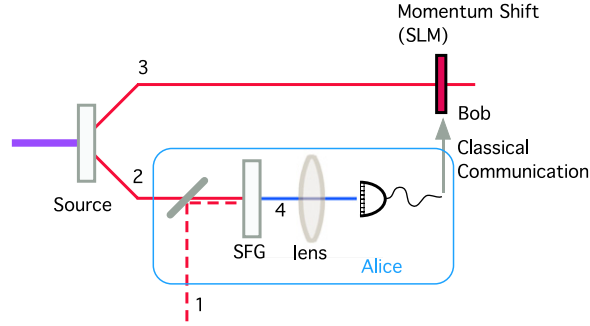


Fig. 35. Illustration of teleportation of the spatial degrees of freedom of a single photon. A nonlinear crystal is used to perform second harmonic generation (SHG). Bob's momentum shift can be performed using spatial light modulation (SLM).

quantum state

$$|\psi_{AB}\rangle \propto \int \int d\mathbf{q}_i d\mathbf{q}_s v(\mathbf{q}_i + \mathbf{q}_s) \gamma(\mathbf{q}_i - \mathbf{q}_s), \quad (179)$$

where v is the angular spectrum of the laser and γ is the phase matching function defined in Eq. (59). Assuming that Alice is in possession of fields 1 and 2 and Bob of field 3, she follows the usual recipe for quantum teleportation [293]. First, it is necessary for Alice to perform a joint measurement on her fields, and send the measurement result to Bob using classical communication. Depending on the outcome, Bob performs a unitary operation on his field, and then recovers the initial quantum state of field 1.

Alice can perform the joint measurement on the spatial degrees of freedom of photons 1 and 2 by injecting them into a nonlinear up-conversion crystal cut for second harmonic generation (SHG) or sum frequency generation. The full multimode Hamiltonian operator for SHG has been described in Ref. [303], and in the thin-crystal limit can be written as

$$\mathbf{H} \propto \int \int \int d\mathbf{q} d\mathbf{q}' d\mathbf{q}'' \delta^2(\mathbf{q} + \mathbf{q}' - \mathbf{q}'') \mathbf{a}_1(\mathbf{q}) \mathbf{a}_2(\mathbf{q}') \mathbf{a}_4^\dagger(\mathbf{q}'') + H.c. \quad (180)$$

Index 4 denotes the second-harmonic field, which is assumed to be initially in the vacuum state. After the nonlinear interaction, Alice measures the transverse wave vector \mathbf{q}'' of the up-converted field, and sends the measurement result to Bob. The detection position is sent to Bob by a classical communication channel, as shown in Fig. 35. The paraxial field operator which describes photodetection at position ρ_D in the far-field is given by Eq. (108). Applying this operator to the state at the output of the beam splitter, detection of a photon at the position ρ_D selects the state

$$|\psi_f\rangle \propto \int \int d\mathbf{q} d\mathbf{q}' u(\mathbf{q}) \Phi\left(\frac{\kappa}{f} \rho_D - \mathbf{q}, \mathbf{q}'\right) |\mathbf{q}'\rangle_3, \quad (181)$$

where all modes in the vacuum state have been excluded, κ is the wave number of the SHG field, f is the focal length of the lens, and Φ is the two-photon angular spectrum defined in Eq. (57).

In the limiting case of an EPR-like state, in which the angular spectrum of the SPDC pump field is a plane wave, $v(\mathbf{q}) \propto \delta(\mathbf{q})$, and the phase matching function is very broad, so that it is reasonable to approximate $\gamma(\mathbf{q}) \propto 1$. This is the thin crystal approximation described in Section 3.4. Under these conditions the state teleported to Bob (181) is

$$|\psi_f^{EPR}\rangle = \int d\mathbf{q} u\left(\mathbf{q} + \frac{\kappa}{f} \rho_D\right) |\mathbf{q}\rangle_3, \quad (182)$$

which is equivalent to the original state (178) except for a translation in \mathbf{q} . Applying a momentum translation:

$$\mathbf{P}(\alpha) |\mathbf{q}\rangle = |\mathbf{q} + \alpha\rangle, \quad (183)$$

Bob will then have $\mathbf{P}(\kappa \rho_D / f) |\psi_f^{EPR}\rangle = |\phi\rangle_3$, which corresponds to perfect teleportation of the initial state $|\phi\rangle_1$. The momentum translation can be implemented using a spatial light modulator.

In a more general case where γ cannot be approximated by unity, the final state after momentum translation is

$$|\psi_f\rangle = C \int \int d\mathbf{q} d\mathbf{q}' u(\mathbf{q}) v(\mathbf{q}' - \mathbf{q}) \gamma\left(2\frac{\kappa}{f} \rho_D - \mathbf{q}' - \mathbf{q}\right) |\mathbf{q}'\rangle_3, \quad (184)$$

where C is a normalization constant. Assuming that Alice detects a photon in beam 4, the fidelity measures the success of the teleportation protocol [202], and is defined as $\mathcal{F} = |\langle \phi | \psi_f \rangle|$. The fidelity depends on the format of the angular spectrum $v(\mathbf{q})$ and phase matching function $\gamma(\mathbf{q})$, respectively.

This teleportation procedure has not yet been realized experimentally, and prevents several serious technical challenges. The principal obstacle is the low up-conversion efficiency for single-photon fields. New materials, such as periodically-poled

crystals [304] or photonic crystal structures may improve these conversion rates. In spite of the low conversion efficiency, a similar experiment using pairs of non-linear crystals to implement a complete Bell-state measurement in the polarization degree of freedom has been performed [305].

The same scheme can be used to swap entanglement between spatially entangled photons pairs, which would be necessary for long-distance spatial quantum communication using a large portion of the available Hilbert space. Another application of this teleportation procedure is the frequency tuning of one photon of a spatially entangled pair. This can be done by replacing photon 1 with an intense field, increasing the up-conversion rate. Frequency tuning of entangled photons has been realized using a periodically-poled crystal [304].

10. Conclusion

Parametric down-conversion has definitely played a very important role in the development of Quantum Optics and more recently Quantum Information. This review focused on the spatial degrees of freedom of the down-converted fields, which have been an important ingredient. The quantum correlations between down-converted photons have allowed for the production of quantum states of light, leading to the observation of non-classical effects and the study of entangled states and their application in Quantum Information tasks. Initially, the concept of spatial coherence in Optics was generalized to include two-photon coherence. Counter-intuitive aspects of the quantum world have been experimentally observed with the transverse spatial degrees of freedom, such as the measurement of the De Broglie wavelength of a two-photon wave packet, the anti-bunching of photon pairs, conditional two-photon interference patterns, quantum erasure, ghost images and ghost interference. These investigations have led to a considerable conceptual improvement and a real advance in the knowledge of the quantum world through the study of the spatial correlations in parametric down-conversion. Applications immediately arose from these new concepts, such as quantum lithography and metrology, quantum cryptography schemes, quantum teleportation and spatial qubits for quantum computation.

This field is still very active and contributions in the fundamental and applied domains appear regularly in the literature. Among the most promising research in the field, we would like to mention the study of the transverse correlations as a resource for quantum information in the domain of continuous variables and high dimension discrete states. Transverse spatial variables are natural entangled continuous variables that can be prepared in a vast range of entangled states whose properties and applications are just beginning to be explored.

Acknowledgements

The authors acknowledge financial support from the Brazilian funding agencies CNPq, CAPES, PRONEX, FAPEMIG and FAPERJ. This work was performed as part of the Brazilian National Institute of Science and Technology for Quantum Information.

References

- [1] D. Burnham, D. Weinberg, *Phys. Rev. Lett.* 25 (1970) 84.
- [2] B. Zeldovich, D.N. Klyshko, *JETP Lett.* - USSR 9 (1969) 40.
- [3] D.N. Klyshko, D. Krindach, *Opt. Spectrosc.* - USSR 26 (1969) 532.
- [4] S. Friberg, C.K. Hong, L. Mandel, *Phys. Rev. Lett.* 54 (1985) 2011.
- [5] C.K. Hong, L. Mandel, *Phys. Rev. A* 31 (1985) 2409.
- [6] C.K. Hong, L. Mandel, *Phys. Rev. Lett.* 56 (1986) 58.
- [7] R. Ghosh, L. Mandel, *Phys. Rev. Lett.* 59 (1987) 1903.
- [8] Z.Y. Ou, L. Mandel, *Phys. Rev. Lett.* 61 (1988) 54.
- [9] X.Y. Zou, L.J. Wang, L. Mandel, *Opt. Commun.* 84 (1991) 351.
- [10] T.P. Grayson, G.A. Barbosa, *Phys. Rev. A* 49 (1994) 2948.
- [11] X.Y. Zou, L.J. Wang, L. Mandel, *Phys. Rev. Lett.* 67 (1991) 318.
- [12] A. Joobeur, B.E.A. Saleh, M.C. Teich, *Phys. Rev. A* 50 (1994) 3349.
- [13] P.H.S. Ribeiro, S. Pádua, J.C.M. da Silva, G.A. Barbosa, *Phys. Rev. A* 49 (1994) 4176.
- [14] D.V. Strekalov, A.V. Sergienko, D.N. Klyshko, Y.H. Shih, *Phys. Rev. Lett.* 74 (1995) 3600.
- [15] T.B. Pittman, Y.H. Shih, D.V. Strekalov, A.V. Sergienko, *Phys. Rev. A* 52 (1995) R3429.
- [16] C.H. Monken, P.S. Ribeiro, S. Pádua, *Phys. Rev. A* 57 (1998) 3123.
- [17] E.J.S. Fonseca, C.H. Monken, S. Pádua, *Phys. Rev. Lett.* 82 (1999) 2868.
- [18] W.A.T. Nogueira, S.P. Walborn, S. Pádua, C.H. Monken, *Phys. Rev. Lett.* 86 (2001) 4009.
- [19] W.A.T. Nogueira, S.P. Walborn, S. Pádua, C.H. Monken, *Phys. Rev. A* 66 (2002) 053810.
- [20] L. Neves, G. Lima, J.G.A. Gómez, C.H. Monken, C. Saavedra, S. Pádua, *Phys. Rev. Lett.* 94 (2005) 100501.
- [21] J.C. Howell, R.S. Bennink, S.J. Bentley, R.W. Boyd, *Phys. Rev. Lett.* 92 (2004) 210403.
- [22] M. D'Angelo, Y.-H. Kim, S.P. Kulik, Y. Shih, *Phys. Rev. Lett.* 92 (2004) 233601.
- [23] D.N. Klyshko, *JETP* 28 (1969) 522.
- [24] L. Wang, Ph.D. thesis, University of Rochester, 1992.
- [25] D.N. Klyshko, *Photons and Non-Linear Optics*, Gordon and Breach Science Publishers, New York, 1988.
- [26] L. Mandel, E. Wolf, *Optical Coherence and Quantum Optics*, Cambridge University Press, New York, 1995.
- [27] Z.Y.J. Ou, *Multi-Photon Quantum Interference*, Springer, New York, 2007.
- [28] N. Bloembergen, *Nonlinear Optics*, Pearson Addison Wesley, New York, 1977.
- [29] Y.R. Shen, *Principles of Nonlinear Optics*, Wiley-Interscience, New York, 1984.
- [30] R. Boyd, *Nonlinear Optics*, Academic Press, New York, 1992.
- [31] E. Wolf, *Introduction to the Theory of Coherence and Polarization of Light*, Cambridge University Press, Cambridge, 2007.

- [32] M. Born, E. Wolf, *Principles of Optics: Electromagnetic Theory of Propagation, Interference and Diffraction of Light*, Cambridge University Press, New York, 1999.
- [33] P.H.S. Ribeiro, C.H. Monken, G.A. Barbosa, *Appl. Opt.* 33 (1994) 352.
- [34] E.J.S. Fonseca, G.A. Barbosa, C.H. Monken, S. Pádua, *Phys. Rev. A* 59 (1999) 1608.
- [35] B.E.A. Saleh, M.C. Teich, *Fundamentals of Photonics*, John Wiley and Sons, Hoboken, 2007.
- [36] J.W. Goodman, *Introduction to Fourier Optics*, Mc Graw Hill, Boston, 1996.
- [37] H. Bacry, M. Cadilhac, *Phys. Rev. A* 23 (1981) 2533.
- [38] D. Stoler, *J. Opt. Soc. Am.* 71 (1981) 334.
- [39] D. Marcuse, *Light Transmission Optics*, Van Nostrand Reinhold Company, New York, 1982.
- [40] M.H. Rubin, D.N. Klyshko, Y.H. Shih, A.V. Sergienko, *Phys. Rev. A* 50 (1994) 5122.
- [41] M.H. Rubin, *Phys. Rev. A* 54 (1996) 5349.
- [42] M. Atatüre, G.D. Giuseppe, M.D. Shaw, A.V. Sergienko, B.E.A. Saleh, M.C. Teich, *Phys. Rev. A* 66 (2002) 023822.
- [43] J.P. Torres, G. Molina-Terriza, L. Torner, *J. Opt. B* 7 (2005) 235.
- [44] M.V. Fedorov, M.A. Efremov, P.A. Volkov, E.V. Moreva, S.S. Straupe, S.P. Kulik, *Phys. Rev. Lett.* 99 (2007) 063901.
- [45] G. Molina-Terriza, J.P. Torres, L. Torner, *Opt. Commun.* 228 (2003) 155.
- [46] C.H. Monken, Angular spectrum transfer and transverse correlations in parametric down conversion (1998–2002), unpublished lecture notes.
- [47] G. Molina-Terriza, S. Minardi, Y. Deyanova, C.I. Osorio, M. Hendrych, J.P. Torres, *Phys. Rev. A* 72 (2005) 065802.
- [48] P.G. Kwiat, K. Mattle, H. Weinfurter, A. Zeilinger, A.V. Sergienko, Y. Shih, *Phys. Rev. Lett.* 75 (1995) 4337.
- [49] T.B. Pittman, D.V. Strekalov, D.N. Klyshko, M.H. Rubin, A.V. Sergienko, Y.H. Shih, *Phys. Rev. A* 53 (1996) 2804.
- [50] A.V. Burlakov, M.V. Chekhova, D.N. Klyshko, S.P. Kulik, A.N. Penin, Y.H. Shih, D.V. Strekalov, *Phys. Rev. A* 56 (1997) 3214.
- [51] E.J.S. Fonseca, P.H.S. Ribeiro, S. Pádua, C.H. Monken, *Phys. Rev. A* 60 (1999) 1530.
- [52] E.J.S. Fonseca, J.C.M. da Silva, C.H. Monken, S. Pádua, *Phys. Rev. A* 61 (2000) 023801.
- [53] Y.-H. Kim, S. Kulik, Y. Shih, M. Scully, *Phys. Rev. Lett.* 84 (2000) 1.
- [54] S.P. Walborn, M.O.T. Cunha, S. Pádua, C.H. Monken, *Phys. Rev. A* 65 (2002) 0338.
- [55] W.H. Peeters, J.J. Renema, M.P. van Exter, *Phys. Rev. A* 79 (2009) 043817.
- [56] P.H.S. Ribeiro, G.A. Barbosa, *Phys. Rev. A* 54 (1996) 3489.
- [57] A.V. Belinskii, D.N. Klyshko, *JETP* 78 (1994) 259.
- [58] J. Jacobson, G. Björk, I. Chuang, Y. Yamamoto, *Phys. Rev. Lett.* 74 (1995) 4835.
- [59] D.F. Walls, *Amer. J. Phys.* 45 (1977) 952.
- [60] E.J.S. Fonseca, Z. Paulini, P. Nussenzveig, C.H. Monken, S. Pádua, *Phys. Rev. A* 63 (2001) 043819.
- [61] P.H.S. Ribeiro, *Braz. J. Phys.* 31 (2001) 478.
- [62] K. Edamatsu, R. Shimizu, T. Itoh, *Phys. Rev. Lett.* 89 (2002) 213601.
- [63] P. Walther, J.-W. Pan, M. Aspelmeyer, R. Ursin, S. Gasparoni, A. Zeilinger, *Nature* 429 (2004) 158.
- [64] I. Vidal, S.B. Cavalcanti, E.J.S. Fonseca, J.M. Hickmann, *Phys. Rev. A* 78 (2008) 033829.
- [65] K.-H. Luo, J. Wen, X.-H. Chen, Q. Liu, M. Xiao, L.-A. Wu, *Phys. Rev. A* 80 (2009) 043820.
- [66] E. Yablonovitch, R.B. Vrijen, *Opt. Eng.* 38 (1999) 334.
- [67] A.N. Boto, P. Kok, D.S. Abrams, S.L. Braunstein, C.P. Williams, J.P. Dowling, *Phys. Rev. Lett.* 85 (2000) 2733.
- [68] P. Kok, A.N. Boto, D.S. Abrams, C.P. Williams, S.L. Braunstein, J.P. Dowling, *Phys. Rev. A* 63 (2001) 063407.
- [69] M. D'Angelo, M.V. Chekhova, Y. Shih, *Phys. Rev. Lett.* 87 (2001) 013602.
- [70] K. Wang, D.-Z. Cao, *Phys. Rev. A* 70 (2004) 041801.
- [71] P.R. Hemmer, A. Muthukrishnan, M.O. Scully, M.S. Zubairy, *Phys. Rev. Lett.* 96 (2006) 163603.
- [72] Q. Sun, P.R. Hemmer, M.S. Zubairy, *Phys. Rev. A* 75 (2007) 065803.
- [73] A. Pe'er, B. Dayan, M. Vucelja, Y. Silberberg, A. Friesem, *Opt. Exp.* 12 (2004) 6600.
- [74] R.W. Boyd, S.J. Bentley, *J. Mod. Opt.* 53 (2006) 713.
- [75] M. Tsang, *Phys. Rev. A* 75 (2007) 043813.
- [76] M.O. Scully, K. Drühl, *Phys. Rev. A* 25 (1982) 2208.
- [77] M.O. Scully, B.G. Englert, H. Walther, *Nature* 351 (1991) 111.
- [78] R. Feynman, R. Leighton, M. Sands, *The Feynman Lectures on Physics*, vol. III, Addison-Wesley, Reading, 1965.
- [79] S.P. Walborn, M.O.T. Cunha, S. Pádua, C.H. Monken, *Am. Sci.* 91 (2003) 336.
- [80] I.F. Santos, M.A. Sogioro, C.H. Monken, S. Pádua, *Phys. Rev. A* 67 (2003) 033812.
- [81] I.F. Santos, L. Neves, G. Lima, C.H. Monken, S. Pádua, *Phys. Rev. A* 72 (2005) 033802.
- [82] I.F. Santos, J.G. Aguirre-Gómez, S. Pádua, *Phys. Rev. A* 77 (2008) 043832.
- [83] V. Giovannetti, S. Lloyd, L. Maccone, J.H. Shapiro, *Phys. Rev. A* 79 (2009) 013827.
- [84] A.F. Abouraddy, B.E.A. Saleh, A.V. Sergienko, M.C. Teich, *Phys. Rev. Lett.* 87 (2001) 123602.
- [85] R.S. Bennink, S.J. Bentley, R.W. Boyd, *Phys. Rev. Lett.* 89 (2002) 113601.
- [86] R.S. Bennink, S.J. Bentley, R.W. Boyd, J.C. Howell, *Phys. Rev. Lett.* 92 (2004) 033601.
- [87] A. Gatti, E. Brambilla, M. Bache, L.A. Lugiato, *Phys. Rev. Lett.* 93 (2004) 093602.
- [88] A. Gatti, E. Brambilla, M. Bache, L.A. Lugiato, *Phys. Rev. A* 70 (2004) 013802.
- [89] F. Ferri, D. Magatti, A. Gatti, M. Bache, E. Brambilla, L.A. Lugiato, *Phys. Rev. Lett.* 94 (2005) 183602.
- [90] A. Valencia, G. Scarcelli, M. D'Angelo, Y. Shih, *Phys. Rev. Lett.* 94 (2005) 063601.
- [91] R. Hanbury-Brown, R.Q. Twiss, *Nature* 178 (1956) 1046.
- [92] B.I. Erkmen, J.H. Shapiro, *Phys. Rev. A* 79 (2009) 023833.
- [93] S.-H. Tan, B.I. Erkmen, V. Giovannetti, S. Guha, S. Lloyd, L. Maccone, S. Pirandola, J.H. Shapiro, *Phys. Rev. Lett.* 101 (2008) 253601.
- [94] B.I. Erkmen, J.H. Shapiro, *Phys. Rev. A* 77 (2008) 043809.
- [95] B.I. Erkmen, J.H. Shapiro, *Phys. Rev. A* 78 (2008) 023835.
- [96] A.F. Abouraddy, P.R. Stone, A.V. Sergienko, B.E.A. Saleh, M.C. Teich, *Phys. Rev. Lett.* 93 (2004) 213903.
- [97] M. Bache, D. Magatti, F. Ferri, A. Gatti, E. Brambilla, L.A. Lugiato, *Phys. Rev. A* 73 (2006) 053802.
- [98] M.C. Teich, B.E.A. Saleh, Entangled-photon microscopy, spectroscopy, and display, US patent no. 5,796,477, 1998.
- [99] M.V. Klein, T.E. Furtak, *Optics*, Wiley, New York, 1986.
- [100] H.J. Kimble, M. Degenais, L. Mandel, *Phys. Rev. Lett.* 39 (1977) 691.
- [101] D. Greenberger, M. Horne, A. Zeilinger, *Phys. Today* 46 (1993) 22–29.
- [102] P.H.S. Ribeiro, S. Pádua, J.C.M. da Silva, G.A. Barbosa, *Phys. Rev. A* 51 (1995) 1631.
- [103] C.K. Hong, T.G. Noh, *J. Opt. Soc. Am. B* 15 (1998) 1192.
- [104] D.G.M. Horne, A. Zeilinger, *World Scientific*, Singapore, 1994, p. 194.
- [105] M. Horne, *Kluwer*, Dordrecht, 1998, vol. 1, p. 109.
- [106] D.M. Greenberger, O.W. Greenberg, T.V. Greenbergest, *World Scientific*, Singapore, 1995, p. 233.
- [107] M.A. Horne, A. Shimony, A. Zeilinger, *Phys. Rev. Lett.* 62 (1989) 2209.
- [108] G. Jaeger, A. Shimony, L. Vaidman, *Phys. Rev. A* 51 (1995) 54.
- [109] G. Jaeger, M.A. Horne, A. Shimony, *Phys. Rev. A* 48 (1993) 1023.
- [110] A.F. Abouraddy, M.B. Nasr, B.E.A. Saleh, A.V. Sergienko, M.C. Teich, *Phys. Rev. A* 63 (2001) 063803.
- [111] B.E.A. Saleh, A.F. Abouraddy, A.V. Sergienko, M.C. Teich, *Phys. Rev. A* 62 (2000) 043816.

- [112] D.P. Caetano, P.H.S. Ribeiro, Phys. Rev. A 68 (2003) 043806.
- [113] W.A.T. Nogueira, S.P. Walborn, S. Pádua, C.H. Monken, Phys. Rev. Lett. 92 (2004) 043602.
- [114] R. Horodecki, P. Horodecki, M. Horodecki, K. Horodecki, Rev. Modern Phys. 81 (2009) 865.
- [115] O. Gühne, G. Tóth, Phys. Rep. 474 (2009) 1.
- [116] L.-M. Duan, G. Giedke, J.I. Cirac, P. Zoller, Phys. Rev. Lett. 84 (2000) 2722.
- [117] S. Mancini, V. Giovannetti, D. Vitali, P. Tombesi, Phys. Rev. Lett. 88 (2002) 120401.
- [118] M.D. Reid, P.D. Drummond, Phys. Rev. Lett. 60 (1988) 2731.
- [119] M.D. Reid, Phys. Rev. A 40 (1989) 913.
- [120] S.L. Braunstein, P. van Loock, Rev. Modern Phys. 77 (2005) 513.
- [121] G. Adesso, F. Illuminati, J. Phys. A: Math. Theor. 40 (2007) 7821.
- [122] P. Hyllus, J. Eisert, New J. Phys. 8 (2006) 51.
- [123] V. Giovannetti, S. Mancini, D. Vitali, P. Tombesi, Phys. Rev. A 67 (2003) 022320.
- [124] R. Simon, Phys. Rev. Lett. 84 (2000) 2726.
- [125] S. Braunstein, A. Mann, Phys. Rev. A 51 (1995) R1727.
- [126] A. Peres, Phys. Rev. Lett. 77 (1996) 1413.
- [127] M. Horodecki, P. Horodecki, R. Horodecki, Phys. Lett. A 223 (1996) 1.
- [128] H. Nha, M.S. Zubairy, Phys. Rev. Lett. 101 (2008) 130402.
- [129] E. Shchukin, W. Vogel, Phys. Rev. Lett. 95 (2005) 230502.
- [130] R.M. Gomes, A. Salles, F. Toscano, P.H.S. Ribeiro, S.P. Walborn, Proc. Natl. Acad. Sci. 106 (2009) 21517.
- [131] G.S. Agarwal, A. Biswas, New J. Phys. 7 (2005) 211.
- [132] M. Hillery, M.S. Zubairy, Phys. Rev. Lett. 96 (2006) 050503.
- [133] M. Hillery, M.S. Zubairy, Phys. Rev. A 74 (2006) 032333.
- [134] X.-y. Chen, Phys. Rev. A 76 (2007) 022309.
- [135] C. Rodó, G. Adesso, A. Sanpera, Phys. Rev. Lett. 100 (2008) 110505.
- [136] S.P. Walborn, B.G. Taketani, A. Salles, F. Toscano, R.L. de Matos Filho, Phys. Rev. Lett. 103 (2009) 160505.
- [137] A. Miranowicz, M. Piani, P. Horodecki, R. Horodecki, Phys. Rev. A 80 (2009) 052303.
- [138] M. Hillery, H.T. Dung, J. Niset, Phys. Rev. A 80 (2009) 052335.
- [139] J. Sperling, W. Vogel, Phys. Rev. A 79 (2009) 022318.
- [140] J. Sperling, W. Vogel, Phys. Rev. A 79 (2009) 052313.
- [141] G. Adesso, Phys. Rev. A 79 (2009) 022315.
- [142] H. Di Lorenzo Pires, M.P. van Exter, Phys. Rev. A 79 (2009) 041801.
- [143] H. Di Lorenzo Pires, M.P. van Exter, Phys. Rev. A 80 (2009) 053820.
- [144] K.W. Chan, J.P. Torres, J.H. Eberly, Phys. Rev. A 75 (2007) 050101.
- [145] C.K. Law, J.H. Eberly, Phys. Rev. Lett. 92 (2004) 127903.
- [146] S.P. Walborn, C.H. Monken, Phys. Rev. A 76 (2007) 062305.
- [147] M.D. Reid, P.D. Drummond, W.P. Bowen, E.G. Cavalcanti, P.K. Lam, H.A. Bachor, U.L. Andersen, G. Leuchs, Rev. Modern Phys. 81 (2009) 1727.
- [148] Z.Y. Ou, S.F. Pereira, H.J. Kimble, K.C. Peng, Phys. Rev. Lett. 68 (1992) 3663.
- [149] H.M. Wiseman, S.J. Jones, A.C. Doherty, Phys. Rev. Lett. 98 (2007) 140402.
- [150] S.J. Jones, H.M. Wiseman, A.C. Doherty, Phys. Rev. A 76 (2007) 052116.
- [151] E.G. Cavalcanti, S.J. Jones, H.M. Wiseman, M.D. Reid, Phys. Rev. A 80 (2009) 032112.
- [152] S.P. Walborn, R.M.G.A. Salles, F. Toscano, P.H.S. Ribeiro, An Entropic Einstein–Podolsky–Rosen Criterion, 2009, [arXiv:0907.4263](https://arxiv.org/abs/0907.4263).
- [153] D. Mendlovic, H.M. Ozaktas, J. Opt. Soc. Am. A 10 (1993) 1875.
- [154] P. Pellat-Finet, Opt. Lett. 19 (1994) 1388.
- [155] A.W. Lohmann, Opt. Commun. 115 (1995) 437.
- [156] H.M. Ozaktas, Z. Zalevsky, M.A. Kutay, The Fractional Fourier Transform: With Applications in Optics and Signal Processing, John Wiley and Sons Ltd, New York, 2001.
- [157] N. Wiener, J. Math. Phys. MIT 8 (1929) 70.
- [158] V. Namias, J. Inst. Appl. Math. 25 (1980) 241265.
- [159] A.C.M. Bride, F.H. Kerr, IMA J. Appl. Math. 39 (1987) 159.
- [160] S. Chountasis, A. Vourdas, C. Bendjaballah, Phys. Rev. A. 60 (1999) 3467.
- [161] A.W. Lohmann, J. Opt. Soc. Am. A 10 (1993) 2181.
- [162] G.R. Fowles, Introduction to Modern Optics, Dover, New York, 1989.
- [163] D.F. McAlister, M. Beck, L. Clarke, A. Mayer, M.G. Raymer, Opt. Lett. 20 (1181) (1995).
- [164] Y. Kang, K. Cho, J. Noh, D.L.P. Vitullo, C.L.M.G. Raymer, Opt. Exp. 18 (1217) (2010).
- [165] E. Mukamel, K. Banaszek, I.A. Walmsley, C. Dorner, Opt. Lett. 28 (2003) 1317.
- [166] B.J. Smith, B. Killet, M.G. Raymer, I.A. Walmsley, K. Banaszek, Opt. Lett. 30 (2005) 3365.
- [167] D.S. Tasca, S.P. Walborn, P.H.S. Ribeiro, F. Toscano, P. Pellat-Finet, Phys. Rev. A 79 (2009) 033801.
- [168] D.S. Tasca, S.P. Walborn, P.H.S. Ribeiro, F. Toscano, Phys. Rev. A 78 (2008) 010304R.
- [169] L. Allen, M.W. Beijersbergen, R.J.C. Spreeuw, J.P. Woerdman, Phys. Rev. A 45 (1992) 8185.
- [170] M.W. Beijersbergen, L. Allen, H.E.L.O. van der Veen, J.P. Woerdman, Opt. Commun. 96 (1993) 123.
- [171] D.G. Grier, Nature 424 (2003) 810.
- [172] H.H. Arnaut, G.A. Barbosa, Phys. Rev. Lett. 85 (2001) 286.
- [173] A. Vaziri, G. Weihs, A. Zeilinger, Phys. Rev. Lett. 89 (2002) 240401.
- [174] A. Vaziri, J.-W. Pan, T. Jennewein, G. Weihs, A. Zeilinger, Phys. Rev. Lett. 91 (2003) 227902.
- [175] G. Molina-Terriza, A. Vaziri, J. Reháček, Z. Hradil, A. Zeilinger, Phys. Rev. Lett. 92 (2004) 167903.
- [176] G. Molina-Terriza, A. Vaziri, R. Ursin, A. Zeilinger, Phys. Rev. Lett. 94 (2005) 040501.
- [177] G. Molina-Terriza, J.P. Torres, L. Torner, Nat. Phys. 3 (2007) 305.
- [178] X. Xue, H. Wei, A.G. Kirk, Opt. Lett. 26 (2001) 1746.
- [179] J. Leach, M.J. Padgett, S.M. Barnett, S. Franke-Arnold, J. Courtial, Phys. Rev. Lett. 88 (2002) 257901.
- [180] H. Wei, X. Xue, J. Leach, M.J. Padgett, S.M. Barnett, S. Franke-Arnold, E. Yao, J. Courtial, Opt. Commun. 223 (2003) 117.
- [181] J. Arit, K. Dholakia, L. Allen, M.J. Padgett, Phys. Rev. A 59 (1999) 3950.
- [182] K. Dholakia, N.B. Simpson, M.J. Padgett, L. Allen, Phys. Rev. A 54 (1996) R3742.
- [183] J. Courtial, K. Dholakia, L. Allen, M.J. Padgett, Phys. Rev. A 56 (1997) 4193.
- [184] A. Mair, A. Vaziri, G. Weihs, A. Zeilinger, Nature 412 (2001) 313.
- [185] S. Franke-Arnold, S.M. Barnett, M.J. Padgett, L. Allen, Phys. Rev. A 65 (2002) 033823.
- [186] S.P. Walborn, A.N. de Oliveira, R.S. Thebaldi, C.H. Monken, Phys. Rev. A 69 (2004) 023811.
- [187] X.-F. Ren, G.-P. Guo, B. Yu, J. Li, G.-C. Guo, J. Opt. B: Quantum Semiclass. Opt. 6 (2004) 243.
- [188] C.I. Osorio, G. Molina-Terriza, J.P. Torres, Phys. Rev. A 77 (2008) 015810.
- [189] J.P. Torres, C.I. Osorio, L. Torner, Opt. Lett. 29 (2004) 1939.
- [190] C.K. Hong, Z.Y. Ou, L. Mandel, Phys. Rev. Lett. 59 (1987) 2044.
- [191] K. Mattle, H. Weinfurter, P. Kwiat, A. Zeilinger, Phys. Rev. Lett. 76 (1996) 4656.

- [192] D. Bouwmeester, J. Pan, K. Mattle, M. Eibl, H. Weinfurter, A. Zeilinger, *Nature* 390 (1997) 575.
- [193] T.B. Pittman, B.C. Jacobs, J.D. Franson, *Phys. Rev. Lett.* 88 (2002) 257902.
- [194] J.L. O'Brien, G.J. Pryde, A.G. White, T.C. Ralph, D. Branning, *Nature* 426 (2003) 264.
- [195] N.K. Langford, T.J. Weinhold, R. Prevedel, K.J. Resch, A. Gilchrist, J.L. O'Brien, G.J. Pryde, A.G. White, *Phys. Rev. Lett.* 95 (2005) 210504.
- [196] N. Kiesel, C. Schmid, U. Weber, R. Ursin, H. Weinfurter, *Phys. Rev. Lett.* 95 (2005) 210505.
- [197] R. Okamoto, H.F. Hofmann, S. Takeuchi, K. Sasaki, *Phys. Rev. Lett.* 95 (2005) 210506.
- [198] S.P. Walborn, A.N. de Oliveira, S. Pádua, C.H. Monken, *Phys. Rev. Lett.* 90 (2003) 143601.
- [199] S.P. Walborn, W.A.T. Nogueira, A.N. de Oliveira, S. Pádua, C.H. Monken, *Mod. Phys. Lett. B* 19 (2005) 1.
- [200] W.H. Peeters, E.J.K. Verstegen, M.P. van Exter, *Phys. Rev. A* 76 (2007) 042302.
- [201] S.P. Walborn, A.N. de Oliveira, S. Pádua, C.H. Monken, *Europhys. Lett.* 62 (2003) 161.
- [202] M. Nielsen, I. Chuang, *Quantum Computation and Quantum Information*, Cambridge, Cambridge, 2000.
- [203] M. Wolf, G. Giedke, J.I. Cirac, *Phys. Rev. Lett.* 96 (2006) 080502.
- [204] M.P. van Exter, A. Aiello, S.S.R. Oemrawsingh, G. Nienhuis, J.P. Woerdman, *Phys. Rev. A* 74 (2006) 012309.
- [205] H.D.L. Pires, C.H. Monken, M.P. van Exter, *Phys. Rev. A* 80 (2009) 022307.
- [206] H. Di Lorenzo Pires, H.C.B. Florijn, M.P. van Exter, *Phys. Rev. Lett.* 104 (2010) 020505.
- [207] S.P. Walborn, P.H.S. Ribeiro, L. Davidovich, F. Mintert, A. Buchleitner, *Nature* 440 (2006) 1022.
- [208] S.P. Walborn, P.H.S. Ribeiro, L. Davidovich, F. Mintert, A. Buchleitner, *Phys. Rev. A* 75 (2007) 032338.
- [209] S.S.R. Oemrawsingh, D.V.X. Ma, A. Aiello, E.R. Eliel, G.W. 't Hooft, J.P. Woerdman, *Phys. Rev. Lett.* 95 (2005) 240501.
- [210] J.B. Pors, A. Aiello, S.S.R. Oemrawsingh, M.P. van Exter, E.R. Eliel, J.P. Woerdman, *Phys. Rev. A* 77 (2008) 033845.
- [211] J.B. Pors, S.S.R. Oemrawsingh, A. Aiello, M.P. van Exter, E.R. Eliel, G.W. 't Hooft, J.P. Woerdman, *Phys. Rev. Lett.* 101 (2008) 120502.
- [212] S.S.R. Oemrawsingh, J.A. de Jong, X. Ma, A. Aiello, E.R. Eliel, G.W. 't Hooft, J.P. Woerdman, *Phys. Rev. A* 73 (2006) 032339.
- [213] C.E. Shannon, W. Weaver, *The Mathematical Theory of Communication*, University of Illinois Press, 1949.
- [214] L. Neves, G. Lima, E.J.S. Fonseca, L. Davidovich, S. Pádua, C. Saavedra, *Phys. Rev. A* 76 (2007) 032314.
- [215] W.K. Wootters, *Phys. Rev. Lett.* 80 (1998) 2245.
- [216] A.K. Ekert, P.L. Knight, *Am. J. Phys.* 63 (1994) 415.
- [217] S.P. Walborn, S. Pádua, C.H. Monken, *Phys. Rev. A* 71 (2005) 053812.
- [218] A.F. Abouraddy, T. Yarnall, B.E.A. Saleh, M.C. Teich, *Phys. Rev. A* 75 (2007) 052114.
- [219] T. Yarnall, A.F. Abouraddy, B.E.A. Saleh, M.C. Teich, *Phys. Rev. Lett.* 99 (2007) 170408.
- [220] J. Bell, *Physics* 1 (1965) 195.
- [221] D. Bohm, *Quantum Theory*, Prentice Hall, Englewood Cliffs, NJ, 1951.
- [222] J. Clauser, M. Horne, A. Shimony, R. Holt, *Phys. Rev. Lett.* 23 (1969) 880.
- [223] J.S. Bell, *Speakable and Unsayable in Quantum Mechanics*, Cambridge University Press, Cambridge, 1987.
- [224] S. Freedman, J. Clauser, *Phys. Rev. Lett.* 28 (1972) 938.
- [225] A. Aspect, P. Grangier, G. Roger, *Phys. Rev. Lett.* 49 (1982) 91.
- [226] A. Aspect, J. Dalibard, G. Roger, *Phys. Rev. Lett.* 49 (1982) 1804.
- [227] G. Weihs, T. Jennewein, C. Simon, H. Weinfurter, A. Zeilinger, *Phys. Rev. Lett.* 81 (1998) 5039.
- [228] W. Tittel, J. Brendel, T. Herzog, H. Zbinden, N. Gisin, *Phys. Rev. A* 57 (1998) 3229.
- [229] S. Gröblacher, T. Paterek, R. Kaltenbaek, C. Brukner, M. Zukowski, M. Aspelmeyer, A. Zeilinger, *Nature* 449 (2007) 871.
- [230] D. Salart, A. Baas, C. Branciard, N. Gisin, H. Zbinden, *Nature* 454 (2008) 861.
- [231] K. Banaszek, K. Wodkiewicz, *Phys. Rev. A* 58 (1998) 4345.
- [232] K. Banaszek, K. Wodkiewicz, *Phys. Rev. Lett.* 82 (1999) 2009.
- [233] M. Revzen, P.A. Mello, A. Mann, L.M. Johansen, *Phys. Rev. A* 71 (2005) 022103.
- [234] Z.-B. Chen, J.-W. Pan, G. Hou, Y.-D. Zhang, *Phys. Rev. Lett.* 88 (2002) 040406.
- [235] T. Yarnall, A.F. Abouraddy, B.E.A. Saleh, M.C. Teich, *Phys. Rev. Lett.* 99 (2007) 250502.
- [236] H. Sasada, M. Okamoto, *Phys. Rev. A* 68 (2003) 012323.
- [237] H. Bechmann-Pasquinucci, W. Tittel, *Phys. Rev. A* 61 (2000) 062308.
- [238] M. Bourennane, A. Karlsson, G. Bjork, *Phys. Rev. A* 64 (2001) 012306.
- [239] N.J. Cerf, M. Bourennane, A. Karlsson, N. Gisin, *Phys. Rev. Lett.* 88 (2002) 127902.
- [240] R.W. Spekkens, T. Rudolph, *Phys. Rev. A* 65 (2001) 012310.
- [241] A. Ambainis, *Proceedings of 33rd Annual Symposium on Theory of Computing*, ACM, New York, 2001, p. 134.
- [242] R.W. Spekkens, T. Rudolph, *Phys. Rev. Lett.* 89 (2002) 227901.
- [243] D. Collins, N. Gisin, N. Linden, S. Massar, S. Popescu, *Phys. Rev. Lett.* 88 (2002) 040404.
- [244] J.P. Torres, A. Alexandrescu, L. Torner, *Phys. Rev. A* 68 (2003) 050301.
- [245] J.P. Torres, Y. Deyanova, L. Torner, G. Molina-Terriza, *Phys. Rev. A* 67 (2003) 052313.
- [246] D.S. Tasca, S.P. Walborn, F. Toscano, P.H.S. Ribeiro, *Phys. Rev. A* 80 (2009) 030101.
- [247] N.R. Heckenberg, R. McDuff, C.P. Smith, A.G. White, *Opt. Lett.* 17 (1992) 221.
- [248] E. Yao, S. Franke-Arnold, J. Courtial, M.J. Padgett, S.M. Barnett, *Opt. Express* 14 (2006) 13089. URL: <http://www.opticsexpress.org/abstract.cfm?URI=oe-14-26-13089>.
- [249] M. Stütz, S. Gröblacher, T. Jennewein, A. Zeilinger, *Appl. Phys. Lett.* (2007) 261114.
- [250] J. Leach, B. Jack, J. Romero, M. Ritsch-Marte, R.W. Boyd, A.K. Jha, S.M. Barnett, S. Franke-Arnold, M.J. Padgett, *Opt. Express* 17 (2009) 8287.
- [251] G. Lima, A. Vargas, L. Neves, R. Guzmán, C. Saavedra, *Opt. Express* 17 (2009) 107450.
- [252] N.K. Langford, R.B. Dalton, M.D. Harvey, J.L. O'Brien, G.J. Pryde, A. Gilchrist, S.D. Bartlett, A.G. White, *Phys. Rev. Lett.* 93 (2004) 053601.
- [253] G. Gibson, J. Courtial, M. Padgett, M. Vasanetsov, V. Pas'ko, S. Barnett, S. Franke-Arnold, *Opt. Express* 12 (2004) 5448. URL: <http://www.opticsexpress.org/abstract.cfm?URI=oe-12-22-5448>.
- [254] S. Gröblacher, T. Jennewein, A. Vaziri, G. Weihs, A. Zeilinger, *N. J. Phys.* 8 (2006) 75.
- [255] L. Neves, S. Pádua, C. Saavedra, *Phys. Rev. A* 69 (2004) 042305.
- [256] M.N. O'Sullivan-Hale, I.A. Khan, R.W. Boyd, J.C. Howell, *Phys. Rev. Lett.* 94 (2005) 220501.
- [257] S.P. Walborn, D.S. Lemelle, M.P. Almeida, P.H.S. Ribeiro, *Phys. Rev. Lett.* 96 (2006) 090501.
- [258] P.G. Kwiat, *J. Mod. Optics* 44 (1997) 2173.
- [259] S.P. Walborn, M.P. Almeida, P.H.S. Ribeiro, C.H. Monken, *Quant. Inform. Comput.* 6 (2006) 336.
- [260] J.T. Barreiro, N.K. Langford, N.A. Peters, P.G. Kwiat, *Phys. Rev. Lett.* 95 (2005) 260501.
- [261] P.G. Kwiat, H. Weinfurter, *Phys. Rev. A* 58 (1998) R2623.
- [262] S.P. Walborn, S. Pádua, C.H. Monken, *Phys. Rev. A* 68 (2003) 042313.
- [263] T.-C. Wei, J.T. Barreiro, P.G. Kwiat, *Phys. Rev. A* 75 (2007) 060305.
- [264] C. Schuck, G. Huber, C. Kurtsiefer, H. Weinfurter, *Phys. Rev. Lett.* 96 (2006) 190501.
- [265] J.T. Barreiro, T. Wei, P.G. Kwiat, *Nat. Phys.* 4 (2008) 282.
- [266] L. Aolita, S.P. Walborn, *Phys. Rev. Lett.* 98 (2007) 100501.
- [267] C.E.R. Souza, C.V.S. Borges, A.Z. Khoury, J.A.O. Huguinin, L. Aolita, S.P. Walborn, *Phys. Rev. A* 77 (2008) 032345.
- [268] A.N. de Oliveira, S.P. Walborn, C.H. Monken, *J. Optics B: Quant. Semiclass. Optics* 7 (2005) 288.
- [269] S.P. Walborn, D.S. Lemelle, D.S. Tasca, P.H.S. Ribeiro, *Phys. Rev. A* 77 (2008) 062323.
- [270] W. Tittel, J. Brendel, B. Gisin, T. Herzog, H. Zbinden, N. Gisin, *Phys. Rev. A* (1998) 3229.

- [271] R. Ursin, F. Tiefenbacher, T. Schmitt-Manderbach, H. Weier, T. Scheidl, M. Lindenthal, B. Blauensteiner, T. Jennewein, J. Perdigues, P. Trojek, et al., *Nat. Phys.* 3 (2007) 481.
- [272] G. Lima, L. Neves, I.F. Santos, J.G.A. Gomez, C. Saavedra, S. Pádua, *Phys. Rev. A* (2006) 032340.
- [273] G. Lima, F.A. Torres-Ruiz, L. Neves, A. Delgado, C. Saavedra, S. Pádua, *J. Phys.: Conf. Ser.* (2007) 012012.
- [274] G. Lima, F.A. Torres-Ruiz, L. Neves, A. Delgado, C. Saavedra, S. Pádua, *J. Phys. B* (2008) 185501.
- [275] G. Lima, F.A. Torres-Ruiz, A.D.L. Neves, C. Saavedra, S. Pádua, *Opt. Commun.* (2008) 5058.
- [276] G. Taguchi, T. Dougakiuchi, N. Yoshimoto, K. Kasai, M. Iinuma, H.F. Hofmann, Y. Kadoya, *Phys. Rev. A* (2008) 012307.
- [277] G. Taguchi, T. Dougakiuchi, M. Iinuma, H.F. Hofmann, Y. Kadoya, *Phys. Rev. A* (2009) 062102.
- [278] C.H. Bennett, G. Brassard, *Proceedings of the International Conference on Computer Systems and Signal Processing, Bangalore, India, IEEE, New York*, 1984, p. 175.
- [279] C.H. Bennett, G. Brassard, N.D. Mermin, *Phys. Rev. Lett.* 68 (1992) 557.
- [280] F. Spedalieri, 2004, [arXiv:quant-ph/0409057](https://arxiv.org/abs/quant-ph/0409057).
- [281] M.P. Almeida, S.P. Walborn, P.H.S. Ribeiro, *Phys. Rev. A* 72 (2005) 022313.
- [282] F. Grosshans, N.J. Cerf, *Phys. Rev. Lett.* 92 (2004) 047905.
- [283] L. Zhang, C. Silberhorn, I.A. Walmsley, *Phys. Rev. Lett.* 100 (2008) 110504.
- [284] Cover, Thomas, *Elements of Information Theory*, John Wiley and Sons, 2006.
- [285] I. Bialynicki-Birula, J. Mycielski, *Comm. Math. Phys.* 44 (1975) 129.
- [286] C. Paterson, *Phys. Rev. Lett.* 94 (2005) 153901.
- [287] B.J. Smith, M.G. Raymer, *Phys. Rev. A* 74 (2006) 062104.
- [288] D.L. Fried, *J. Opt. Soc. Am.* 56 (1966) 1372.
- [289] M.W. Wright, M. Srinivasan, K. Wilson, *IPN Progress Report* 42 (2005) 1.
- [290] R.K. Tyson, *J. Opt. Soc. Am. A* 19 (2002) 753.
- [291] R.K. Tyson, D.E. Canning, *App. Opt.* 42 (2003) 4239.
- [292] J.B. Pors, C.H. Monken, E.R. Eliel, J.P. Woerdman, 2009, [arXiv:0909.3750v1](https://arxiv.org/abs/0909.3750v1).
- [293] C.H. Bennett, G. Brassard, C. Crépeau, R. Jozsa, A. Peres, W.K. Wothers, *Phys. Rev. Lett.* 70 (1993) 1895.
- [294] L. Vaidman, *Phys. Rev. A* 49 (1994) 1473.
- [295] S. Braunstein, H.J. Kimble, *Phys. Rev. Lett.* 80 (1998) 869.
- [296] A. Furusawa, J.L. Sorensen, S.L. Braunstein, C.A. Fuchs, H.J. Kimble, E.S. Polzik, *Science* 282 (1998) 706.
- [297] H.J. Briegel, W. Dür, J.I. Cirac, P. Zoller, *Phys. Rev. Lett.* 81 (1998) 5932.
- [298] J.F. Sherson, H. Krauter, R.K. Olsson, B. Julsgaard, K. Hammerer, I. Cirac, E.S. Polzik, *Nature* 443 (2006) 557.
- [299] D. Gottesman, I.L. Chuang, *Nature* 402 (1999) 390.
- [300] I.V. Sokolov, M.I. Kolobov, A. Gatti, L.A. Lugiato, *Opt. Commun.* 193 (2001) 175.
- [301] L.V. Magdenko, I.V. Sokolov, M.I. Kolobov, [quant-ph/0602200](https://arxiv.org/abs/quant-ph/0602200).
- [302] S.P. Walborn, D.S. Ether, R.L. de Matos Filho, N. Zagury, *Phys. Rev. A* 76 (2007) 033801.
- [303] D.S. Ether, C.H. Monken, P.H.S. Ribeiro, R.L. de Matos Filho, *Phys. Rev. A* 73 (2006) 053819.
- [304] S. Tanzilli, W. Tittel, M. Halder, O. Alibart, P. Baldi, N. Gisin, H. Zbinden, *Nature* 437 (2005) 116.
- [305] Y.-H. Kim, S.P. Kulik, Y.H. Shih, *Phys. Rev. Lett.* 86 (2001) 1370.